Proteome-scale Investigation of Protein Modification and Metabolic Regulation in Brown Adipose Tissue

Samuel W. Entwisle

A dissertation

submitted in partial fulfillment of the

requirements for the degree of

Doctor of Philosophy

University of Washington

2019

Reading Committee:

Judit Villén, Chair

James E. Bruce

Peter S. Rabinovitch

Program Authorized to Offer Degree:

Molecular and Cellular Biology

University of Washington

Abstract

Proteome-scale Investigation of Protein Modification and Metabolic Regulation in Brown Adipose Tissue

Samuel W. Entwisle

Chair of the Supervisory Committee:

Judit Villén, Associate Professor

Genome Sciences

Brown adipose tissue (BAT) is present in most mammals, and becomes highly metabolically active during cold exposure. Its ability to lower blood glucose and burn calories when it is activated holds great interest for its potential as a therapeutic target for metabolic diseases such as type-2 diabetes. However, in order to leverage this unique functionality of BAT to develop novel therapeutics, it will be important to gain a better systems-wide understand of the cellular consequences of its activation, and the signaling and regulatory networks that control its metabolism. In this dissertation, these questions are explored using mass spectrometry (MS)-based proteomics, through two research projects: a study of protein acetylation and metabolomics in mouse BAT, and a study of signaling dynamics dependent on the mTOR complex 2 subunit RICTOR. To investigate the system-wide molecular effects of different degrees of chronic thermogenesis, we measured protein expression and the levels of protein acetylation using MS, and integrated our analysis with polar metabolite data that had been collected from the same mouse cohort. This analysis uncovered broad increases in mitochondrial protein acetylation after severe cold acclimation, increases to acetylated amino

acids and acetylcarnitine, and novel cold-dependent acetylation sites on the uncoupling protein UCP1 that may play a role in regulating protein stability. To investigate the downstream effectors of RICTOR in brown adipocytes, we compared the time course response to insulin of control brown adipocytes and those possessing an inducible knockout of *Rictor* (*Rictor*-iKO). We employed MS to measure the global proteome and phosphoproteome, as well as a set of phosphorylation sites in a targeted analysis. This revealed broad differences in the proteome between control and knockout cells including an increased immune response in *Rictor*-iKO cells, as well as a mild repression of insulin-sensitive sites including the lipogenesis-associated enzyme ATP citrate lyase. These results suggest that RICTOR plays a multifaceted role in cells that extends beyond insulin signaling. In sum, we have investigated the proteome responses to cold acclimation and to the disruption of important signal transduction machinery. The findings have expanded our view of the metabolic flexibility of BAT, and laid the groundwork for future therapeutic strategies to improve BAT function in different contexts.

TABLE OF CONTENTS

LIST OF FIGURES ..... **ii**

ACKNOWLEDGMENTS ..... **iii**

Chapter 1: Systems of Metabolic Regulation in Brown Adipose Tissue **1**

1.1 Brown adipose tissue as a potential therapeutic target *1*

1.2 Neuronal and hormonal regulators of BAT *1*

1.3 BAT metabolic regulation by mTORC2 ..... *3*

1.4 Metabolic changes in BAT during thermogenesis are centered on acetyl-CoA *4*

1.5 Analysis of post-translational modification in BAT *8*

1.6 Goals for this dissertation *12*

Chapter 2: Cold-Induced Thermogenesis Increases Acetylation on the Brown Fat Proteome **13**

2.1 Summary *14*

2.2 Introduction *14*

2.3 Results *16*

2.4 Discussion *35*

2.5 Materials and Methods *38*

Chapter 3: RICTOR Loss Induces an Interferon-Like Response and Unevenly Suppresses Insulin-Dependent Phosphorylation in Brown Adipocytes **45**

3.1 Summary *46*

3.2 Introduction *47*

3.3 Results *49*

3.4 Discussion *62*

3.5 Materials and Methods *66*

Chapter 4: Discussion and Future Directions **73**

4.1 How does the mechanism of activation affect the function of RICTOR/mTORC2? *73*

4.2 How do differentially phosphorylated forms of AKT function? *74*

APPENDIX: SUPPLEMENTAL MATERIAL FOR CHAPTER 2 ..... **76**

REFERENCES **84**

LIST OF FIGURES

Figure 2.1……..18
Figure 2.2……..20
Figure 2.3……..22
Figure 2.4……..24
Figure 2.5……..30
Figure 2.6……..32
Figure 2.7……..34
Figure 3.1……..51
Figure 3.2……..54
Figure 3.3……..57
Figure 3.4……..61

ACKNOWLEDGMENTS

I am privileged to have been given opportunities, mentorship, love, and support by so many people over the years. None of this work would have been possible without these people, and I am immensely grateful.

My parents encouraged me to leave home and attend the Maine School of Sciences and Mathematics in cold and remote Limestone, ME, for my last three years of high school. While there, I was inspired and challenged by my peers, and by standout teachers including David Dougan, Larry Berz, and Alice Bolstridge. At the University of Maine, my interest in chemistry blossomed into a love of biology. I owe that, in large part, to my biochemistry professor and thesis advisor, Dorothy Croall. Apart from training me in molecular biology and biochemistry methods, she showed me how to think about scientific questions rigorously while instilling a passion for research that I will always trace back to her. During this time I also had great experiences collaborating with the lab of Clarissa Henry, where I was trainined in zebrafish research techniques. During a summer internship at the Mount Desert Island Biological Laboratory, Antonio Planchart helped me gain independence and additional bench skills in his laboratory. My two years after working with Laurence Daheron at the iPS Core Facility at Harvard Stem Cell Institute after college were very influential. Laurence fostered a fun and productive lab environment where I learned many cell culture methods while gaining invaluable exposure to the world-class research at Harvard.

At the University of Washington, and in Seattle, I have enjoyed great support from colleagues and friends. During my first three years, I received generous financial support from Susan Potts and Tina Neiders via the ARCS Foundation Seattle Chapter. The administrative staff and directors of the Molecular and Cellular Biology Program, and those of the Genome Sciences

Department, consistently provided helpful guidance and moral support. My thesis committee members Jim Bruce, Maitreya Dunham, Stan Fields, Rich Gardner, and Peter Rabinovitch challenged me and offered great advice and support over the course of my degree program. Experiences at the Pacific Science Center, ComSciCon-PNW, and ENGAGE were invaluable as I sought to become a better communicator of science. Many friends and colleagues within and outside the University have been great sources of inspiration and camaraderie. There are too many people to name, but the potlucks, hiking trips, bike rides, concerts, and book club discussions have made these past few years fun and enriching. In particular, Tim Durham, my roommate for 5 years, has been a great friend and companion with whom to share the journey of graduate school.

The research presented herein is all the result of a collaboration with the lab of David Guertin at the University of Massachusetts Medical Center. Dave's enthusiasm for our work can be felt from across the country, and his ideas have been instrumental. Members of the Guertin lab – particularly the postdocs Joan Sánchez-Gurmaches, Su Myung Jung, and Camila Martinez-Calejman – performed all of the mouse and cell culture experiments presented in this thesis, and have been great to work with. I have had great experiences working with several other collaborators during graduate school, including with the labs of Maitreya Dunham, Margaret Goodell, and Thurl Harris.

The Villén lab has been an excellent place to get my Ph.D. training. I worked with many smart, inspiring, and helpful people during my time here. In particular, Danielle Swaney introduced me to basic proteomics methods during my lab rotation, while Rob Lawrence, Billy Edelman, and Miguel Martín-Pérez were excellent role models during my first few years and beyond. Daniél Hernandez and Ariadna Llovet built our data analysis pipeline and were always helpful and patient with my questions. Ricard Rodríguez was a great mentor and was always generous with

his ideas and troubleshooting prowess. Ian Smith, Kyle Hess, Anthony Valente, Bianca Ruiz, and Mario Leutert have brought great scientific insights, enthusiasm, and vibrancy to the lab over my final couple of years. My advisor, Judit Villén, was a great and supportive mentor. She created a space where I could make mistakes and grow from them in ways I could not have anticipated. I admire her scientific instincts, and the way she has built a collegial lab environment that promotes collaboration and intellectual freedom.

Finally, I would like to thank my family. My parents have given me so much since the begininning, and their unconditional love and support has meant the world. I thank my brothers Noah and Will for their love and camaraderie over all these years. And finally, thanks to Joana, the brightest part of my every day. I love you and I am so excited for our future together.

Chapter 1: Systems of Metabolic Regulation in Brown Adipose Tissue

1.1 Brown adipose tissue as a potential therapeutic target

Type-2 diabetes (T2D) comprises 90% of diabetes cases worldwide, and being overweight is a common risk factor for T2D that affects over one-third of people in the US. Drugs that alleviate the symptoms of both T2D and obesity are desperately needed, as lifestyle changes like diet and exercise are often insufficient due to genetic, geographic, or socioeconomic factors. Brown adipose tissue (BAT) has generated recent interest as a therapeutic target for T2D and obesity. BAT is physiologically activated by exposure to cold temperatures. When active, BAT increases its uptake of glucose and other macronutrients from circulation and burns calories to generate heat in a process called non-shivering thermogenesis. In mice as well as humans, cold exposure or transplantation of BAT (in mice only) improved symptoms of T2D (Bartelt et al. 2011) (Stanford et al. 2013), (Chondronikola et al. 2014). These results suggest that increasing BAT activity by mimicking cold exposure is a promising therapeutic strategy for T2D in humans, yet our understanding of metabolic regulation in BAT will need to improve in order to develop viable drug targets.

1.2 Neuronal and hormonal regulators of BAT

The sympathetic nervous system (SNS) is the primary stimulus that initiates BAT thermogenesis. Environmental cold exposure activates the SNS, which, among many responses organism-wide, leads to norepinephrine stimulation of the β3-adrenergic receptor in brown adipocytes, and a subsequent cAMP signaling cascade. In addition to norepinephrine, adenosine is also released at synapses in brown fat, which augments cAMP generation (Gnad et al. 2014). SNS-induced cAMP generation in BAT causes increased glucose uptake, which

likely occurs in two stages (Dallner et al. 2006). The early stage involves cAMP-driven translocation of the GLUT1 transporter to the plasma membrane (Olsen et al. 2014), (Mukaida et al. 2017), and the second involves cAMP-dependent *de novo* synthesis of GLUT1 (Dallner et al. 2006). cAMP also activates protein kinase A (PKA) which, among other things, phosphorylates substrates that promote lipolysis of stored triglycerides. PKA also phosphorylates the transcription factor CREB, which binds to the cAMP response element and induces transcription of many target genes important for thermogenesis, including the uncoupling protein UCP1. UCP1 helps to mediate thermogenesis in the mitochondria by localizing to the inner mitochondrial membrane and uncoupling the proton motive force from ATP synthesis, thus dissipating it as heat.

Much upstream regulation of BAT activity occurs at the level of the central nervous system, however brown adipocyte metabolism is sensitive to many other extracellular stimuli that originate from different parts of the body. For example, thyroid hormone has been shown to promote BAT activity by causing transcriptional changes that favor increased energy expenditure (de Jesus et al. 2001). The adrenocorticotropic hormone, ACTH, has been shown to enhance thermogenesis in BAT (van den Beukel et al. 2014), while endocannabinoids (Boon et al. 2014) and glucocorticoids (Strack et al. 1995) have been shown to directly inhibit BAT thermogenesis.

BAT is also highly sensitive to insulin, which apart from driving glucose uptake after feeding, is important for the development of functional BAT. One study showed that BAT-specific loss of the insulin receptor leads to an age-dependent atrophy of BAT, and a defect in insulin secretion that led to a diabetic phenotype (Guerra et al. 2001). While the reason for the insulin-dependence of BAT wasn't fully elucidated, the authors did observe a slight drop in the expression of BAT-specific transcription factors, and a loss of *de novo* lipogenesis (DNL) gene

expression, the latter of which is a consistent feature of thermogenesis (Yu et al. 2002; Sanchez-Gurmaches et al. 2018). The kinase AKT is activated downstream of insulin stimulation and is important for regulating metabolism, as well as pro-growth and pro-survival cellular responses. In mice, AKT2 expression has been shown to be induced in cold-activated BAT, and is important for cold-induced increases in DNL as well as BAT tissue size, and its loss causes increases in apparent compensatory "browning" of white adipose tissue, indicating decreased BAT function (Sanchez-Gurmaches et al. 2018). Cold exposure has been shown to increase the maximal insulin response in BAT and other insulin-sensitive tissues in rats (Vallerand et al. 1987). Taken together, these results suggest that insulin signaling is an important part of BAT function that influences glucose uptake and DNL, and that a better understanding of the determinants of healthy insulin signaling in BAT could point towards molecular targets for therapeutically increasing BAT activity.

1.3 BAT metabolic regulation by mTORC2

Downstream of insulin, mechanistic target of rapamycin (mTOR) is an important regulator of cellular metabolism. It exists in two functional distinct protein complexes: mTOR complex 1 (mTORC1) and mTOR complex 2 (mTORC2). mTORC1 is activated by intracellular amino acid levels, and by the kinase AKT in response to stimulation by insulin and other growth factors. When active, it promotes cell growth by stimulating protein synthesis and ribosome biogenesis (Saxton & Sabatini 2017). The mechanism of activation and downstream effectors of mTOR complex 2 (mTORC2) are less well understood. Because there is no specific inhibitor for mTORC2, to generate mTORC2 loss-of-function, a common strategy is to knock out the mTORC2-specific subunit RICTOR. Studies of RICTOR-deficient cells have revealed that mTORC2 phosphorylates AKT in its C-terminal hydrophobic motif (Sarbassov 2005). Analysis of phospho-mimetic and -inhibitory AKT mutants by *in vitro* enzyme assays showed that this

phosphorylation site is likely necessary for maximal activity (Alessi et al. 1996). Whole body ablation of RICTOR in mice was embryonic lethal (Guertin et al. 2006), while tissue-specific knockouts in mice have shown that RICTOR promotes insulin-stimulated glucose uptake in skeletal muscle (Kumar et al. 2008), and lipogenesis in liver (Yuan et al. 2012). Genetic knockout of RICTOR in BAT has shown that mTORC2 is important for regulating glucose and lipid metabolism, although the phenotype depends on the specific knockout model used. In one study, RICTOR was knocked out in the *aP2+* lineage, which is specific to both white and brown adipocytes (Albert et al. 2016). Here, the authors found that mTORC2 loss in BAT causes deficiencies in glucose uptake and thermogenesis. In contrast, *Rictor-iKO* in the *Myf5+* lineage (*Myf5-Rictor*^{iKO}), which includes BAT and skeletal muscle, shrank BAT size and reduced DNL, but actually improved thermogenesis while protecting mice from diet-induced obesity (Hung et al. 2014). The discrepancy between these studies could be due to the different tissue-specificities of *Rictor-iKO*, and the tissue "specificity" of *aP2*-promoter-driven knockouts has been called into question (K. Y. Lee et al. 2013). *In vitro* cell culture models have additionally shown that brown adipocyte differentiation (Hung et al. 2014) and glucose uptake (Olsen et al. 2014) are both dependent on RICTOR. Despite the strong phenotypes, and regardless of the differences between specific knockout models, it has been difficult to conclusively demonstrate mTORC2-dependent AKT activity or any other downstream effectors of mTORC2. Understanding the role of mTORC2 in the context of BAT insulin/AKT signaling will be an important area of research moving forward.

1.4 Metabolic changes in BAT during thermogenesis are centered on acetyl-CoA

1.4.1 Glucose uptake and metabolism. Cold-induced thermogenesis in BAT entails broad changes to cellular metabolism. These changes include, according to current knowledge, increased glucose and fatty acid uptake from circulation, increased lipolysis of stored

triglycerides, increased β-oxidation of fatty acids, increased DNL, and increased aerobic respiration. One connection to almost all of these metabolic processes is acetyl-CoA. Mitochondrial acetyl-CoA is the byproduct of glucose and fatty acid oxidation, and an important carbon source for the tricarboxylic acid (TCA) cycle which fuels respiration; cytosolic acetyl-CoA is the two-carbon building block of new lipids in DNL. Despite exhaustive study of individual components or pathways, the way that acetyl-CoA-adjacent pathways are regulated in concert during BAT thermogenesis is poorly understood. The ensuing paragraphs will summarize current knowledge of different metabolic inputs and outputs that converge on acetyl-CoA, and highlight important questions moving forward.

Glucose has many uses in active BAT. For example, a study of the brown adipocyte response to β3-adrenergic stimulation showed that knockdown of glucose transporters GLUT4 or GLUT1, or the glycolytic enzymes hexokinase or pyruvate kinase, decreases the glucose uptake and oxygen consumption rate (Winther et al. 2018). Interestingly, this study also found increased lactate efflux from brown adipocytes after β3-adrenergic stimulation (Winther et al. 2018). Consistent with this, inhibition of glycolysis by 2-deoxyglucose, and knockdown of lactate dehydrogenase, reversed BAT thermogenesis in a mouse model (Jeong et al. 2018). Findings related to lactate generation are consistent with recent work showing that lactate feeds the TCA cycle in most tissues (Hui et al. 2017). Taken together, these results show that glycolysis and lactate fermentation are both required for BAT thermogenesis, presumably through generation of acetyl-CoA.

1.4.2 De novo *lipogenesis.* Glucose can be converted to fatty acids via DNL in active BAT. This occurs when glucose-derived mitochondrial acetyl-CoA is used to generate citrate by the enzyme citrate synthase. Citrate can then subsequently exit mitochondria and enter the cytosol through a citrate-malate antiporter, where it is converted back to acetyl-CoA by the enzyme ATP

citrate lyase (ACLY). From here, acetyl-CoA is converted to malonyl-CoA by acetyl-CoA carboxylase isoforms (ACACA/B) and is subsequently committed to fatty acid synthesis by fatty acid synthase (FASN), and from here can be incorporated into triglycerides and stored in lipid droplets.

Recent work by Irshad et al. in cultured brown adipocytes demonstrated the importance of DNL (Irshad et al. 2017). Using ^{14}C-labeled glucose, the authors find that ^{14}C labeling of $^{14}CO_2$ increases after β3-adrenergic stimulation in a manner dependent on fatty acid oxidation. This implies that, while glucose oxidation increases upon β3-adrenergic stimulation, this increase occurs via DNL and β-oxidation rather than via the TCA cycle. Consistent with this, DNL enzymes are well documented to increase in expression after cold acclimation, due to the upstream transcription factor ChREBPβ (Sanchez-Gurmaches et al. 2018), and blocking DNL to disrupt BAT function (Christoffolete et al. 2004), although it may not be necessary for maintaining body temperature during cold challenge (Guilherme et al. 2018). More work will be needed to fully untangle the role of DNL in BAT thermogenesis. Regardless, DNL appears to be a consistent feature of active BAT metabolism, and creates a demand for a cytosolic pool of acetyl-CoA.

1.4.3 Fatty acid uptake. In addition to lipolysis of triglyceride stores, uptake of fatty acids from circulation fuels β-oxidation in active BAT. Several lines of evidence support the idea that fatty acid uptake is an important feature of active BAT. One study showed that fatty acid uptake increases expression of fatty acid binding proteins correlates with increased tolerance to cold challenge (Wu et al. 2006), while another study showed that cold-activated BAT clears triglyceride-rich lipoproteins from circulation and improves hyperlipidemia (Bartelt et al. 2011). Moving forward, it will be important to establish the determinants and the relative importance of lipolysis and exogenous uptake as sources of fatty acids in BAT.

1.4.4 Importance of fatty acids in BAT. Metabolism of active BAT is geared towards *de novo* synthesis and uptake of fatty acids. Is there an adaptive reason for this? UCP1 is activated by long-chain fatty acids (LCFAs), and it was shown that this is because UCP1 is a H^+/LCFA symporter (Fedorenko et al. 2012). Another critical function of fatty acids in BAT is as fuel for β-oxidation. A few different β-oxidation enzymes have been shown to be necessary for thermogenesis (Ellis et al. 2010), (J. Lee et al. 2015). Complete oxidation of fatty acids leads to high stoichiometric amounts of NADH and acetyl-CoA, which can directly and indirectly supply electrons to the electron transport chain, respectively, to fuel thermogenesis.

1.4.5 Regulation of heat generation in BAT. Aerobic respiration by the electron transport chain (ETC) is the engine that generates heat in BAT. The most well-known method for heat generation by the ETC is via UCP1-mediated uncoupling. However, other mechanisms exist that promote maximal flux through electron transport, including substrate cycling via creatine that continually regenerates ADP, which favors flux through traditional ATP-synthesis-coupled respiration (Kazak et al. 2015). Generation of reactive oxygen species has also been shown to promote increased thermogenesis (Chouchani et al. 2017), at least in part through sulfenylation of cysteine residues on UCP1 itself (Chouchani et al. 2016).

1.4.6 Non-cell autonomous regulation of organismal metabolism by BAT. While BAT clearly has important cell autonomous function in fuel oxidation and heat generation, it can also regulate metabolism as an endocrine organ. Several secreted factors from BAT have been identified. Some BAT-derived autocrine and paracrine factors regulate BAT size and function directly by, for example, increasing innervation and vascularization of the tissue (Villarroya, Cereijo, et al. 2017). BAT-secreted factors can act in an endocrine manner as well, affecting distant tissues such as the brain, white adipose tissue, and the liver (Villarroya, Cereijo, et al. 2017). Additionally, a loss of BAT function can induce white adipose tissue browning via the central

nervous system(Schulz et al. 2013). While it is not the primary focus of this dissertation, the importance of the non-cell-autonomous roles of BAT will need to be determined, and remains an area of active research.

1.5 Analysis of post-translational modification in BAT

1.5.1 Phosphorylation-based cell signaling. New therapeutic strategies for stimulating BAT activity have great potential to help people with metabolic diseases. Developing such therapies will require a systems-level understanding of changes that occur in BAT during thermogenesis. One particularly useful lens through which to view cellular changes is protein post-translational modification (PTM). Reversible phosphorylation is perhaps the most well understood post translational modification in terms of its cellular function. Phosphorylation is a highly conserved mechanism by which cells transmit signals to and from their external environment, and within themselves. Most commonly, this occurs when a kinase catalyzes the phosphorylation of a serine, threonine, or tyrosine side chain. Dephosphorylation is mediated by phosphatases, often as part of negative feedback loops. Signaling pathways mentioned above, such as β3-adrenergic response and the insulin response, rely heavily on reversible protein phosphorylation to transmit important signals. In cells, pathways such as these exist in the context of a dynamic network of molecular interactions that transmits and integrates information from different sources, extracellularly or intracellularly. Defining cell signaling networks should aid in discovering and predicting the effects of novel therapies for countless diseases, including metabolic diseases like type-2 diabetes.

1.5.2 Mass spectrometry-based phosphoproteomics. Quantifying phosphorylation sites across the proteome has proven to be an effective strategy for understanding cell signaling networks. To measure phosphorylation events using the common “bottom-up” approach, proteins from a

sample are proteolytically digested using an enzyme such as trypsin that reproducibly cuts after arginine and lysine residues. This digestion generates short peptides, which can be measured at this stage to ascertain the abundance of their respective proteins irrespective of PTMs. However, to analyze phosphorylation, these peptide samples can be further enriched for phosphorylated peptides using methods such as iron(III) immobilized metal ion chromatography (IMAC), which exploits strong ionic interactions between iron(III) and phosphate. Purified phosphopeptides, or unenriched and mostly unmodified peptides, are then analyzed by liquid chromatography coupled to tandem mass spectrometry (LC-MS/MS). Briefly, LC-MS/MS entails separating complex peptide mixtures using a liquid chromatography method, typically over the course of 1-2 hours. As analytes elute, they are ionized and their m/z is measured in MS scans. From each MS scan, specific analytes are isolated and fragmented in the gas phase. The m/z of those fragments are then measured in a second MS scan known as an MS/MS scan. The pattern of fragments in MS/MS scans allows for identification of the peptide sequence, and in the case of phosphoproteome analysis, localization of the phosphorylated residue.

Several MS/MS acquisition strategies have been employed for bottom-up phosphoproteomics. The most common is data-dependent acquisition (DDA), whereby the top-N (typically 10 or 20) most abundant peptides at any given MS scan are selected for fragmentation, MS/MS analysis, and sequence identification using database searching algorithms such as Comet (Eng et al. 2013). Because only one MS/MS spectrum is needed to confidently detect a peptide, and typically many MS scans can occur during the elution of a single peptide, analytes of the same m/z as a fragmented peptide are typically banned from being fragmented for a short time afterwards. This approach allows peptides that may not have originally made the top-N to be selected for fragmentation themselves. DDA has enabled unsurpassed coverage of the

phosphoproteome in terms of the overall number of phosphorylation sites, making it an excellent tool for discovery.

One weakness of DDA, however, is that it suffers from stochastic sampling and low overlap between samples, making it often difficult to analyze phosphorylation across many samples and experimental conditions. In addition, it can be difficult to test specific hypotheses using DDA, because it can be difficult to ensure that particular phosphorylation sites of interest will be well measured. To achieve more reproducible measurement, and greater agency to test specific hypotheses, parallel reaction monitoring (PRM) can be very useful. PRM differs from DDA in that instead of the most abundant peptides in an MS scan being fragmented, a pre-determined set of phosphopeptides, representing pathways or biological processes of interest, are fragmented regardless of their signal intensity in the MS scan. Apart from allowing lower abundance phosphorylation events to be detected and quantified, PRM is advantageous for phosphoproteomics because it makes it easier to detect and quantify positional isomers of phosphopeptides, i.e. peptides with multiple phospho-acceptor residues that are phosphorylated in different ways. One challenge of PRM approaches, however, is that in order to assemble a set of peptides of interest, the m/z and retention time of peptides must be known. Towards this end, DDA data can be immensely helpful, and previous work has shown that the success of PRM assays can be improved by predicting m/z and retention time using previously-collected DDA data (Lawrence et al. 2016). In sum, DDA and PRM represent highly complementary modes of LC-MS/MS analysis that are well suited to analysis of protein phosphorylation.

1.5.3 Protein acetylation reflects the cellular metabolic state. Another important PTM with potential relevance to BAT is protein acetylation. Acetylation occurs when acetyl-CoA is added to lysine side chains, and it can occur enzymatically by the action of acetyltransferases, or non-enzymatically; deacetylation typically occurs enzymatically. Acetylation is most famously known

as a modification of histone H3 tails that regulates chromatin state and gene expression, however many other nuclear proteins are acetyated and recognized by proteins with specialized acetyl-lysine-recognizing bromodomains (Narita et al. 2019). Interestingly, a recent study found that acetylation stoichiometry in HeLa cells is very low, with a median of 0.02%, but that most high stoichiometry acetylation sites occur via acetyltransferases, and that these sites are on proteins related to transcription regulation, and on acetyltransferases themselves (Hansen et al. 2019). In addition, the environment in mitochondria can be conducive to widespread protein acetylation, as the pH and concentration of reactive acetyl-CoA favor non-enzymatic acetylation (Wagner & Payne 2013). There are some examples of acetylation sites in mitochondria with an impact on protein function (Ozden et al. 2014; Zhao et al. 2010). However, a recent study on mouse heart mitochondrial isolates showed that widespread changes to acetylation likely doesn't affect mitochondrial bioenergetics (Fisher-Wellman et al. 2019).

As with phosphorylation, methods have been developed for global analysis of protein acetylation. Perhaps the most common is an immuno-affinity enrichment for acetylated lysine peptides (Y. Li et al. 2013). Similar to phosphoproteomics approaches, enriched acetylated peptide samples are analyzed by LC-MS/MS, whereby the sequences and site localizations of peptides are identified, and abundances are quantified. Several acetylproteomics studies have been done using different samples, and many found strong changes to global mitochondrial protein acetylation in response to metabolic changes (Hebert et al. 2013) (Schwer et al. 2009), (Chow et al. 2014). Thus, while the degree of its functional impact on the acetylated proteins is unclear, mitochondrial protein acetylation can serve as a readout of cellular metabolic changes.

1.6 Goals for this dissertation

In the ensuing chapters, I will describe studies that aim to characterize the regulatory relationships between metabolism and protein post-translational modifications, namely acetylation and phosphorylation. In chapter 2 of this dissertation, I describe a proteomics, acetylproteomics, and metabolomics study of BAT from mice that were acclimated to mild and severe cold environmental temperatures, compared with mice at thermoneutrality, without cold stress. Using this approach, we contextualized observed changes in protein acetylation, and identified a potentially novel acetylation-based regulatory mechanism on UCP1. In chapter 3, I describe a phosphoproteomics approach to investigate the function of mTORC2 in brown adipocytes. Specifically, I present data from a time series of cultured brown adipocytes, with or without induced knockout of the gene for the mTORC2 subunit RICTOR, that were exposed to insulin over 30 minutes. At each time point, we analyzed the proteome and phosphoproteome using LC-MS/MS. We find that RICTOR loss causes mild, yet broad, suppression of insulin signaling. In chapter 4, I close with ideas for important research directions moving forward.

Chapter 2: Cold-Induced Thermogenesis Increases Acetylation on the Brown Fat Proteome

Samuel W. Entwisle[1,2], Su Myung Jung[3], Joan Sanchez-Gurmaches[3,4,5], Robert T. Lawrence[1,2], David J. Pedersen[3], Miguel Martin-Perez[2], Adilson Guilherme[5], Michael P. Czech[3], David A. Guertin[3,6,7,*], Judit Villen[1,2,*]

[1]Molecular and Cellular Biology Program, University of Washington, Seattle, WA 98195

[2]Department of Genome Sciences, University of Washington, Seattle, WA 98195

[3]Program in Molecular Medicine, University of Massachusetts Medical School, Worcester, MA 01605

[4]Division of Endocrinology, Division of Developmental Biology, Cincinnati Children's Hospital Research Foundation, Cincinnati, OH 45209

[5]Department of Pediatrics, University of Cincinnati College of Medicine, Cincinnati, OH 45209

[6]Department of Molecular, Cell and Cancer Biology, University of Massachusetts Medical School, Worcester, MA 01605

[7]Li Weibo Institute for Rare Diseases Research, University of Massachusetts Medical School, Worcester, MA 01605

*Corresponding authors: David Guertin (David.Guertin@umassmed.edu) and Judit Villen (jvillen@uw.edu)

2.1 Summary

Stimulating brown adipose tissue (BAT) energy expenditure could be a therapy for obesity and related metabolic diseases. Achieving this requires a systems-level understanding of the biochemical underpinnings of thermogenesis. To identify novel metabolic features of active BAT, we measured protein abundance, protein acetylation, and metabolite levels in BAT isolated from mice living in their thermoneutral zone or in colder environments. We find that the enzymes which synthesize lipids from cytosolic acetyl-coA are among the most robustly increased proteins after cold acclimation, consistent with recent studies highlighting the importance of anabolic *de novo* lipogenesis in BAT. In addition, many mitochondrial proteins are hyperacetylated by cold acclimation, including several sites on UCP1, which may have functional relevance. Metabolomics analysis further reveals cold-dependent increases to acetylated carnitine and several amino acids. This BAT multi-omics resource highlights widespread proteomic and metabolic changes linked to acetyl-CoA synthesis and utilization that may be useful in unraveling the remarkable metabolic properties of active BAT.

2.2 Introduction

Brown adipose tissue (BAT) specializes in burning calories to generate heat in a process called thermogenesis. Active BAT can rapidly absorb and metabolize glucose and lipids during thermogenesis(K. L. Townsend & Tseng 2014), and its presence in adult humans correlates with improved metabolic phenotypes(Cypess et al. 2009; Chondronikola et al. 2014). Humans with type-2 diabetes (T2D) or obesity have been shown to have lower rates of BAT glucose uptake (Ouellet et al. 2011), and stimulating BAT activity in mice(Bartelt et al. 2011) and humans(Chondronikola et al. 2014), or transplanting BAT into mice(Stanford et al. 2013), reverses metabolic deficiencies associated with T2D. BAT may also provide metabolic health benefits via secreted factors called BATokines(Villarroya, Gavaldà-Navarro, et al. 2017;

Villarroya et al. 2018; Cereijo et al. 2018). Collectively, these findings suggest that increasing BAT activity may be a promising therapeutic strategy for T2D and obesity in humans. Thus, there is strong rationale for more deeply exploring the biochemical properties of BAT metabolism.

In physiologically relevant settings, BAT is activated by the sympathetic nervous system in response to cold exposure or certain high fat diets(Rothwell & Stock 1997; Feldmann et al. 2009). Cold-induced thermogenesis (CIT) is the best understood mode of BAT activation. Classically, norepinephrine triggers CIT in brown adipocytes by stimulating β3-adrenergic receptor signaling and cAMP synthesis, which activates protein kinase A (PKA). PKA phosphorylates CREB, which binds to the cAMP response element and induces transcription of many target genes including the uncoupling protein UCP1. UCP1 localizes to the inner mitochondrial membrane and dissipates the proton motive force as heat, thus uncoupling it from ATP synthesis. This is thought to be the primary mechanism of heat-generation in BAT, although alternate heat-generating pathways have been reported(Kazak et al. 2017; Ikeda et al. 2017). While many of the signaling modalities that stimulate BAT have been identified, the associated metabolic and proteomic changes that underlie thermogenesis remain less well defined.

To gain a more comprehensive understanding of the molecular underpinnings of CIT, we analyzed the proteome, acetylproteome, and metabolome of BAT from mice that were acclimated to three different temperatures: thermoneutrality (30°C), room temperature (22°C) and severe cold (6°C). We report striking cold-dependent changes that, when integrated, reveal previously unappreciated changes in acetyl-CoA metabolism and redox control relevant to lipid metabolism and thermogenesis, including acetylation sites on UCP1 that may have functional relevance.

2.3 Results

2.3.1 Cold adaptation upregulates lipid synthesis, glucose metabolism, and electron transport chain complex I-II proteins. First, we explored proteomic signatures of chronic cold-induced BAT activation by acclimating mice to three different temperature conditions: thermoneutrality (30°C, which is preferred by mice(Gordon et al. 1998)), room temperature (which is mildly cold for mice, 22°C) and severe cold (6°C) (Fig 2.1A). Following the temperature acclimation period, BAT was harvested and subjected to proteome analysis. The number of confidently detected proteins is consistent across all samples, ranging from 1857 to 2432 (Fig 2.1B). Differential protein expression was determined by comparing each cold condition to thermoneutrality. We identified 60 proteins altered (~3%, 26 increasing, 34 decreasing) in response to mild cold and 232 proteins altered (~11%, 119 increasing, 113 decreasing) in response to severe cold (Fig 2.1C) indicating a thermogenic proteome response that scales with cold severity.

Both mild and severe cold acclimation had profound effects on the proteome. Mild cold acclimation already caused significant increases to *de novo* lipogenesis proteins including ATP citrate lyase (ACLY, 5.2-fold), the two acetyl-CoA carboxylase isoforms (ACACA, 3.5-fold; and ACACB, 3.2-fold), and fatty acid synthase (FASN, 8.5-fold increase) (Figs 2.1D, 2.1F). This is consistent with previous results indicating that *de novo* lipogenesis is a central feature of thermogenesis in BAT (Sanchez-Gurmaches et al. 2018; Mottillo et al. 2014). UCP1 increases 3.7-fold, and the mitochondrial pyruvate carrier 2 (MPC2) increases 3.1-fold after mild cold acclimation (Fig S2.1A). All of the proteins mentioned above also significantly increase after severe cold acclimation. In addition, proteins related to the electron transport chain (ETC) complex I are among the most upregulated after severe cold acclimation (NDUFA12, increasing 3.7-fold; NDUFA10, 2.4-fold; NDUFB6, 3.7-fold; and MTND3, 4.4-fold) (Figs 2.1F, S2.1A). Interestingly, the calcium load-activated channel TMCO1 increases 4.6-fold after severe cold

acclimation, but is not reliably measured in the mild cold condition, possibly because it is below the limit of detection (Figs 2.1E, S2.1A). Notable decreasing proteins include the selenium binding protein 1 (SELENBP1, 2.9-fold decrease after severe cold acclimation), Mimecan (OGN, 4.7-fold), and the centromere protein V (CENPV, 3.5-fold), all of which also significantly decreased, albeit with lower fold-changes, after mild cold acclimation (Fig 2.1D, 2.1E, S2.1B). Interestingly, some proteins decrease after mild cold acclimation, and increase to near thermoneutral levels in the severe cold. These include the long-chain fatty acid CoA ligase (ACSL5, 4.8-fold decrease after mild cold acclimation), and the ubiquitin-like modifier SUMO2 (6.3-fold decrease) (Figs 2.1D, S2.1B). Taken together, analysis of the most significant cold-induced protein changes confirms that lipid synthesis and electron transport are simultaneously upregulated during BAT thermogenesis, while revealing other novel, potential protein markers of BAT activity.

Despite not being among those most significantly regulated, many other notable proteins show interesting responses to cold acclimation. For example, the insulin-regulated glucose transporter, SLC2A4 (a.k.a. GLUT4), is upregulated 2.7-fold in mild cold consistent with insulin and beta-adrenergic signaling cooperating during CIT. Early glycolytic enzymes are also significantly cold-induced, including hexokinase 2 (HK2, 2.6-fold increase in severe cold), glucose-6 phosphate isomerase (GPI, 2.9-fold increase), and the phosphofructokinase liver isoform (PFKL, 2.7-fold increase). This is consistent with increased glucose flux into active BAT and is the basis for detecting BAT by FDG-PET-CT imaging(Cypess et al. 2009). Enzymes in the pentose phosphate pathway are also significantly induced, including glucose-6-phosphate 1-dehydrogenase X (G6PDX, 2.7-fold increase in severe cold), ribose-5-phosphate isomerase (RPIA, 2.6-fold increase, $q = 0.14$), and transaldolase (TALDO1, 1.8-fold increase), suggesting important destinations for glucose besides pyruvate synthesis (Fig S2.1A).

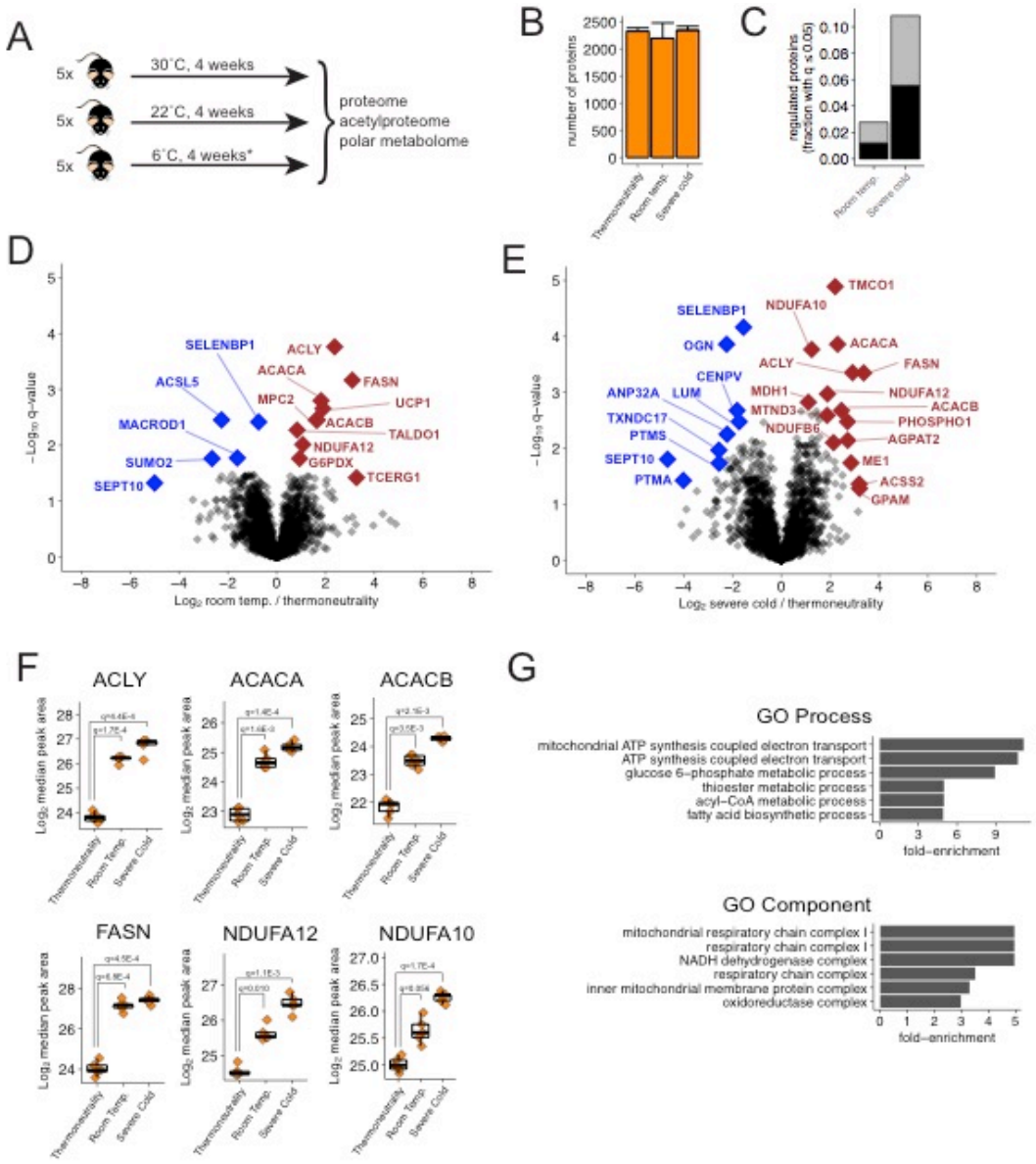

Figure 2.1 Replicate analysis of BAT after room temperature acclimation reveals a core proteome response of thermogenesis. (A) Outline of experimental design. *Temperature was decreased 4°C per week for 4 weeks, such that they were housed at 6°C for the final week. **(B)** Number of identified proteins in each biological condition. Error bars represent standard deviation. **(C)** The fraction of proteins with q ≤ 0.05, either increasing (black) or decreasing (grey), is plotted for the indicated experimental conditions, relative to the thermoneutrality control. **(D-E)** Volcano plot showing the Log_2 fold-change versus the -Log_{10} q-value for all proteins, between the severe cold and thermoneutral conditions **(D)** and between the room temperature and thermoneutral conditions **(E)**. Selected increasing (brown) and decreasing proteins (blue) after severe cold acclimation are highlighted. **(F)** Boxplots of selected proteins after cold acclimation. **(G)** Top terms at 5% FDR from Gene Ontology (GO) enrichment analysis of proteins that were significantly increased at least twofold in mild *or* severe cold versus thermoneutrality.

In addition, the carnitine palmitoyltransferase enzymes CPT1B and CPT2 increase after severe cold acclimation, 2-fold and 1.6-fold respectively (Table S1), suggesting an increase in fatty acid import into mitochondria, which is thought to be rate-limiting for fatty acid oxidation. Thus, manual inspection of proteins related to metabolism provides more detailed insight about glucose and fatty acid metabolism during BAT thermogenesis.

To further characterize the thermogenic proteome, we performed a gene ontology (GO) enrichment analysis for proteins that increase or decrease in *either* mild *or* severe cold. GO Process analysis identifies “mitochondrial ATP synthesis-coupled electron transport”, “glucose 6-phosphate metabolic process”, “acyl-CoA metabolic process”, and “fatty acid biosynthetic process” as being enriched among proteins that increase in mild or severe cold relative to thermoneutrality (Fig 2.1G). Analysis of GO Components for these upregulated proteins shows enrichment of the terms “mitochondrial respiratory chain complex I” and “NADH dehydrogenase complex”, suggesting an overall increase in complex-I proteins (Fig 2.1G). While there are several significantly decreasing proteins, named above, we found that no corresponding GO pathways are enriched in proteins with decreased abundance after cold acclimation. Together, our global proteomics analysis of BAT is consistent with cold acclimation stimulating glucose uptake, and flux towards glycolysis, the pentose phosphate pathway, *de novo* lipogenesis, capacity for fatty acid oxidation, and electron transport.

2.3.2 Mitochondrial proteome remodeling during thermogenesis. Because BAT thermogenesis increases mitochondrial metabolic activity, we used our proteomics dataset to characterize the mitochondrial proteome in response to the different cold acclimation conditions. First, we annotated all measured proteins as either “mitochondrial” or “non-mitochondrial” based on GO Component annotations, and compared the abundance of the median mitochondrial protein to

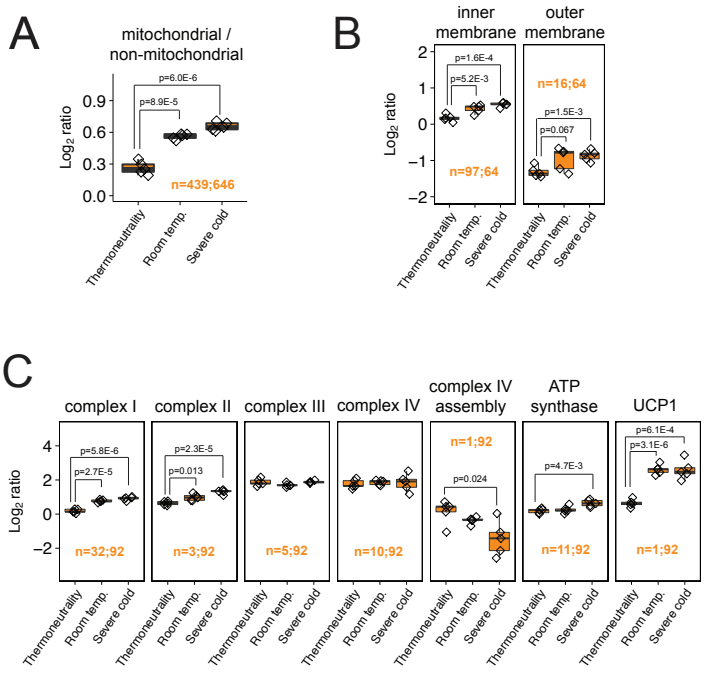

Figure 2.2 Mitochondrial proteins as a whole, and ETC complex-I proteins in particular, increase their relative abundance during thermogenesis. (A) Plot showing changes to the Log_2 ratio of the median mitochondrial to the median non-mitochondrial protein. The number of proteins used to calculate medians for mitochondrial and non-mitochondrial fractions are indicated for each experiment before and after the semicolon, respectively. **(B)** Plot showing the Log_2 ratio of the median inner membrane or outer membrane protein to the median mitochondrial matrix protein. The number of inner/outer membrane proteins and the number of matrix proteins are indicated for each experiment before and after the semicolon, respectively. **(C)** Plot showing the Log_2 ratio of the median ETC complex protein to the median mitochondrial matrix protein. The number of ETC complex proteins and the number of matrix proteins are indicated for each experiment before and after the semicolon, respectively.

the median non-mitochondrial protein across all replicates and conditions. This analysis revealed that mitochondrial proteins significantly increase relative to non-mitochondrial proteins after both mild and severe cold acclimation (Fig 2A). We also examined the relative changes to proteins annotated to different mitochondrial subcompartments. This approach indicates a greater increase in inner mitochondrial membrane proteins, relative to mitochondrial matrix proteins, in cold conditions relative to thermoneutrality (Fig 2B). This suggests that mitochondria in BAT contain more dense cristae after cold acclimation. We also observe a similar, but milder, increase in outer mitochondrial membrane proteins relative to mitochondrial matrix proteins (Fig 2B), suggesting increased surface area to volume ratio that could be due to increased mitochondrial fission.

To further investigate changes to inner mitochondrial membrane proteins, we calculated the ratio of each complex in the ETC to the mitochondrial matrix, using annotation from WikiPathways to define proteins that represent complexes I-IV and the ATP synthase complex. Strikingly, complex I and complex II proteins, but not those from complexes III and IV, increase in response to all cold acclimation conditions (Fig 2C), and show a nearly two-fold enrichment in mitochondria between thermoneutrality and severe cold adaptation. The ATP synthase complex also has a mild cold-dependent increase, which could reflect a compensatory mechanism to generate sufficient ATP in the face of uncoupled respiration (Fig 2C). These results suggest that the stoichiometry of ETC complexes, specifically complexes I and II, is regulated during BAT thermogenesis.

2.3.3 Overlap between the cold-induced transcriptome and proteome. Compared to the thermogenic proteome described above, previously-reported RNA-seq transcriptome analyses of these BAT samples (Sanchez-Gurmaches et al. 2018) contains a similar distribution of fold-changes between conditions (Fig 3A), but a greater percentage of significant changes at a 5%

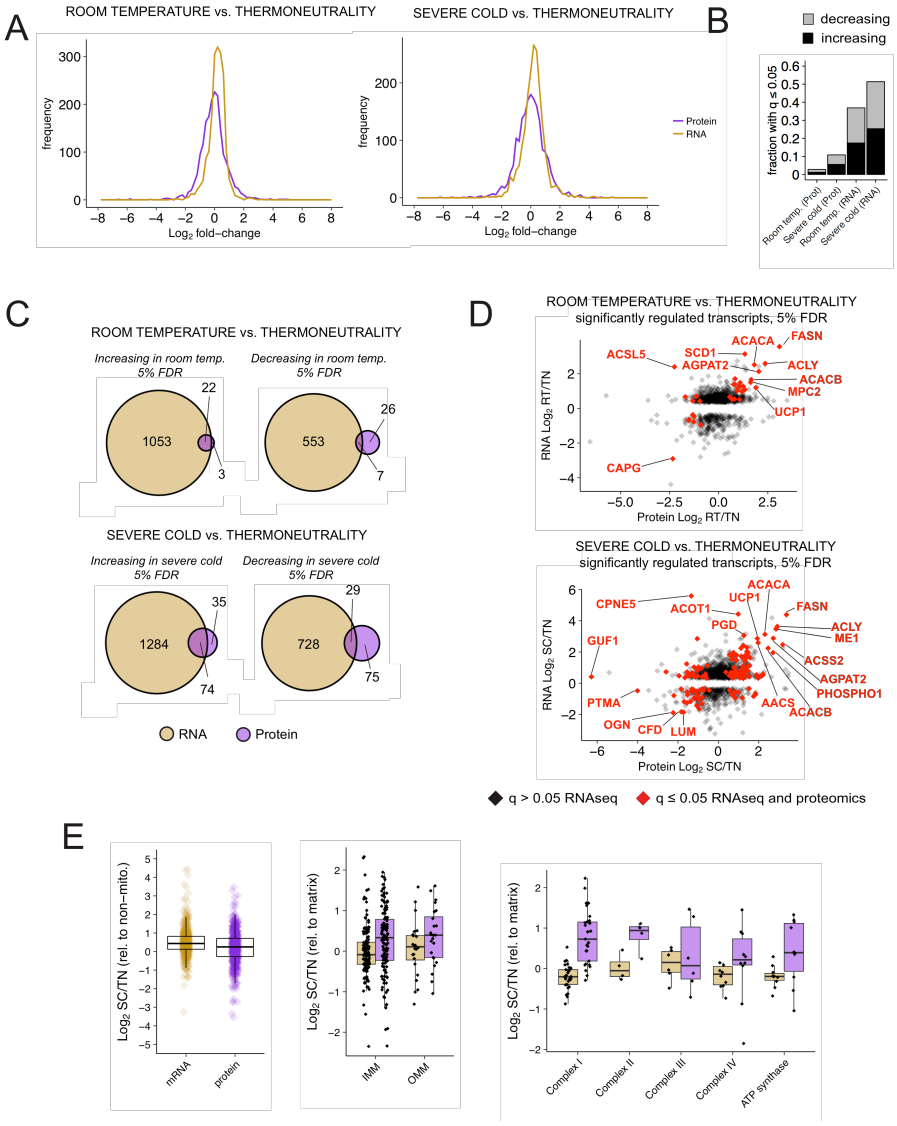

Figure 2.3 Comparison of proteome and transcriptome profiling of 3-temperature cold acclimated mouse BAT. Transcriptome profiling from Sanchez-Gurmaches et al.{SanchezGurmaches:2018kp} was compared to the 3-temp proteomics experiment presented in this study. **(A)** Distribution of Log_2 fold-changes, both room temperature (left) and severe cold (right) vs. thermoneutrality, for the proteome and transcriptome profiling datasets. **(B)** FDR q-values were compared between each condition and the thermoneutrality control. The fraction of proteins or transcripts with q ≤ 0.05 is plotted for the indicated experimental conditions. **(C)** Euler plots comparing significantly (q ≤ 0.05) upregulated or downregulated proteins and their respective transcripts. Only transcripts whose proteins were detected in the proteomics experiment are shown. **(D)** Transcripts that increase after room temperature (top) or severe cold (bottom) acclimation are plotted to compare fold-changes between the transcriptome and proteome datasets. Sites that are significantly (q ≤ 0.05) regulated in both experiments are shown in red, even if their direction of change differs. **(E)** Analysis of mRNA and protein levels in mitochondrial sub-groups. Left: the ratio of mitochondrial to non-mitochondrial mRNA/protein). Middle: the ratio of inner mitochondrial membrane (IMM) or outer mitochondrial membrane (OMM) to mitochondrial matrix mRNA/protein. Right: the ratio of ETC complexes to mitochondrial matrix mRNA/protein.

FDR threshold (Fig 3B). 88% of proteins that significantly increase ($q \leq 0.05$) in room temperature acclimation, and 68% of those that significantly increase in severe cold acclimation, also increase at the mRNA level (Fig 2.3C). Among the overlapping mRNA-protein pairs that most significantly increase in cold in both the proteomic and transcriptomic analyses are fatty acid synthesis enzymes (including ACLY, ACSS2, ACACA, ACACB, FASN, SCD1); AGPAT2, which functions in triacylglyceride synthesis; and UCP1 (Fig 2.3D). Correlation between mRNA-protein pairs is less consistent in transcripts or proteins that decrease after mild or severe cold acclimation (Fig 2.3C), which may suggest regulation via protein translation or degradation. Indeed, a recent study found that proteasomal activity increases in cold-adapted BAT, and is important for effective thermogenesis(Bartelt et al. 2018). Unlike at the protein level, there was no increase in transcripts encoding for inner or outer mitochondrial membrane, or ETC proteins, relative to mitochondrial matrix proteins after cold acclimation (Fig 2.3E). This suggests that regulation of the mitochondrial proteome with BAT activation is post-translational.

2.3.4 Mitochondrial protein acetylation increases during cold acclimation. Because multiple routes to acetyl-CoA generation are increased in active BAT, we hypothesized that cold adaptation is also associated with significant changes in protein acetylation. To test how BAT activation affects protein acetylation patterns, we digested total BAT protein with trypsin, enriched for acetylated peptides using anti-acetyl-lysine antibodies, then quantified their amount using label-free mass spectrometry. Across all conditions, the number of acetylation sites, or acetylsites, identified per run ranged from 794 to 1904, with higher number of identified acetylation sites in the severe cold condition (2. 4A). To account for the fact that acetylated proteins might themselves change in abundance between conditions, acetylsite quantifications were normalized to the level of the respective protein for that replicate. After this normalization,

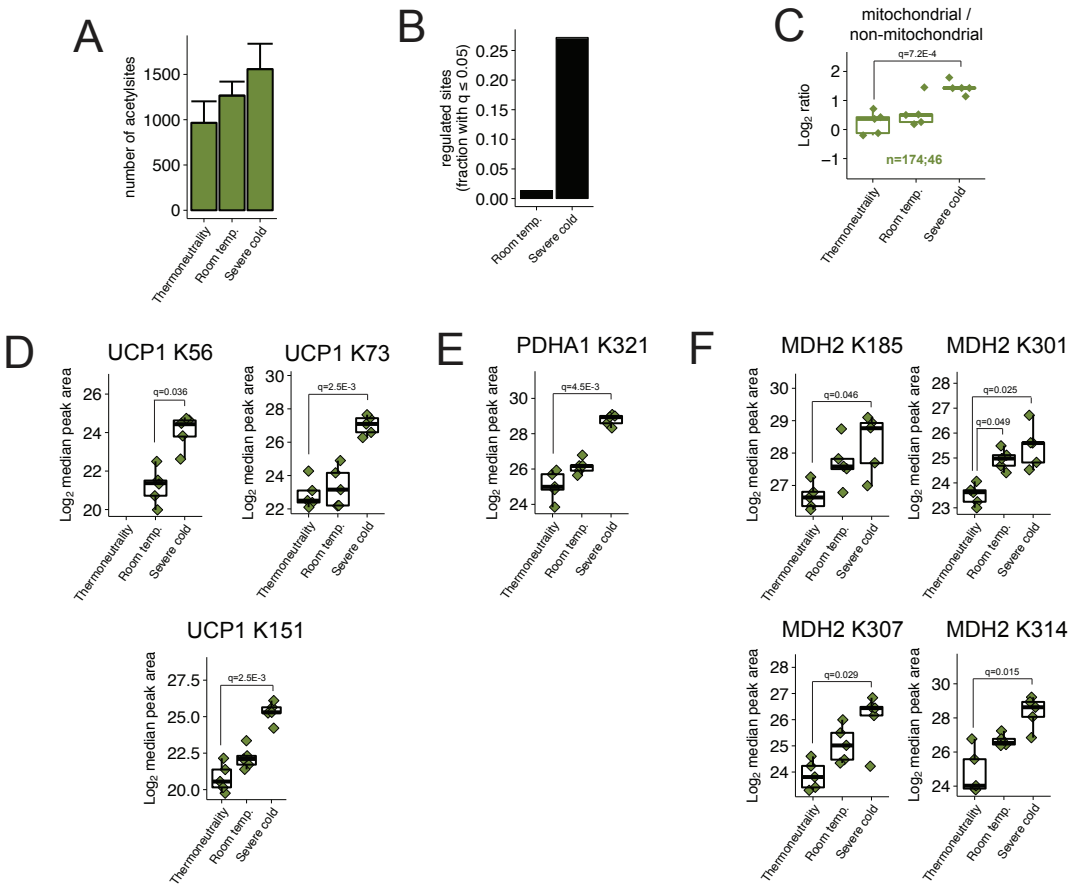

Figure 2.4 Mitochondrial protein acetylation increases during thermogenesis. (A) Number of identified acetylsites in each biological condition. Error bars represent standard deviation. **(B)** The fraction of acetylsites with q ≤ 0.05, either increasing (black) or decreasing (grey), is plotted for the indicated experimental conditions, relative to the thermoneutrality control. Note that the decreasing (grey) portion is barely visible. **(C)** Log_2 ratios of mitochondrial to non-mitochondrial protein-normalized acetylated peptide forms, across all conditions and experiments. The number of mitochondrial and non-mitochondrial proteins is indicated for each experiment before and after the semicolon, respectively. **(D)** Acetylation on UCP1 K56, K73, and K151 and is shown for all three temperature conditions. **(E)** Acetylation on PDHA1 K321 is shown for all three temperature conditions. **(F)** Acetylation on four MDH2 sites is shown for all three temperature conditions.

we calculated q-values for room temperature and severe cold conditions relative to thermoneutrality. Cold-induced thermogenesis caused a widespread increase in protein acetylation in BAT. At 5% FDR, over 25% of protein-normalized acetylation sites increase in severe cold acclimation, while only 1% increase in room temperature acclimation (Fig 2.4B). GO enrichment analysis on acetylsites that increase after severe cold acclimation reveals terms related to the mitochondria and fatty acid catabolism (Figs S2.2A, S2.2B). Acetylation on mitochondrial proteins, relative to non-mitochondrial proteins, increases over 2-fold in response to severe cold acclimation (Fig 2.4C).

Interestingly, UCP1 is hyperacetylated after cold acclimation on K151 (22.6-fold increase after severe cold), K73 (17.7-fold increase), and K56 (7.2-fold increase from mild to severe cold) (Fig 2.4D). This is the first time that UCP1 acetylation during cold-induced thermogenesis has been reported. UCP1 localizes to the inner mitochondrial membrane, and all three of these sites are on the mitochondrial matrix-facing side. Several other hyperacetylated mitochondrial proteins are particularly noteworthy based on the number of acetylsites that significantly increase. In the TCA cycle, two isocitrate dehydrogenase isoforms are highly hyperacetylated in cold acclimation; IDH2, with 12 acetylsites, and IDH3 alpha subunit, with 8 acetylsites; the alpha subunit of the fatty acid oxidation trifunctional enzyme, HADHA, is hyperacetylated at 12 sites; and dihydrolipoyl dehydrogenase (DLD), which functions in branch chain amino acid catabolism, is hyperacetylated at 8 sites. While these acetylation sites have not been extensively studied, the number of cold-dependent acetylation sites on IDH isoforms, HADHA, and DLD suggest suggests a potential to affect protein function.

Relative to mitochondrial protein acetylation, we detected few changes in cytoplasmic protein acetylation (Figs S2.2C, S2.2D). Histone H3 acetylation regulates gene expression; however, we did not detect significant changes to histone H3 acetylation relative to its total protein levels

(Figs S2.2E, S2.2F). Because of low nuclear histone abundance, we speculate that a higher resolution analysis of histone marks at specific promoters via techniques such as ChIP-seq is required to fully assess acetylation-mediated epigenetic changes that might be associated with thermogenesis. These findings suggest that the nuclear-cytoplasmic acetyl-CoA generated in active BAT may predominantly be used for *de novo* lipid synthesis rather than protein lysine acetylation, and that the increase in mitochondrial protein acetylation relative to other compartments may be driven by the robust increase in mitochondrial nutrient (e.g. fatty acid, pyruvate) oxidation also associated with thermogenesis.

We also identified cold-induced acetylation sites on mitochondrial proteins with previously characterized metabolic functions. For example, acetylation of the pyruvate dehydrogenase E1 alpha subunit (PDHA1) on K321 has been shown to be inhibitory, and implicated in the Warburg effect in cancer cells(Fan et al. 2014). PDHA1 K321 acetylation increases in severe-cold-acclimated BAT (Fig 2.4E). Inhibiting PDHA1 in BAT could thus temper the flux from glycolysis to acetyl-CoA synthesis, and favor other uses of glycolytic intermediates. Another example of hyperacetylation with previously characterized function is on the mitochondrial enzyme malate dehydrogenase (MDH2). MDH2 functions in the TCA cycle and as part of the malate-aspartate shuttle that transports NADH reducing equivalents between the mitochondria and cytosol. MDH2 has four acetylation sites that, when simultaneously mutated to arginine, decrease its activity (Zhao et al. 2010). We find that all four of these acetylsites on MDH2 significantly increasing in severe-cold (Fig 2.4F). The aforementioned cold-induced acetylation sites on PDHA1 and MDH2 could be important for regulating glucose and NADH metabolism, respectively, in the context of BAT thermogenesis.

2.3.5 Analysis of independently temperature-acclimated mice confirms key proteomics and acetylproteomics findings. To solidify our findings, we repeated our BAT proteome and

acetylproteome analysis on an independent mouse cohort. This second experiment was largely similar to the previous one with regards to animal age, diet, and housing conditions (see methods in 2.4), but here we increased the number of replicates and focused on the two temperatures that are relevant to humans(Cannon & Nedergaard 2011; Sanchez-Gurmaches et al. 2016): thermoneutrality and room temperature.

We first compared the thermogenic proteome datasets and find they are of similar scope and quality as they contain a similar number of identified proteins (Fig S2.3A), and have a similar degree of quantitative reproducibility indicated by the distribution of coefficients of variation (Fig S2.3B). The percentage of significantly regulated proteins is greater in the second experiment (Fig S2.3C); and the magnitude and directionality of proteins that are significantly altered in at least one experiment are in good agreement (Fig S2.3E). Thirteen proteins significantly increase in both experiments, including *de novo* lipogenesis enzymes ACACA, ACACB, and FASN, and the early glycolytic enzymes HK2 and GPI. Relevant proteins that significantly increased in one dataset (e.g. ACLY, ACSS2, CPT1B and CPT2), also show an increase in the other dataset. We found 2 proteins significantly decreasing in both datasets: the extracellular matrix protein FBN2 and the cytosolic selenium-binding protein SELENBP1 (Fig S2.3D). The cold-stimulated increase in mitochondrial proteins relative to non-mitochondrial proteins is also conserved between both data sets (Fig S2/3G), as is an increase in the amount of outer mitochondrial membrane proteins (Fig S2/3H) and complex I proteins (Fig S2.3I) relative to mitochondrial matrix proteins.

Mitochondrial protein hyperacetylation occurs during mild cold acclimation in the second experiment, to an even greater extent than in the first experiment. Importantly, the summary statistics for acetylproteome measurements are comparable between the two datasets, both in terms of the number of identified sites (Fig S2.4A) and the quantitative reproducibility (Fig

S2.4B). While the number of significantly regulated sites is greater in the second experiment (Fig S2.4C), due in part to increased replicates, the global increase in mitochondrial protein acetylation over cytoplasmic/nuclear protein acetylation is consistent (Fig S2.4D). Specific acetylation sites of interest, discussed above –PDHA1 K321; MDH2 K185, K301, K307 and K314– all significantly increase in room temperature relative to thermoneutrality acclimation in the second experiment (Fig S2.4E-G). Expression of UCP1 between chronic thermoneutral and room temperature housing showed no differences in this experiment (Fig S2.5A), yet the significant increase in acetylation on UCP1 K151 was conserved (Fig S2.5B). The second experiment also revealed a 13.6-fold increase in acetylation on UCP1 K67 after mild cold acclimation (Fig S2.5B) that did not pass our significance threshold in the first experiment. Taken together, these data add confidence to our proteomics and acetylproteomic findings and solidify many of our hypothesis on how thermogenesis regulates BAT metabolism.

2.3.6 Cold acclimation alters glycolytic intermediates, nucleotide triphosphates, and electron transporters in BAT. Next we explored the BAT metabolic landscape by measuring 124 polar metabolites extracted from BAT by LC-MS/MS. Measured metabolites include intermediates to glycolysis, the TCA cycle, and amino acid and nucleotide metabolism. 23 metabolites increase in abundance in severe-cold-adapted BAT relative to thermoneutrality at 5% FDR while 13 metabolites decrease. Cyclic AMP is among those increasing with cold acclimation consistent with its role in transducing the beta-adrenergic stimulus to protein kinase A (PKA) during thermogenesis (Figs 2.5A, S2.6A). The nucleotide triphosphates ATP, GTP, and UTP all decrease significantly at least 6-fold in cold-adapted BAT (Figs 2.5A, S2.6B), which is consistent with the decreased oxidative phosphorylation that accompanies uncoupled respiration(Lindberg et al. 1967). The corresponding loss of nucleotide triphosphates other than ATP would be an

expected equilibrium state due to the action of nucleotide-diphosphate kinase(Ray & Mathews 1992).

Several glycolytic intermediates decrease with cold-acclimation including fructose 1,6-bisphosphate, 3-phosphoglycerate, phosphoenolpyruvate, and a saccharide that could be either fructose-6-phosphate (glycolysis) or glucose-1-phosphate (glycogen metabolism) (Figs 2.5A, S2.6C). Decreased steady-state levels of glycolytic metabolites is consistent with increased glycolytic flux. In contrast, glycerol 3-phosphate increases 4.2-fold with severe cold acclimation (Fig 2.5B). Glycerol 3-phosphate synthesis occurs by several mechanisms, including via glycolysis, and is a precursor to triglyceride synthesis. In rats, glucose-derived glyceride levels in BAT increased after the tissue was activated by a high-fat cafeteria diet(Chaves et al. 2012). Thus, it is possible that synthesis of glycerol 3-phosphate and its subsequent incorporation into triglycerides is also an important role for glucose in cold-activated BAT. Another possibility is that glycerol 3-phosphate increases by hydrolysis of triglycerides due to the increased lipolysis rate. In addition to being a precursor to triglycerides, glycerol 3-phosphate is also an electron carrier that can transfer reducing equivalents between the mitochondria and cytosol, where it can be consumed in a reaction, along with NAD^+, to generate NADH and dihydroxyacetone phosphate. Interestingly, two other reduced electron carriers increase after cold acclimation: succinate and NADH. Succinate increases 3.6-fold in the severe cold (Figs 5A, 5F, Table S5), while NADH increases 3.9-fold with $q = 0.078$ (Fig 2.5B). NAD^+ does not change in response to cold acclimation (Fig 2.5B). This is interesting, given the importance of reducing equivalents in driving the ETC, as well as their potential for participating in product inhibition of the enzymes that generate them. In sum, these results (summarized in Fig 2.6) indicate significant changes to glycolysis, nucleotide triphosphates, and redox biochemistry in BAT following cold acclimation.

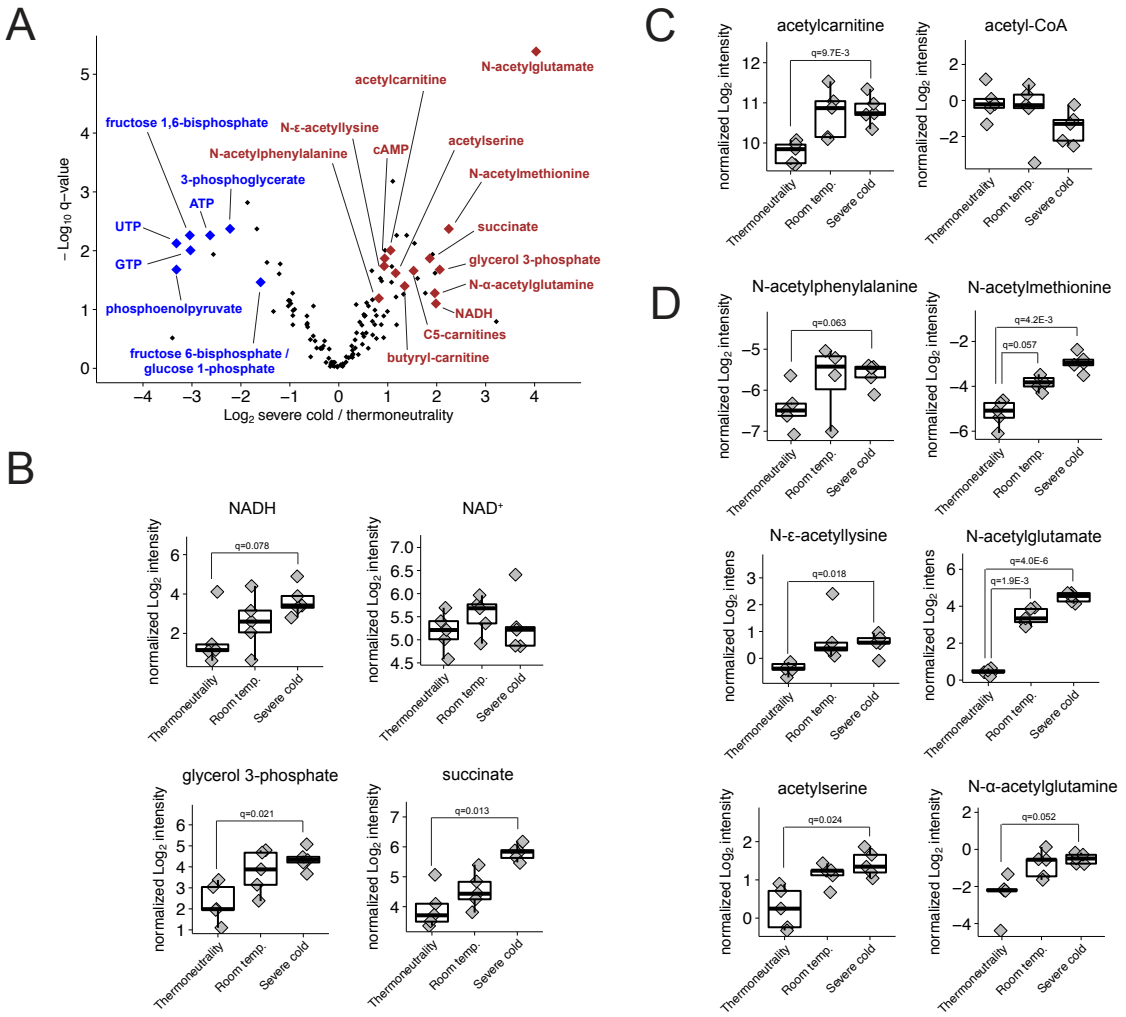

Figure 2.5 Polar metabolite measurements reveal many changes to acetylated metabolites and reducing equivalents. (A) Volcano plot showing the Log_2 fold-change versus the -Log_{10} q-value for all metabolites, between the severe cold and thermoneutrality conditions. Selected increasing (brown) and decreasing (blue) metabolites are indicated. **(B)** Barplots showing quantifications for metabolites involved with cellular redox reactions in all five conditions from both experiments. **(C)** Barplots showing quantifications for acetylcarnitine and acetyl-CoA in all five conditions from both experiments. **(D)** Barplots showing quantifications for acetylated amino acids in all five conditions from both experiments.

2.3.7 Increases to acetylated metabolites during thermogenesis suggests altered acetyl-CoA flux. Acetyl-CoA levels do not change between the thermoneutral and room temperature conditions and mildly decrease with severe cold (Fig 2.5C, 2.6A). Thus, while the rate of acetyl-CoA synthesis would be expected to rise with cold due to the increase in fatty acid oxidation and *de novo* lipogenesis that is characteristic of active BAT, the constant or decreasing acetyl-CoA abundance likely reflects increased acetyl-CoA flux towards protein acetylation and perhaps other metabolites. Acetyl-CoA is a highly reactive metabolic intermediate due to the high energy thioester bond linking its acetyl group to the CoA moiety, and there are several cellular reactions that can consume it (Fig 2.6A); thus its availability must be under tight control. Indeed, we find increased acetylcarnitine and acetylated amino acids in thermogenic BAT. Acetylcarnitine is generated in the mitochondria from acetyl-CoA and carnitine by the enzyme carnitine acetyltransferase, and exported from the mitochondria to buffer against high mitochondrial acetyl-CoA levels(Pearson & Tubbs 1967). Acetylcarnitine is upregulated 2.1-fold in severe-cold-acclimated BAT, suggesting mitochondrial acetyl-CoA synthesis may exceed its utilization by the TCA cycle in cold-stimulated BAT (Fig 2.5C). Interestingly, we also find that four acetylated amino acids also significantly increase in abundance with cold: N-acetylglutamate (16-fold increase), N-acetylmethionine (4.8-fold), acetylserine (2.2-fold), and N-ε-acetyllysine (1.9-fold) (Figs 2.5D, 2.6A). Two more acetylated amino acids (acetylphenylalanine and N-α-acetylglutamine) increase by greater than 2-fold (Fig 2.5D).

BAT thermogenesis may lead to accumulation of some metabolites upstream of acetyl-CoA as well, as the branched chain amino acids valine, leucine, and isoleucine, which are catabolized to acetyl-CoA, all increase with cold. In addition, amino acids could be generated by protein degradation, which has been shown to be increased in active BAT(Bartelt et al. 2018). While we do not measure subcellular fractions of these metabolites, correlation with acetylcarnitine and

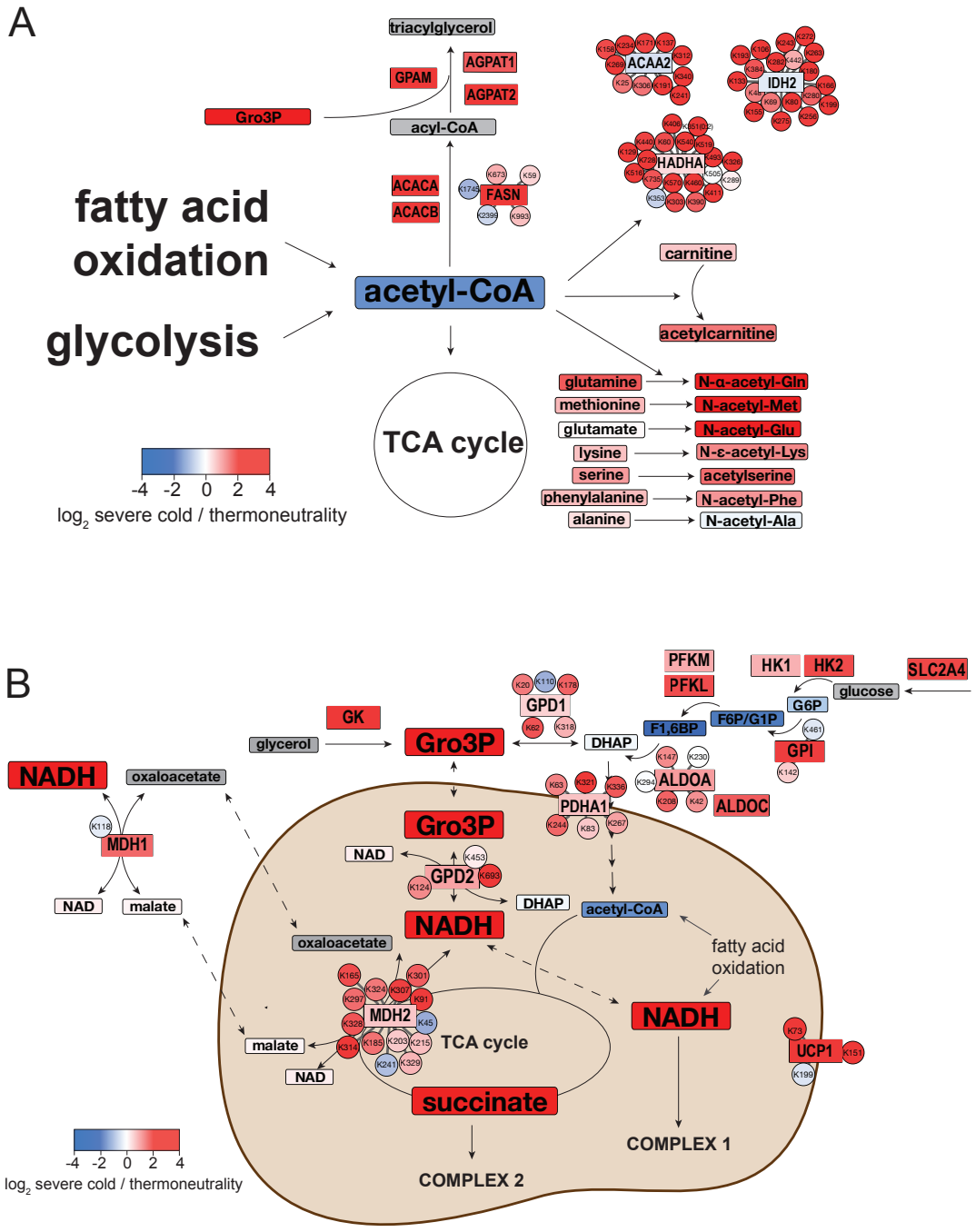

Figure 2.6 Chronic cold acclimation alters acetyl-CoA usage and redox metabolism in BAT. (A) Schematic showing quantitative data for select metabolites, proteins, and acetylation sites for selected pathways that consume acetyl-CoA. **(B)** Schematic showing quantitative data for select metabolites, proteins, and acetylation sites that are connected to cellular redox.

mitochondrial protein acetylation levels suggest a role for acetylated amino acids in buffering mitochondrial acetyl-CoA.

2.3.8 Functional analysis of UCP1 acetylation sites. Finally, given the BAT specificity and function of UCP1 in thermogenesis, and the cold-induced regulation observed for its four acetylation sites detected, we wondered if these sites might be functionally relevant. When normalized to protein levels, acetylation on K56, K67, K73, and K151 increase in response to either mild or severe cold, with $q \leq 0.05$ in either of the two proteomics experiments (Figs 2.4D, S2.5B). To test potential functional relevance of UCP1 acetylation on these sites, we analyzed exogenously expressed UCP1 mutants in 293T cells. Specifically, we mutated K56, K67, K73 and K151 to either arginine (UCP1-4KR), which blocks acetylation, or glutamine (UCP1-4KQ), which mimics acetylation. We also generated UCP1-3KR and UCP1-3KQ by only mutating K56, K67 and K73 (Fig 2.7A). After expressing the recombinant UCP1 mutant in 293T cells, Western blot analysis indicated that the 3KR and 4KR mutants express at similar levels to the UCP1-WT control. However, both UCP1-3KQ, and more dramatically UCP1-4KQ, express at significantly lower levels (Fig 2.7B). This is not due to differences in mRNA expression because UCP1-4KQ and -3KQ show higher transcription than control (Fig 2.7C). To test whether acetylation alters UCP1 stability, we treated the 293T cells expressing UCP1-WT, -4KR and -4KQ with cycloheximide (CHX) to inhibit *de novo* protein synthesis and estimate UCP1 protein half-lives. We observe that the acetyl-mimetic mutant (UCP1-4KQ) has a shorter half-life relative to UCP1-WT, while UCP1-4KR has a longer half life (Fig 2.7D). While the exact mechanism of how acetylation may influence UCP1 stability remains to be determined, and limitations of overexpressing wild-type and mutant UCP1 *in vitro* are duly noted, our results show preliminary evidence that cold-induced acetylation of UCP1 could have functional relevance.

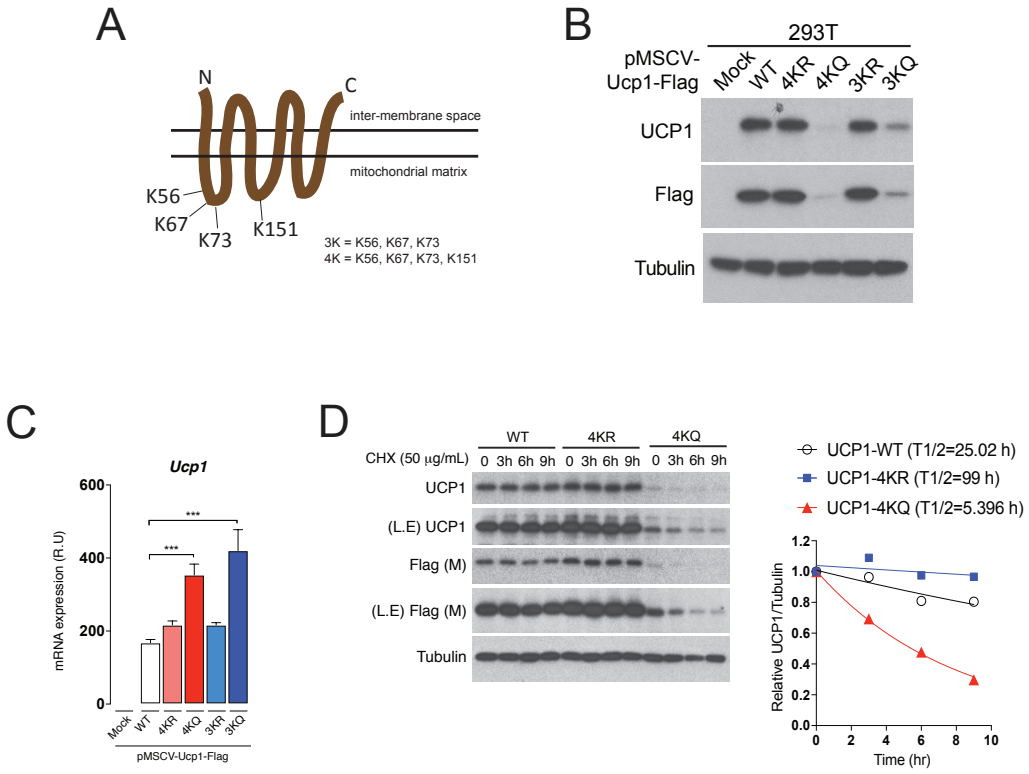

Figure 2.7 Four cold-dependently hyperacetylated lysine residues on UCP1 are important for stability. (A) Outline of UCP1 acetylation mutant constructs design. Note that all four acetylation sites are predicted to exist on the mitochondrial matrix side of the IMM. **(B)** Immunoblots of UCP1 wild-type or mutant constructs expressed in 293T cells. **(C)** mRNA expression levels, measured by qPCR, of UCP1 wild type or mutant constructs expressed in 293T cells. **(D)** Immunoblot (left) and quantification (right) showing protein expression of UCP1 wild-type or mutant constructs in a time series after cycloheximide (CHX) treatment. Half-lives of UCP1 proteins are calculated in the graph. In all immunoblot analysis, expression of alpha-tubulin was used as a loading control.

2.4 Discussion

Brown adipose tissue is of great interest as a potential therapeutic target for type-2 diabetes and other metabolic diseases associated with obesity, yet the molecular underpinnings of BAT metabolic activity have not been fully elucidated. Here, we sought a better understanding of the BAT molecular landscape by comparing proteome, acetylproteome, and metabolome data between inactive and different degrees of cold-activated BAT. We show that cold-induced thermogenesis has significant and reproducible effects on all three "omics" measurements taken in this study. Among many findings, our integrative analysis suggests a broad reprogramming of acetyl-CoA metabolism during thermogenesis. This conclusion is supported by (1) the upregulation of enzymes related to *de novo* lipogenesis, which consumes cytosolic acetyl-CoA, (2) increases to carnitine palmitoyltransferases CPT1B and CPT2, suggesting increased capacity for fatty acid oxidation, which generates mitochondrial acetyl-CoA, (3) the upregulation of mitochondrial protein acetylation, and (4) increases in acetylated metabolites, including acetylcarnitine as well as several acetylated amino acids.

Many mitochondrial proteins were hyperacetylated in BAT after cold acclimation, including a few sites on metabolic enzymes that have previously-characterized functions. We find that PDHA1 K321 becomes hyperacetylated after cold-acclimation relative to PDHA1 protein levels (Fig S4E). PDHA1 acetylation at this site has been shown to promote a transformed phenotype in cancer cell lines, likely via the Warburg effect(Ozden et al. 2014). A Warburg-like effect could exist in cold-activated BAT, whereby glycolytic intermediates could be directed to other key metabolites. Another example of hyperacetylation at previously-characterized sites is on MDH2. We report that several lysine residues on the mitochondrial malate dehydrogenase, MDH2, are hyperacetylated in cold-adapted BAT (Fig 2.4F). Some of these sites have been shown to increase the activity of the MDH2 reverse reaction, which consumes NADH and generates

malate, which is shuttled out of the mitochondria (Zhao et al. 2010). This could be a mechanism by which NADH product inhibition is overcome in active BAT (Fig 2.6B). Finally, we found cold-dependent hyperacetylation on four sites on UCP1, and through mutagenesis experiments and cell culture expression, we demonstrate increased degradation of UCP1 with acetylation-mimicking mutations, suggesting that acetylation at these residues may influence the stability of UCP1 and be functionally relevant.

BAT thermogenesis is centered around the ETC. Our metabolomics data revealed cold-dependent increases to three ETC substrates: NADH, succinate, and glycerol-3 phosphate (Fig 2.6B). This could reflect metabolic reprogramming geared toward generating substrates for electron transport. In addition, succinate was recently shown to be sequestered from circulation in BAT, where it subsequently potentiates thermogenesis via reactive oxygen species (ROS) generation by complex II (Mills et al. 2018). Alongside increases in substrates for electron transport, we observe changes to ETC complex stoichiometry that could also affect the generation of ROS. ETC complexes have been shown to assemble in cells as supercomplexes (Letts & Sazanov 2017). One study in neurons and astrocytes showed that adjusting expression of a complex-I protein affects the presence of complex-I in a free state versus in supercomplexes, which in turn affects the production of ROS (Lopez-Fabuel et al. 2016). ROS production increases in BAT during cold acclimation, and has been shown to be necessary for complete induction of thermogenesis (Chouchani et al. 2016), but our knowledge of the mechanisms of ROS production is incomplete. We observe increases to complexes I-II of the ETC, and not other complexes, which could be a way to adjust ETC stoichiometry and consequent production of ROS during thermogenesis.

Turning to the observed acetyl-CoA reprogramming in thermogenesis, another mechanism by which cells regulate mitochondrial acetyl-CoA levels is through the action of carnitine acetyl-

transferase (CRAT). One recent study showed that deletion of CRAT in skeletal muscle leads to an increase in acetyl-CoA and a concomitant increase in mitochondrial protein acetylation in response to high-fat feeding (Davies et al. 2016). In our study, acetylcarnitine levels increase as a result of mild and severe cold adaptation suggesting a key role for CRAT in buffering mitochondrial acetyl-CoA pools during BAT thermogenesis. Like acetylcarnitine, acetylated amino acids increase in BAT after cold acclimation. No one has reported amino acid acetylation as a means to dispense of excess acetyl-CoA, but it is a plausible mechanism that could work in parallel with acetylcarnitine synthesis. While it is also possible that the increase in alpha-amino acetylated amino acids is the result of increased cleavage of N-terminally acetylated protein residues, we found no evidence of increased N-terminal acetylation in the proteomics data (Fig S7). Thus, we postulate that conversion to citrate and subsequent cytosolic *de novo* lipogenesis, as well as the acetylation of amino acids, carnitine, and lysine residues on mitochondrial proteins, function to consume mitochondrial acetyl-CoA generated from glucose and fatty acids during BAT thermogenesis (Fig 2.6A). This would allow oxidative metabolism to continue with minimized product inhibition by acetyl-CoA. Interestingly, the most upregulated metabolite in our dataset is N-acetylglutamate, which stimulates urea cycle activity in the liver by allosterically activating the enzyme carbamoyl phosphate synthetase (HALL et al. 1958). Given that proteasomal activity is known to increase in active BAT (Bartelt et al. 2018), urea cycle activity may be necessary to dispose of nitrogen byproducts from amino acid catabolism. In the future, it will be interesting to measure acetyl-CoA in distinct subcellular fractions (e.g. mitochondrial, nuclear, and cytosolic), as well as flux of reactions generating and consuming acetyl-CoA in order to characterize the connection between acetyl-CoA and acetylated amino acids. In addition, the dramatic increase of N-acetylglutamate suggests that simultaneous, multi-omics analysis of multiple tissues could help to elucidate novel inter-organ crosstalk mechanisms during thermogenesis.

In conclusion, we demonstrate that cold-induced thermogenesis profoundly alters the BAT proteome by increasing the levels and/or the acetylation of specific proteins. We also describe many changes in key metabolites in response to cold-induced thermogenesis that provide important clues to how BAT fuels its metabolism. This work emphasizes the metabolic flexibility of BAT and has important implications for development of therapeutic strategies targeting BAT metabolism to fight metabolic diseases.

2.5 Materials and Methods

2.5.1 Mice. For all experiments, C57BL/6J mice were used. Mice were housed in the Animal Medicine facilities of the UMMS in a clean room set at 22ºC and 45% humidity under daily 12h light/dark cycles in ventilated racks with cages changed every two weeks. Mice were fed the facility chow diet. For the four week temperature acclimation experiments, mice at 10 weeks old were simultaneously housed in two rodent incubators (RIT33SD, Powers Scientific) within the Animal Medicine facilities of the UMMS. One of them had the temperature adjusted to 30ºC (thermoneutrality group). Another incubator had its temperature decreased by four degrees weekly until reaching 6ºC at which temperature the mice stayed for a week (severe cold group). Room temperature group mice were co-housed in the same facility as the mice in rodent incubators. Mouse cages were changed weekly using components pre-adjusted to temperature. No cage enrichment was used in this set of experiments. Mice were sacrificed at 14 weeks old in the morning in random fed conditions. For the “2-temp” experiment, mice were housed two per cage, with one nestlet per cage, at ambient room temperature. They were fed D12450J (Research Diets). At 8 weeks of age, mice in the thermoneutral group were transferred to a temperature and humidity controlled 30ºC room. Cages were changed weekly using components pre-adjusted to temperature. Mice in the thermoneutral and room temperature

groups were sacrificed at 12 weeks of age. All animal experiments were approved by the University of Massachusetts Medical School Institutional Animal Care and Use Committee.

2.5.2 Analysis of proteome and acetyl-proteome. For proteomics analysis, mouse interscapular BAT was homogenized in ice-cold lysis buffer using a plastic pestle in a microcentrifuge tube. The lysis buffer contained 8 M urea, 50 mM Tris pH 8.2, Roche complete mini EDTA-free protease inhibitor cocktail, phosphatase inhibitors (50 mM β-glycerophosphate, 1 mM sodium orthovanadate, 10 mM sodium pyrophosphate, 50 mM sodium fluoride), and nicotinamide (class-III histone deacetylase inhibitor). Ground tissue was then sonicated for three cycles of 20 seconds each, chilled on ice for ~10 min, and clarified by centrifugation at 16,000 x g at 4°C. Protein concentration was measured at this stage using the BCA Assay (Pierce). Protein cysteine residues were then reduced using 5 mM dithiothreitol (DTT) for 45 min at 55°C and alkylated using 15 mM iodoacetamide for 30 min at room temperature in the dark. Excess iodoacetamide was quenched with an additional 5 mM DTT at room temperature for 15 min. Samples were then diluted 5-fold in 50 mM pH 8.2 Tris, and digested with 5 µg/mL trypsin for 16 hours at 37°C, after which they were quenched by adding 10% trifluoroacetic acid to a pH of <2. Due to precipitated debris at the low pH, peptide samples were clarified by centrifugation at 3,500 x g at 4°C. Samples were then de-salted using Waters Sep-Pak tC18 cartridges (50 mg packing material), dried by vacuum centrifugation, and stored at -20°C until further use. For acetylation analysis, 0.5 mg of dried peptides were dissolved in 0.5 mL of ice-cold immuno-affinity purification (IAP) buffer (50 mM MOPS-NaOH, pH 7.2, 10 mM Na_2HPO_4, and 50 mM NaCl). Anti-acetyl-lysine agarose beads (ImmuneChem, lot #061214) were prepared by washing with cold IAP buffer. Approximately 25 µL of bead slurry was used per sample. Peptides and anti-acetyl-lysine beads were incubated on a rotating mixer for 2 hours at 4°C, washed five times with 1 mL ice-cold IAP buffer, followed by one wash with 1 mL phosphate

buffered saline (Sigma-Aldrich). Acetylated peptides were eluted two times with 0.15% trifluoroacetic acid for a total of 100 µL, and desalted using four cut-out layers of C18 Empore disks in a Stage-tip configuration (Rappsilber et al. 2003).

All liquid chromatography-tandem mass spectrometry (LC-MS/MS) experiments were done on a EASY-nLC 1000 (Thermo Scientific) coupled to a Q-Exactive mass spectrometer (Thermo Scientific). LC was performed with a 40 cm long, 100 µm inner diameter column packed in-house with Reprosil C18 1.9 µm beads (Dr. Maisch GmbH), with a column oven set to 50°C. Whole proteome and acetylation analyses were done using 90 minute LC-MS/MS runs, including column washing and equilibration. Prior to LC-MS/MS analysis, peptide samples were dissolved in a solution with 4% formic acid and 3% acetonitrile. For whole proteome analysis, samples were separated with a gradient of 9% to 32% acetonitrile in 0.15% formic acid over 62 minutes. For acetyl-proteome analysis, the gradient was 12% - 40% acetonitrile over 64 minutes. MS acquisition was performed using data-dependent acquisition with a “Top-20” method and 40 s dynamic exclusion. Precursor fragmentation was performed using higher-energy collisional dissociation with a 27% normalized collision energy. Whole proteome MS/MS acquisition was performed as follows: full-scan MS was acquired between 300-1500 m/z at 70,000 resolution, with a 3×10^6 automatic gain control (AGC) target and 100 ms maximum injection time. MS/MS acquisition was performed with a 2 m/z isolation window at 17,500 resolution, with a 5×10^4 AGC target and 50 ms maximum injection time. All MS data was collected in centroid mode. MS for acetyl-proteome analysis was performed similarly to the whole proteome analysis with the following differences: data-dependent acquisition was done with a “Top-10” method with 30 s dynamic exclusion, and the MS/MS maximum injection time was 100 ms. Proteome and acetylproteome MS analysis for the two-temperature validation experiment was done in technical duplicate.

Raw files were converted to mzXML format and searched using Comet (Eng et al. 2013) against the mouse SwissProt database including isoforms (downloaded May 10, 2015). Methionine oxidation was treated as a variable modification, and carbamidomethylation of cysteine residues was treated as a constant modification. In the case of acetyl-proteome analysis, acetylated lysine residues were treated as a variable modification. Trypsin digestion was defined with cut-sites at lysine/arginine except when followed by proline. Precursor mass tolerance was set to 50 ppm, and fragment mass tolerance was 0.02 Daltons. Search results were filtered using Percolator (Käll et al. 2007) to obtain a list of peptide-spectrum matches at a <1% false discovery rate. Acetylation site localization was performed using an in-house implementation of Ascore (Beausoleil et al. 2006) that admits any post-translational modification setting, where sites with an Ascore ≥ 13 ($p \leq 0.05$) were considered localized. Quantification was performed using ThunderQuant, an in-house developed software for peptide quantification that relies on MS1 peak area integration. Peptide quantifications were pooled into protein quantifications, where the median peptide for each protein was taken to represent the protein. Protein quantifications were normalized to the total signal from each run. Acetylated peptides were pooled into acetylation isoforms, referred to “acetylsites” in the text for simplicity, if they have overlapping sequences and the same acetylation sites. If multiple unique peptides corresponded to an acetylation isoform, the median peptide was used for quantification. Acetylation isoforms were not normalized to the total signal from each run, because the total amount of acetylation, and the number of identified isoforms was seen to increase depending on the experimental condition. Differences between conditions were statistically determined by calculating two-tailed T-tests with unequal variance for each protein and acetylation isoform, and correcting the P-values with the Benjamini-Hochberg method. Proteins and acetylsites were labeled as significantly regulated if they are different between conditions at $q \leq 0.05$, i.e. a 5%

false-detection rate (FDR). Raw mass spectrometry data and search results are available on MassIVE (ID: MSV000082951, PW: mildcoldstress).

2.5.3 Metabolite profiling. Polar metabolites were analyzed at the Whitehead Institute Metabolite Profiling Core Facility. BAT samples were homogenized in four volumes of water using a TissueLyser II (Qiagen), and polar metabolites were measured using liquid chromatography coupled to tandem mass spectrometry (LC-MS/MS). A multiple reaction monitoring method was employed, where MS transitions, declustering potentials and collision energies were determined using reference standards. Metabolites were analyzed in either negative or positive ionization mode as previously described (M. K. Townsend et al. 2013).

Negative ionization mode data were acquired as follows. A 30µL aliquot of each homogenate was extracted using 120 µL of 80% methanol containing 0.05 ng/µL $^{15}N_4$-inosine-, 0.05 ng/µL $^{2}H_4$-thymine, and 0.1 ng/µL $^{2}H_4$-glycocholate as internal standards (Cambridge Isotope Laboratories). The samples were centrifuged (10 min, 9,000 x g, 4°C) and the supernatants (10 µL) were injected directly onto a 150 x 2.0 mm Luna NH2 column (Phenomenex). Separation was performed with an ACQUITY UPLC system (Waters) running a hydrophilic interaction chromatography (HILIC) method. Initial mobile phase conditions were 10% mobile phase A (20 mM ammonium acetate and 20 mM ammonium hydroxide in water and 90% mobile phase B (10 mM ammonium hydroxide in 75:25 v/v acetonitrile/methanol) and the column was eluted at 400 µL/min using a 10 min linear gradient to 100% mobile phase A. Negative-mode MS/MS data were acquired using a 5500 QTRAP triple quadrupole mass spectrometer (AB Sciex). The ion spray voltage was -4.5 kV and the source temperature was 500°C.

Positive ionization mode data were acquired as follows. A 10-µL aliquot of each homogenate was extracted using nine volumes of 74.9/24.9/0.2 (v/v/v) acetonitrile/methanol/formic acid

containing stable isotope-labeled internal standards: 0.2 ng/μL $^{2}H_{8}$-L-valine-d8 (Isotec); and 0.2 ng/μL $^{2}H_{8}$-L-phenylalanine (Cambridge Isotope Laboratories). Samples were centrifuged (10 min, 9,000 x g, 4°C) and supernatants (10 μL) were injected onto a 150 x 2.1 mm Atlantis HILIC column (Waters). Separation was performed with an 1100 Series pump (Agilent) and an HTS PAL autosampler (Leap Technologies). The column was eluted isocratically at a flow rate of 250 μL/min with 5% mobile phase A (10 mM ammonium formate and 0.1% formic acid in water) for 1 min followed by a linear gradient to 40% mobile phase B (acetonitrile with 0.1% formic acid) over 10 min. Positive ionization mode MS/MS data were acquired using a 4000 QTRAP triple quadrupole mass spectrometer (AB Sciex). The ion spray voltage was 4.5 kV and the source temperature was 450°C.

MultiQuant 1.2 software (AB Sciex) was used for automated peak integration and metabolite peaks were manually reviewed for quality of integration and compared against a known standard to confirm identity. Peak quantifications for each metabolite were normalized across all runs using the mass of the tissue sample. Differences between conditions were statistically determined by calculating two-tailed T-tests with unequal variance for each metabolite, and correcting the P-values with the Benjamini-Hochberg method. Metabolites were labeled as significantly regulated if they are different between conditions at $q \leq 0.05$, i.e. a 5% false-detection rate (FDR).

2.5.4 UCP1 mutant plasmid construction and retroviral infection. Mouse UCP1 cDNA was subcloned into the pMSCV-puro-FLAG (C-terminal tagged) (Clontech) vector. UCP1 acetylation deficient-(KR) or mimetic-(KQ) mutant constructs were generated by site-directed mutagenesis using the NEBaseChanger tool for point mutation primers design. To generate 293T cells were transfected with pMSCV-puro retroviral vectors expressing UCP1-Flag WT, UCP1-Flag 3KR, UCP1-Flag 3KQ, UCP1-Flag 4KR, UCP1-Flag 4KQ in combination with the retroviral packaging

plasmids pCMV-VSVG (Addgene) and pCMV-Gag-Pol (Addgene). The culture media supernatant were added into target cells (293T) and followed by 24h incubation with Polybrene (8 ug/mL, Sigma). After incubation, the medium was replaced with complete medium. After 48h post infection, cells were trypsinized and subjected to puromycin selection.

2.5.5 Gene expression and western blot analysis. For analyzing mRNA levels, total RNA was isolated using Qiazol (Qiagen) and RNeasy kit (Qiagen), cDNA synthesis was performed using High Capacity cDNA reverse transcription kit (#4368813, Applied Biosystems) and analyzed in a StepOnePlus real-time PCR machine. Primers for mouse UCP1 were 5'-CTGCCAGGACAGTACCCAAG and 3'-TCAGCTGTTCAAAGCACACA, and primers for TBP (a normalization control) were 5'-GAAGCTGCGGTACAATTCCAG and 3'-CCCCTTGTACCCTTCACCAAT. For western blot analysis, cells were harvested in cold PBS and lysed in lysis buffer (1% Triton X-100, 50mM Hepes at pH7.4, 150mM NaCl, 10mM beta-glycerol phosphate, 2mM EDTA, protease inhibitor cocktail). After elution by 5x sample buffer, the protein lysates were boiled followed by run (typically 10-20 ug per lane) in SDS acrylamide/bis-acrylamide gels, transferred to PVDF membranes and detected with indicated antibodies.

Chapter 3: RICTOR Loss Induces an Interferon-Like Response and Unevenly Suppresses Insulin-Dependent Phosphorylation in Brown Adipocytes

Samuel W. Entwisle[1,2], Camila Martinez-Calejman[3], Anthony Valente[2], David A. Guertin[3,4,5], Judit Villén[1,2,*]

[1]Molecular and Cellular Biology Program, University of Washington, Seattle, WA 98195

[2]Department of Genome Sciences, University of Washington, Seattle, WA 98195

[3]Program in Molecular Medicine, University of Massachusetts Medical School, Worcester, MA 01605

[4]Department of Molecular, Cell and Cancer Biology, University of Massachusetts Medical School, Worcester, MA 01605

[5]Li Weibo Institute for Rare Diseases Research, University of Massachusetts Medical School, Worcester, MA 01605

*Corresponding author: Judit Villen (jvillen@uw.edu)

3.1 Summary

Stimulating brown adipose tissue (BAT) activity represents a promising therapy for overcoming metabolic diseases. Understanding metabolic control in BAT by cellular signaling pathways will be critical for developing novel therapies that stimulate BAT activity. mTOR complex 2 (mTORC2) regulates AKT activity, which is a key kinase of the insulin signaling pathway. mTORC2 has been shown to be important for regulating BAT metabolism, yet its mechanism of activation is not known, nor are the identities of its downstream effectors. In this study, we apply proteomics to investigate the role of mTORC2 in brown adipocytes. To assess the role of mTORC2 in brown adipocytes, we compare wild-type controls to isogenic cells with an induced knockout of the mTORC2-specific subunit RICTOR (*Rictor*-iKO) by stimulating each with insulin for a 30 minute time course, and measuring the proteomes and phosphoproteomes. In *Rictor*-iKO cells, we identify decreases to proteasome core subunits, and increases to antigen-presentation and STAT1, suggesting de-repression of interferon-like signaling. From analyzing the phosphoproteome, we observe significant differences to basal phosphorylation including decreased phosphorylation of the lipid droplet protein perilipin-1 phosphorylation in *Rictor*-iKO cells, suggesting that RICTOR could be involved with regulating basal lipolysis. And finally, we observe a suppressed magnitude of the insulin signaling response in *Rictor*-iKO cells. Some sites exhibit significant dependence on RICTOR, including an AKT substrate site on ATP citrate lyase, which could partially explain the previously-observed RICTOR dependence of *de novo* lipogenesis from glucose in BAT. These results reveal new roles for RICTOR and mTORC2 including suppression of an interferon-like response, and control of the overall magnitude and specificity of insulin-dependent phosphorylation.

3.2 Introduction

The mammalian target of rapamycin (mTOR) is a serine/threonine kinase and a ubiquitous and critical regulator of metabolism and cell growth. mTOR exists in two protein complexes. mTOR complex 1 (mTORC1) is activated by intracellular amino acid levels, and by the kinase AKT in response to stimulation by insulin and other growth factors. mTOR complex 2 (mTORC2) is less well understood, though it is essential for embryonic development and the proper functioning of many tissues in mammals (Guertin et al. 2006; Yuan et al. 2012; Kumar et al. 2010). Despite its importance, its mechanism of activation and the full extent of its downstream effectors have been difficult to elucidate.

mTORC2 plays an important role in BAT, as has been shown by two different tissue-specific knockouts of the mTORC2-specific subunit RICTOR. Each knockout had different tissue specificities that each contained BAT, and each caused a different phenotype in BAT; one caused impaired glucose uptake and thermogenesis (Albert et al. 2016), while the other improved BAT thermogenesis (Hung et al. 2014). *In vitro* cell culture models of *Rictor-iKO* showed that RICTOR is required for brown adipocyte differentiation (Hung et al. 2014) and βA-driven glucose uptake (Olsen et al. 2014). These studies reveal the complexity and context-specificity of mTORC2-mediated metabolic regulation alongside its potential utility as a therapeutic target, and underscore the need for a more complete picture of mTORC2 and its role in cellular signaling.

mTORC2 is activated downstream of growth factor signaling, including insulin/IGF-1, and its signaling role is largely understood in terms of its most well-characterized substrate, AKT. When activated, mTORC2 phosphorylates the C-terminal, hydrophobic motif of AKT (S473 in AKT1, S474 in AKT2). Mutagenesis studies have shown that maximal *in vitro* AKT activity is

dependent on phosphorylation of its hydrophobic motif (Risso et al. 2015). However, *in vivo* results show a more complicated picture, as several AKT substrates appear unaffected by mTORC2 loss in BAT (Hung et al. 2014). mTORC2 has also been shown to act in a positive feedback loop with AKT (Yang et al. 2015), but the effect of this feedback mechanism on broad downstream signaling has not been demonstrated. Investigating the signaling role of mTORC2 could provide insight to metabolic regulation in BAT, as well as in other tissues.

Several different studies have compared the transcriptome, proteome, or metabolome of cells with and without functional mTORC2 (Oh et al. 2017); (Wang et al. 2018); (Shimobayashi et al. 2018); (Kleinert et al. 2016). In addition, Lamming et al. used phosphoproteomics alongside transcriptomics to identify potential novel downstream effectors of mTORC2 in the mouse liver. However, they only measured samples after feeding, and thus could not assess the dynamic response to feeding of mTORC2-dependent signaling (Lamming et al. 2014). To date, no study has assessed the function of mTORC2, *vis-a-vis* its downstream phosphorylation targets, in the context of dynamic signal transduction. Here, we use mass spectrometry-based phosphoproteomics to profile phosphorylation changes that occur in wild-type or *Rictor*-iKO cultured brown adipocytes after being stimulated by insulin for a 30 minute time series. Using both discovery-driven and hypothesis-driven approaches, we find that RICTOR loss lowers the expression of insulin-related metabolic proteins, increases expression of immune-response proteins, and promotes dampening of AKT substrate phosphorylation in response to insulin that is most strongly seen in a set of AKT substrates that includes the DNL enzyme ATP citrate lyase.

3.3 Results

3.3.1 Time course analysis of RICTOR-*dependent insulin signaling in brown adipocytes.* In order to assess the function of mTORC2 in differentiated brown adipocytes, it was necessary to develop a model whereby mTORC2 can be knocked out in mature adipocytes. As was reported previously, *Rictor-iKO* prevents *in vitro* differentiation of brown adipocytes (Hung et al. 2014). In order to circumvent this, *Rictor-iKO* was engineered by a tamoxifen-inducible CreER-Lox recombinase system (*Rictor*-iKO). Preadipocytes possessing *Rictor*-iKO were differentiated to mature brown adipocytes, and subsequently treated with 4-hydroxytamoxifen (*Rictor*-iKO) or vehicle (control) to induce knockout. The cells were then left for 6 days to ensure complete degradation of RICTOR protein.

mTORC2 is well understood to be a part of the insulin signaling pathway, as it is important for insulin-induced phosphorylation of the AKT hydrophobic motif. Phosphorylation downstream of insulin stimulation has been shown to be highly dynamic, with some phosphorylation events responding rapidly and some responding at 5-10 minutes (Humphrey et al. 2013). Thus, to probe the signaling role of mTORC2, we chose to perform an insulin time-course analysis. Cells were starved overnight in serum-free media, and treated with 150 nM insulin for a 30 minute time series (Fig 3.1A). Cells were snap-frozen at 0 (i.e. unstimulated), 1, 2, 5, 10, 15, and 30 minutes. *In vitro* differentiation was performed in two batches, and three replicates were harvested per time point per batch. This time course scheme will provide a dynamic view of phosphorylation-based cellular signaling. It will also allow a highly powered proteome comparison of *Rictor*-iKO and control brown adipocytes, given that the proteome will be unlikely to change much over a 30 minutes of insulin stimulation, but it is likely to be different between control and *Rictor*-iKO cells. We posited that differences between control and *Rictor*-iKO cells

might underlie differences in dynamic signaling in response to insulin. Thus, we analyzed the proteome and phosphoproteome in the same cells and stimulation conditions.

3.3.2 Proteome analysis reveals changes to diverse cellular processes in Rictor-*iKO brown adipocytes.* Proteome analysis was performed by analyzing each sample in a single run on a QExactive (Thermo) mass spectrometer. Each run identified over 3,000 proteins with a ProteinProphet probability of greater than 0.95 (Fig 3.1B). To assess statistically significant changes as a result of RICTOR loss, insulin stimulation, or an interaction between the two, we employed analysis of variance (ANOVA) followed by a Benjamini-Hochberg correction. We found no statistically significant protein abundance changes as result of insulin stimulation, nor did we find any protein abundances whose response to insulin depended on the presence of RICTOR (Fig 3.1C). This is because protein expression changes require more time than the 30 minutes of insulin stimulation spanned by our time series analysis. However, we found 1,284 proteins with significant differences in expression between control and *Rictor*-iKO cells (Fig 3.1C). This suggests that broad proteome reprogramming occurs in brown adipocytes that lose RICTOR.

To further explore the proteome changes that occur upon RICTOR loss, we performed gene ontology (GO) enrichment analysis to identify molecular functions, biological processes, and cellular compartments that are overrepresented among increasing and decreasing proteins after *Rictor-iKO*. This revealed that glycolytic enzymes are overrepresented among proteins that are decreased in abundance by *Rictor-iKO* (Figs 3.1D, 3.1G). This is consistent with previous studies reporting that mTORC2 induces glycolysis in brown adipocytes by increasing cytosolic hexokinase activity (Albert et al. 2016), and with work in cancer cells demonstrating that mTORC2 regulates glycolytic gene expression in glioblastoma cells (Masui et al. 2013). In our

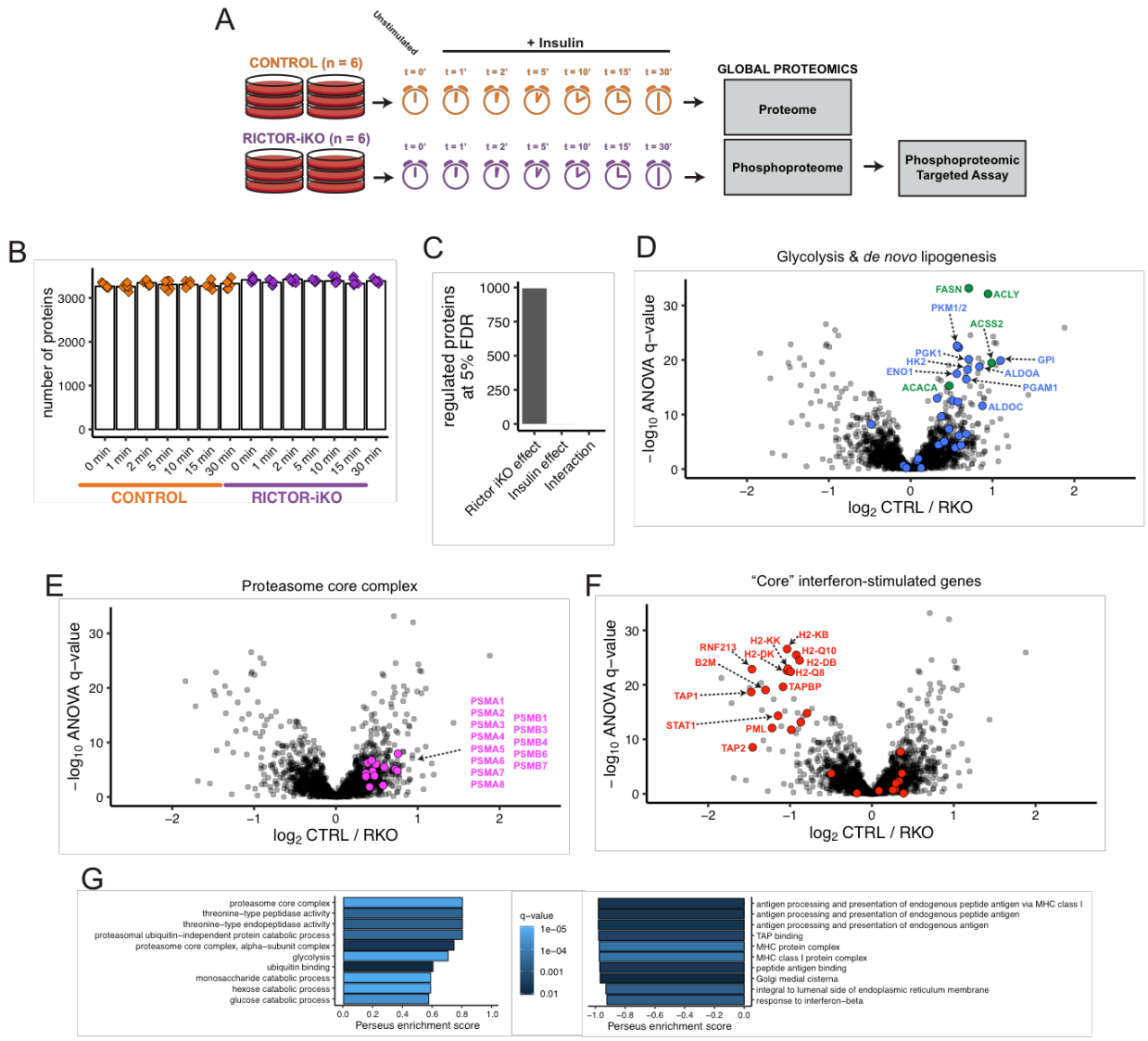

Figure 3.1 *Rictor-iKO* downregulates the proteasome, upregulates interferon-like response. (A) Experimental design **(B)** Number of identified proteins per replicate, organized by condition. **(C)** Number of proteins that are affected by *Rictor*-iKO, insulin stimulation, or an interaction between the two (ANOVA, 5% FDR). **(D)** Volcano plot with glycolysis and *de novo* lipogenesis enzymes highlighted. **(E)** Volcano plot with core proteasomal subunits highlighted. **(F)** Volcano plot with core interferon-stimulated genes, as identified by Shaw et al. (Shaw et al. 2017). **(G)** GO enrichment analysis for proteins that are downregulated (left) or upregulated (right) in *Rictor*-iKO cells.

brown adipocyte cell culture model, glycolytic enzyme expression is increased at almost every step. mTORC2 has also previously been shown to regulate expression of DNL enzymes. Indeed, we observe that fatty acid synthase (FASN) and ATP citrate lyase (ACLY), acetyl-CoA synthetase 2 (ACSS2), and acetyl-CoA carboxlyase A (ACACA) are among the proteins most significantly downregulated by *Rictor-iKO*. GO enrichment analysis also revealed that terms related to the proteasome are higher in the presence of RICTOR (Figs 3.1E, 3.1G). Specifically, expression of the alpha subunits 1-8 and beta subunits 1-7 are decreased by *Rictor-iKO*. In addition the molecular function term “ubiquitin binding” is enriched among proteins that are decreased by *Rictor-iKO*, including the protein Ubiquilin-1, which is important for targeting polyubiquitinated proteins to the proteasome (not shown). Other proteins involved with quality control are downregulated in *Rictor-iKO* cells, including NPLOC4 and VCP, which are two members of the VCP-UFD1-NPL4 complex that detects ubiquitinated proteins in the ER and sends them to the cytosol for degradation. Interestingly, the deubiquitinase UCHL3 is significantly decreased after mTORC2 loss. While its increase would appear to function in opposition to increases in the ubiquitin proteasome system, it has been shown previously to support maximal insulin signaling, through an indirect mechanism, as measured by phosphorylation of the insulin receptor, AKT, and FOXO1 (Suzuki et al. 2009). Thus, in brown adipocytes, RICTOR enables maximal expression of many components of the ubiquitin proteasome system.

RICTOR loss also significantly increases the expression of some proteins. Most strikingly, several proteins related to antigen presentation are upregulated in *Rictor-iKO* cells, and several related GO terms are highly enriched (Fig 3.1F, 3.1G). Specific proteins include six type I major histocompatibility antigens, beta-2 microglobulin, the antigen peptide transporters TAP1/2, and tapasin (Fig 3.1F). Increases to these proteins are consistent with a general increase in

interferon signaling. In concordance, the signal transducer STAT1 is also increased in *Rictor*-iKO cells, which is consistent with a greater ability to respond to type-I interferons. To test the hypothesis that interferon response proteins are increased in *Rictor*-iKO cells in general, I cross-referenced a recent list of "core" interferon-stimulated genes that was identified by assessing the evolutionary conservation of interferon responses (Shaw et al. 2017). Of these proteins that were identified in our study, a majority strongly and significantly increase as a result of RICTOR loss (Fig 3.1F). This raises an intriguing possibility that RICTOR/mTORC2 represses interferon signaling. Taken together, our proteome analysis reveals that RICTOR is upstream of diverse cellular processes, including glucose metabolism, proteostatic mechanisms and interferon-associated antigen presentation.

3.3.2 Rictor-*iKO affects phosphorylation of perilipin-1 and the caveolar proteins caveolin-2 and caveolae-associated protein 2 in an insulin-independent manner.* Understanding the signaling role of RICTOR within mTORC2 will be important for explaining the protein expression and phenotypic changes resulting from RICTOR loss. To address this, we analyzed the insulin time course and assessed similarities and differences in phosphorylation levels. To analyze phosphorylation in the time series proteomics samples, digested peptides were enriched using iron(III) immobilized metal ion affinity chromatography. The enriched phosphopeptide samples were then subjected to single shot analysis on an Orbitrap Fusion Tribrid (Thermo). From this analysis, we identified over 5,000 phosphorylation sites per replicate (Fig 3.2A).

Principal component analysis (PCA) was performed to identify global similarity between all the samples, and it showed that the control and *Rictor*-iKO cells are easily distinguished by their phosphorylation profiles along principal component 1, while the time of insulin stimulation separated the samples along principal component 2 (Fig 3.2B). In sum, and not surprisingly,

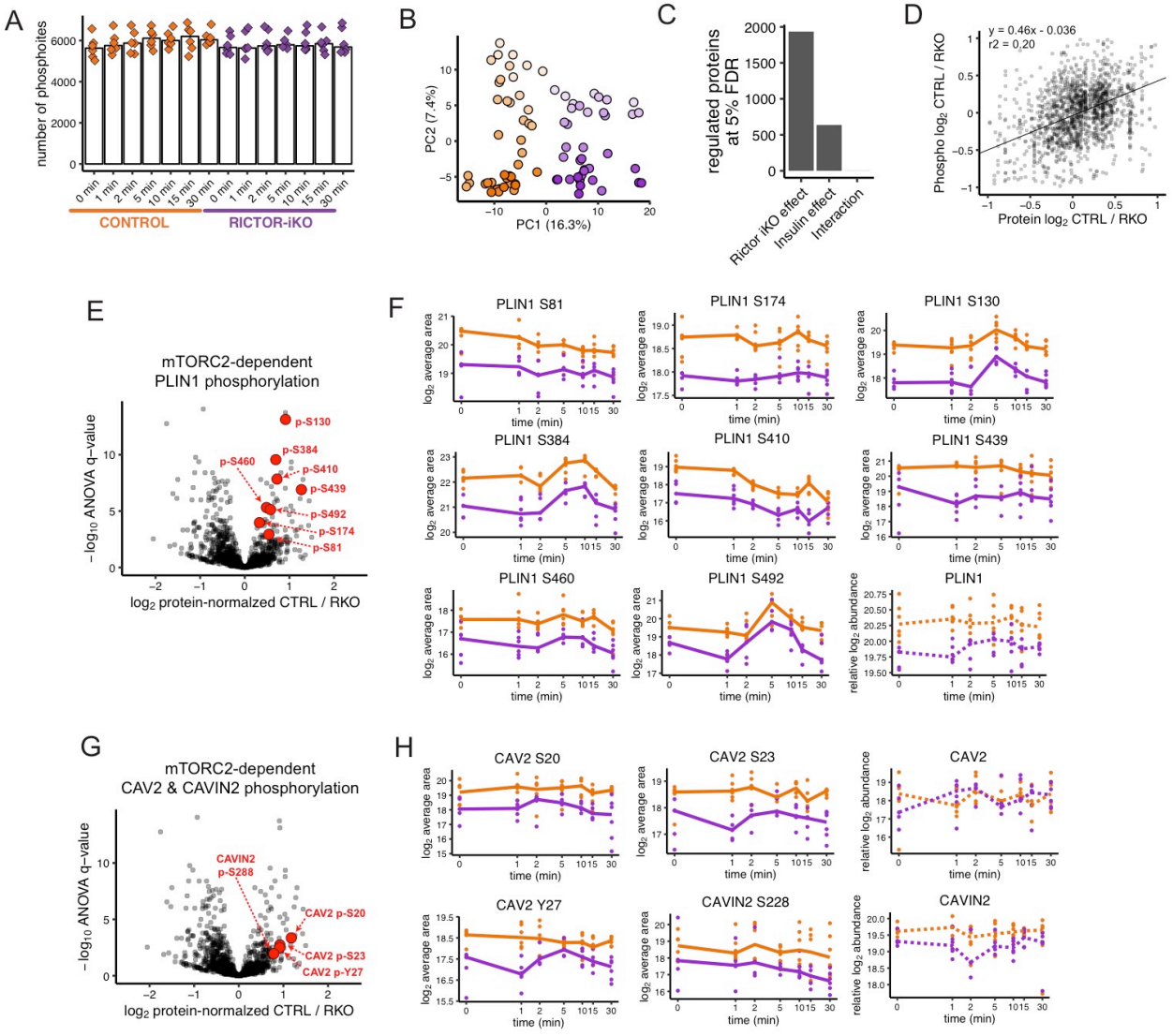

Figure 3.2 RICTOR controls basal phosphorylation independent of insulin, including on perilipin-1 and caveolar proteins. (A) Number of identified phosphosites per replicate, organized by condition. **(B)** Principal component analysis of phosphorylation site quantitative measurements. Darker shades represent later time points; orange is control, and purple is *Rictor*-iKO. **(C)** Number of phosphosites that are affected by *Rictor*-iKO, insulin stimulation, or an interaction between the two (ANOVA, 5% FDR). **(D)** Scatter plot of relative abundance changes between controls and *Rictor*-iKO for phosphosites versus their respective proteins. **(E-F)** Volcano plot **(E)** highlighting protein-normalized perilipin-1 (PLIN1) phosphorylation sites alongside phosphorylation- and protein-level quantifications **(F)** for every condition. **(G-H)** Volcano plot **(G)** highlighting caveolin-2 (CAV2) and caveolae-associated protein (CAVIN2) phosphorylation sites alongside phosphorylation- and protein-level quantifications **(H)** for every condition.

PCA revealed that both RICTOR loss and insulin stimulation had a strong effect on phosphorylation. We hypothesized that phosphorylation differences could manifest in one of two ways: they could be due to differences in basal phosphorylation independent of insulin, or they could be due to differences in the insulin response. First we sought to characterize the differences in basal phosphorylation between control and *Rictor*-iKO brown adipocytes. As with the proteomics data in section 3.2.2, we calculated ANOVA statistics to assess the relative contribution of insulin and *Rictor*-iKO on global phosphorylation. This revealed that nearly 2,000 sites had significantly different phosphorylation levels in *Rictor*-iKO cells relative to controls (Fig 3.2C). Based on this, we sought to understand whether phosphorylation differences between control and *Rictor*-iKO cells are due to protein abundance changes, or to changes in basal phosphorylation occupancy. Plotting the fold-change in abundance between control and *Rictor*-iKO for phosphorylation versus their respective proteins, for all cases where the comparison was possible, revealed a relatively poor correlation between the two (Fig 3.2D). Thus, we expect that many differences in basal phosphorylation between control and *Rictor*-iKO cells are due to phosphorylation sites occupancy, rather than protein abundance.

We next sought to identify phosphorylation sites with significantly higher occupancy in control or *Rictor*-iKO cells. To accomplish this, all quantified phosphorylation sites were normalized to the quantification of abundance for that protein in each replicate. If an abundance measurement for that protein was not available, the phosphosite quantification was dropped for that replicate. This approach revealed many sites with significant differences relative to their respective proteins. Among these were several sites on the protein perilipin-1 (PLIN1) (Fig 3.2E, 3.2F). PLIN1 coats lipid droplets, and regulates lipolysis, and its phosphorylation has been associated with lipolysis (Marcinkiewicz et al. 2006). Several sites on PLIN1 are hypophosphorylated in *Rictor*-iKO cells, perhaps indicating decreased lipolysis. Two of these sites on PLIN1, S81-p and

S492-p, are reported protein kinase A (PKA) substrates, suggesting the intriguing hypothesis that RICTOR could also regulate basal PKA-mediated lipolysis in response to β-adrenergic stimulation.

Two other examples of proteins that have several sites that similarly decrease in *Rictor-iKO* are Caveolin-2 (CAV2) and Caveolae-associated protein 2 (CAVIN2) (Fig 3.2G, 3.2H). Both proteins are components of caveolae, which are invaginations of the plasma membrane that are abundant in adipocytes and important for lipid trafficking and metabolism (Pilch & L. Liu 2011). Whether mTORC2 regulates caveolae and/or lipolysis via insulin-independent phosphorylation are potentially interesting areas for future investigation.

3.3.4 Insulin signaling is mildly but broadly diminished by mTORC2 loss. We next sought to assess the role of mTORC2 in insulin signaling. From our ANOVA analysis of global phosphorylation described above, we found that over 500 phosphosites had a significant response to insulin. However, this statistic simultaneously considers the control and *Rictor*-iKO conditions. To test for an interaction between the effects of insulin and RICTOR loss, we performed a 2-way ANOVA, which revealed only two sites that had a significantly different insulin response in the control and *Rictor*-iKO: S542 on the ubiquitin ligase AMFR and S2223 on the nuclear pore protein TPR (Fig 3.3A). While S2223 on TPR has not been functionally characterized before, AMFR is a member of the VCP/p97-AMFR/gp78 E3 ubiquitin ligase complex, and phosphorylation of S542 on AMFR by p38 has been shown to regulate mitochondrial-endoplasmic reticulum interactions and mitochondrial motility (L. Li et al. 2015). In sum, ANOVA reveals phosphorylation sites that significantly change due to insulin stimulation, and two sites that have statistically significant responses.

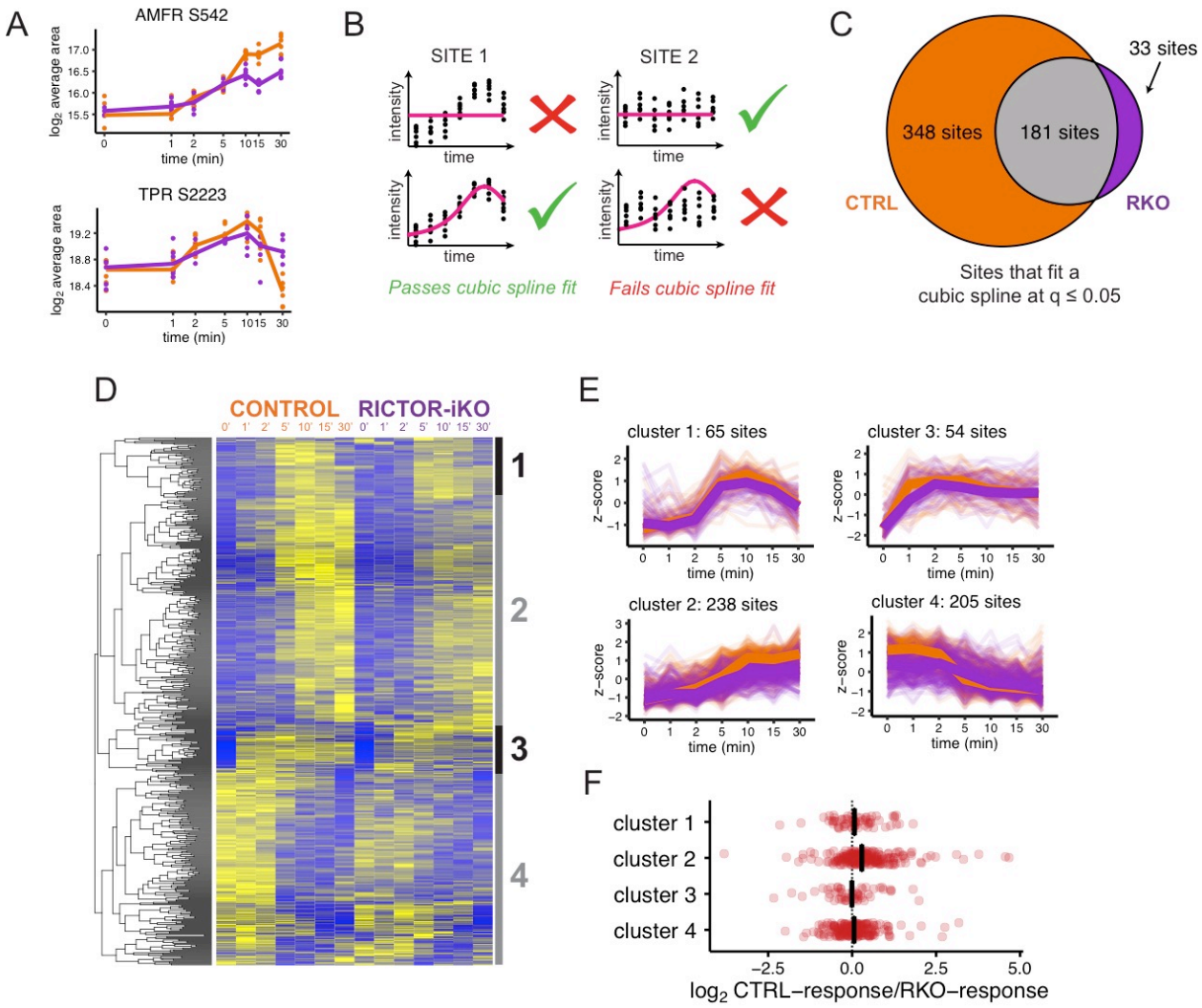

Figure 3.3 RICTOR loss causes a mild loss in insulin phospho-signaling sensitivity that is balanced towards later-increasing phosphorylation sites. (A) Plots showing *Rictor*-dependent insulin responses as determined by 2-way ANOVA analysis with a 5% FDR cut-off. **(B)** Schematic overview of cubic spline fitting method to assess insulin responsiveness in individual time series. **(C)** Euler diagram showing the number of phosphosites from the control and *Rictor*-iKO time series that successfully fit a cubic spline model at 5% FDR. **(D)** Heatmap and hierarchical clustering of phosphosites that fit a cubic spline model in either the control or *Rictor*-iKO. Four clusters are defined that represent the range of temporal responses. **(E)** Line plots of clusters in (D). **(E)** The dynamic range of the control and *Rictor*-iKO insulin responses were compared by calculating a ratio between the two, which was plotted to show the relative average RICTOR dependence for each cluster from (D).

While the 2-way ANOVA represents a stringent test of potential differential insulin sensitivity of individual sites, we sought to get a sense for more global trends. To assess insulin responsiveness in control and *Rictor*-iKO cells separately, we applied an implementation of a cubic spline model that was developed to analyze DNA microarray time series data (Storey et al. 2005). The method tries to fit a cubic spline function to the data and assesses its goodness-of-fit relative to a horizontal line (Fig 3.3B). Using this approach, we identified 528 phosphosites that significantly change in response to insulin in control cells, and only 214 that significantly change in the *Rictor*-iKO cells (Fig 3.3C). To reveal patterns of insulin responsiveness, we performed hierarchical clustering on the phosphorylation sites normalized to the minimum condition in each time course (often t=0). This analysis revealed four cluster of sites: one that peaks at around 5 minutes and then drops down again by 30 minutes (cluster 1), one that peaks at around 30 minutes (cluster 2), one that achieves near-maximum response after only one minute of insulin stimulation (cluster 3), and one that drops through the entire time course (cluster 4) (Fig 3.3D-3.3E). To quantify whether *Rictor*-iKO affects the insulin response in some clusters more than others, time course dynamic range was compared between control and *Rictor*-iKO cells by calculating a maximum/minimum ratio for the control and *Rictor*-iKO time series. When this response ratio was plotted for each site and averaged across clusters, it revealed that the insulin response of cluster 2 is more greatly diminished by RICTOR loss than the other clusters on average (Fig 3.3F). This suggests that RICTOR has a slight preference to control later-phosphorylated insulin-responsive phosphorylation sites relative to rapidly-phosphorylated or dephosphorylated sites.

3.3.5 Targeted analysis of a panel of phosphorylation sites with known functions related to AKT, AGC kinases, and fundamental cell signaling processes. A known limitation of data-dependent acquisition (DDA) proteomics is the stochastic sampling of peptide precursors to fragment and

sequence, which leads to missing values and a bias towards more abundant peptides. This means that important peptides, e.g. hydrophobic sites on AKT, and some AKT substrates, were not measured in all of our experimental conditions. To circumvent this limitation, we employed targeted mass spectrometry, where peptides of interest are chosen *a priori* and measured systematically based on predicted mass-to-charge ratios and chromatographic retention times. A recent study in our laboratory showed that data from pooled, un-targeted DDA experiments can be used to predict the behavior of peptides and target them using parallel reaction monitoring (PRM) (Lawrence et al. 2016). Thus, to complement our discovery-driven, DDA experiment from sections 3.3.3 and 3.3.4, we composed a list of literature-curated phosphorylation sites comprising known AKT substrates, regulatory phosphorylation sites on AGC kinases, and other fundamental cell signaling and BAT-associated phosphorylation sites that have been previously observed in mouse phosphoproteome experiments in our laboratory. This initial list consisted of nearly 400 phosphopeptides. To narrow down the list into 100-200 that can fit in a single one-hour PRM method, the 400 peptides were split up into separate targeted methods and measured with wide retention time windows in a pooled brown adipocyte phosphopeptide sample. This allowed us to prioritize peptides that are abundant in our brown adipocyte sample, and ensure that only one peptide per site, or combination of sites, was included in the final assay. In the end, 97 phosphopeptides were quantified well across our time series (see Fig 3.4A), and an additional 12 were used for normalization, as they did not change across our time series conditions as shown by our DDA data. Importantly, the targeted analysis allowed us to measure many phosphorylation sites that were absent or incompletely measured in the global phosphoproteomic analysis of the same samples described above (Fig 3.4B).

Hierarchical clustering of the targeted phosphorylation sites (Fig 3.4C) revealed clusters of sites comparable to the clusters seen from the global phosphoproteomics in Fig 3.3D. It also showed

that most of the insulin-sensitive sites in the target list increased over the course of the time series (Fig 3.4C). As above, 2-way ANOVA analysis was used to identify phosphopeptides that show a significantly different insulin response in the control versus *Rictor*-iKO. This revealed several phosphorylation sites with significantly different responses (Fig 3.4D). The targeted approach was likely more highly powered because several sites were not measured well in the DDA experiment, and because the total number of measurements is much lower so that the Benjamini-Hochberg multiple test correction is not as harsh. As anticipated, the insulin response of AKT2 hydrophobic motif phosphorylation (S474) is greatly diminished in the *Rictor*-iKO (Figs 3.4D, 3.4E). Two other sites with previously-observed association to mTORC2 activity were also significantly decreased in the *Rictor*-iKO cells: mTOR S2481 and NDRG1 S330 (Figs 3.4D, 3.4E). Thus, some of the most significantly altered insulin-sensitive phosphorylation sites confirm prior knowledge about mTORC2-dependent phosphorylation.

Our ANOVA analysis additionally revealed novel examples of phosphorylation sites with *Rictor*-dependent insulin responses. These include the AKT substrate site on ACLY (Fig 3.4F), which is also decreased at the protein level by RICTOR loss (Fig 3.1D). In addition, an AKT substrate site on AS160 has a *Rictor*-dependent insulin response, suggesting an effect on insulin-dependent glucose uptake (Fig 3.4F). The insulin response of two translation-related phosphorylation sites are also diminished by RICTOR loss: S422 on the translation initiation factor EIF4B, and S64 and T69 on EIF4EBP1 (Fig 3.4F). The phosphorylation sites on EIF4B and EIF4EBP1 are associated with increased translation (Gingras et al. 2001; Shahbazian et al. 2006). Taken together, targeted phosphoproteomics analysis confirms that mTORC2 loss decreases the insulin-sensitivity of brown adipocytes, while providing more statistical power to identify some AKT substrate sites, such as ACLY, AS160, and translation-associated proteins, that are more impacted than others.

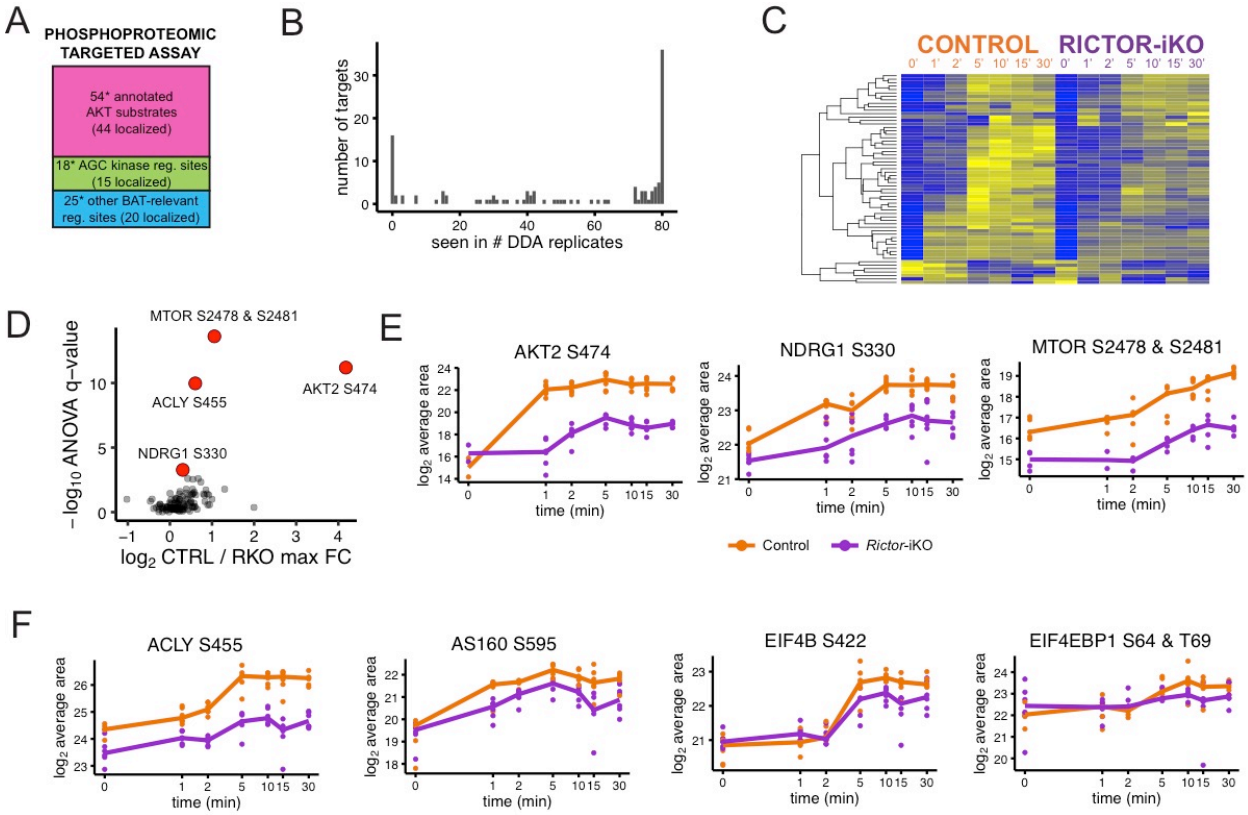

Figure 3.4 Targeted analysis reveals ACLY, AS160, and two translation-associated proteins to be part of a RICTOR-dependent insulin response. **(A)** Schematic outline of the phosphoproteomic targeted assay. **(B)** Histogram showing the number of replicates that phosphorylation targets were seen in the DDA experiment. **(C)** Heatmap showing hierarchical clustering of phosphorylation targets. **(D)** Volcano plot of all measurements from targeted phosphoproteomics assay, showing the ratio of insulin response magnitude on the x-axis. **(E)** Phosphorylation sites with previously known dependence on mTORC2. **(F)** AKT substrate sites on ACLY, AS160, and EIF4B, and an mTORC1 substrate site on EIF4EBP1.

3.4 Discussion

Despite its clear importance in regulating glucose and lipid metabolism, mTORC2 remains the most poorly understood mTOR complex both in terms of its upstream regulation and its downstream effectors. Different studies have found that mTORC2 can localize to diverse areas of the cell depending on the cell type and contexts (Zinzalla et al. 2011) (Betz et al. 2013) (Ebner et al. 2017). This context specificity is underscored by the fact that *Rictor-iKO* in *Myf5*+ tissues (BAT and skeletal muscle) affects BAT function very differently than does *Rictor-iKO* in *aP2*+ tissues (BAT and white adipose tissue). mTORC2 is known to act as an AKT kinase, yet there have been conflicting reports about the nature of its regulation of AKT activity. Several groups have observed that some AKT substrates are sensitive to mTORC2 loss while others are not. However, the identity of mTORC2-dependent AKT substrates has not been explored in a systematic way.

We compared insulin-dependent and insulin-independent effects of mTORC2 loss on downstream phosphorylation. Our results show that, independently of insulin, *Rictor*-iKO de-represses an immune response in brown adipocytes, and changes the basal phosphorylation levels of several sites including perilipin-1 and caveolae-related proteins. In addition, mTORC2 loss decreases the overall insulin sensitivity of AKT substrates, some more so than others, while largely preserving the dynamics of AKT substrate phosphorylation.

The main hypothesis we sought to test was whether mTORC2 loss affects the insulin response as reflected in protein phosphorylation levels. We first assessed this using global phosphoproteomics. While this approach did not have sufficient statistical power to detect differential insulin responses using an ANOVA approach, it did show a clear, if mild, repression of the magnitude of insulin responses, and allowed us to identify two candidate *Rictor*-

dependent, insulin-sensitive phosphorylation sites in AMFR S542 and TPR S2223. Targeted phosphoproteome analysis allowed us to further explore this loss of insulin sensitivity, as it afforded us increased sensitivity to measure low abundance phosphorylation events, and it reduced the burden of multiple hypothesis testing compared to a global analysis. Through this targeted approach, we identified annotated AKT substrate sites on ACLY, AS160, and EIF4B,, among others, whose insulin sensitivity was partially dependent on *Rictor*. In particular, the S455 site on ACLY is of interest as it has been previously shown to promote activity of ACLY (Potapova et al. 2000), and to be an AKT substrate in adipocytes (Berwick et al. 2002). ACLY activity is important for DNL; thus, this could be a mechanism, in addition to inducing expression of DNL enzymes, whereby mTORC2 could promote DNL. The mechanisms that determine mTORC2-dependent ACLY phosphorylation, and mTORC2-dependent AKT substrate preference in general, should be investigated further.

While some AKT substrates show a greater dependence on mTORC2 for maximum insulin response another notable consequence of mTORC2 knockout is a broad dampening of insulin signaling. This effect was observed in the targeted, and also in the global phosphoproteome analysis, and appears more prominent in the later-activating phosphorylation sites (see Fig 3.3F). However, it should be noted that the 2-way ANOVA statistic biases against detection of significantly different early-activating phosphorylation sites, as there are no time points between 0 and 1 minute to add confidence. Thus, while we are unable to determine with statistical rigor the extent to which mTORC2 specifically promotes late versus early insulin-sensitive phosphorylation, mTORC2 does appear to have a slight preference towards the latter. Future work will need to explore this question with more depth by assessing *Rictor*-dependent phosphorylation at more time points.

How might mTORC2 suppress insulin signaling? Previous work showed that mTORC2 and AKT can act as part of a positive feedback loop that is driven by AKT-dependent phosphorylation of the mTORC2 subunit SIN1 at T86. Unfortunately, we were not able to measure this site with our phosphoproteomics approach, nor did we obtain good measurement of SIN1 protein levels. However, loss of a positive feedback loop could conceivably lead to a global repression of signaling. Another possibility lies with the finding from our proteomics work that expression of the deubiquitinase UCHL3 is dependent on mTORC2. While the mechanism for UCHL3-mediated insulin signaling suppression is not clear, yet it may involve blocking the trafficking or degradation of signaling components as its effect on insulin signaling is dependent on its de-ubiquitinase activity. A third possibility is that RICTOR directs phosphorylation of specific AKT substrates and other insulin-dependent phosphorylation events by ensuring specific subcellular co-localization of signaling components. Indeed, RICTOR has been shown to exist in several different subcellular compartments (Ebner et al. 2017). In sum, whether SIN1-mediated positive feedback, UCHL3 downregulation, subcellular localization, or some other mechanism determines mTORC2-dependent regulation of insulin signaling should be investigated further.

We have demonstrated that RICTOR loss affects global protein phosphorylation, but it also affects downstream protein expression. From our parallel time course analysis we were able to compare control and *Rictor*-iKO cells with a high number of replicates, giving high power to detect many significant changes. We identified several core proteasomal components that are downregulated by RICTOR loss. Interestingly, mTORC2 has been shown to transcriptionally induce the expression of proteasome subunits in a mechanism that appears to depend on SREBP (Zhang et al. 2014). Indeed, we observe downregulation of other proteins whose expression is regulated by SREBP, particularly the DNL-related enzymes FASN, ACACA, and ACSS2 (Horton et al. 2002). Loss of SREBP-dependent gene expression is consistent with

global dampening of insulin signaling that we observe in the phosphoproteomics dataset. The significance of mTORC2-dependent proteasome subunit expression in the context of the well-characterized metabolic phenotypes of *Rictor-iKO* BAT will need to be investigated further.

Another striking finding from our proteome analysis is the apparently coordinated upregulation of antigen presentation proteins and interferon-like signaling in *Rictor*-iKO cells. This includes several MHC class I antigens, as well as TAP1/2, and the transcriptional regulator STAT1. Interestingly, STAT1 has been shown to inhibit white adipose tissue browning through a mechanism that is dependent on an interferon response (Moisan et al. 2015). Interestingly, interferon-gamma signaling has been shown to promote insulin resistance in various tissue and cell models (McGillicuddy et al. 2009; Šestan et al. 2018; Grzelkowska-Kowalczyk & Wieteska-Skrzeczyńska 2009). This is consistent with our results, to the extent that we observe a dampened insulin signaling response in *Rictor*-iKO cells. Interferon responses have been studied in brown adipocytes, and it has been shown that interferon signaling leads to mitochondrial dysfunction and decreased expression of UCP1 (Kissig et al. 2017). The BAT-associated transcription factor PRDM16 suppressed this interferon response, suggesting that suppression of interferon response is an important part of the BAT transcriptional program. We don't see changes to overall mitochondrial protein abundance, suggesting that mTORC2 loss could somehow exert a protective effect on mitochondrial function that would counteract an increase in interferon signaling. The mechanisms underlying mTORC2-mediated regulation of this interferon-like response will need to be elucidated in future studies.

The data presented above show broad changes to protein levels and phosphorylation levels that go well beyond insulin signaling. While it is likely that basal, insulin-independent mTORC2 activity in brown adipocytes is generating many of the differences between control and *Rictor*-iKO cells, it is also worth considering potential mTORC2-independent roles for the RICTOR

protein. In adipocytes, RICTOR has been shown to interact with the unconventional myosin-Id (MYO1D) and promote cortical actin rearrangement independent of mTORC2 (Hagan et al. 2008). Another study showed that RICTOR interacts with the Cullin-1 E3 ligase and mediates ubiquitination of the kinase SGK1 (Gao et al. 2010). When analyzing *Rictor-iKO* models moving forward, it will be important to consider the effect of functions not related to mTORC2 activity.

To conclude, this work offers the most in-depth exploration yet of the role of mTORC2 in the context of dynamic cell signaling. Our analysis revealed insulin-dependent phosphorylation-based signaling events are dampened in cells without functional mTORC2, including particularly prominent dampening of insulin-responsive phosphorylation on ACLY, EIF4B and EIF4EBP1. RICTOR loss also alters insulin-independent phosphorylation, including sites on perilipin-1 and caveolar proteins that may have relevance in brown adipocytes. Finally, protein-level changes, including a strong interferon-like response in the *Rictor*-iKO cells, suggest novel regulatory functions for RICTOR and mTORC2. In sum, our analysis uncovers diverse insulin-dependent and insulin-independent roles for RICTOR/mTORC2 in brown adipocytes, shedding more light on its multi-faceted regulation of cellular metabolism.

3.5 Materials and Methods

3.5.1 Brown adipocyte cell culture. To obtain inducible-knockout cell lines, the interscapular BAT was removed from *Ubc-Cre*^{ERT2};*Rictor*^{floxed} mice at post natal day 1, dissected and minced, and added 500ul of collagenase solution. The tubes were vortexted for 10 seconds and placed into a thermomixer at 800 rpm at 37ºC for 40 min with a mechanical disaggregation at 20 min. Afterwards the digested tissue was filtered through a 100 µm filter into fresh microcentrifuge tube, and centrifuged at room temperature at 1500 rpm for 5 min. The supernatant was removed, and the pellet re-suspended in culture medium and transferred into a 6 well plate. The

cells were left overnight, and given fresh medium the next day. On the day 3 the cells were immortalized by adding virus solution that consisted of 50% primary culture media, 50% viral stock (pBABE Zeocin-SV40 Large T) and polybren (8 mg/ml). On day 4 the media was changed to DMEM high-glucose media (supplemented with 10% fetal bovine serume (FBS) and pennacilin/streptomycin) and on day 5, Zeocin selection began and remained for one week.

To differentiate brown adipocytes, cell lines were split into differentiation media (high-glucose DMEM including 10% FBS, 1% antibiotics, 20nM insulin and 1nM T_3) at day 1. Differentiation was induced with induction media (high-glucose DMEM including 10% FBS, 1% antibiotics, insulin 20nM, 1nM T_3, 0.125mM indomethacin, 2 µg/mL dexamethasone and 0.5mM 3-isobutyl-1-methylxanthine (IBMX)) after they reached confluence at day 4. On day 6, cells were put back into differentiation media. The media was changed one more time at day 8. To generate *Rictor*-iKO cells, 4-hydroxytamoxifen was added into the differentiation media at day 8. At the end of day 12 the control and *Rictor*-iKO cells were treated in DMEM high-glucose without FBS for 12 h and stimulated with 150 nM of insulin for 1, 2, 5, 10, 15, or 30 minutes. Cells were harvested by washing with ice-cold PBS, and flash freezing of the plates in liquid nitrogen.

3.5.2 Mass spectrometry sample preparation. Snap-frozen cells were lysed using ice-cold urea buffer (8M urea, 50 mM Tris pH 8.2, 75 mM NaCl, 50 mM β-glycerophosphate, 1 mM sodium orthovanadate, 10 mM sodium pyrophosphate, 50 mM sodium fluoride, and 1x EDTA-free protease inhibitors (Pierce). Two wells of a six-well plate were pooled for each sample. Each well was lysed into 125 µL of urea lysis buffer, and subsequently vortexed and homogenized using a probe sonicator 2 x each while kept ice cold. Lysates were then centrifuged at 16,000 x g to remove solid debris and lipids, and proteins amounts were quantified with a BCA assay (Pierce). Protein cysteine residues were then reduced with dithiothreitol (DTT) for 45 minutes at 55ºC, alkylated with 15 mM iodoacetamide for 30 minutes at room temperature in the dark, and

quenched with an additional 5 mM DTT for 15 minutes at room temperature. Samples were then diluted one-fifth with 50 mM Tris pH 8.2, and digested with trypsin for 16 hours at 37ºC. Digestions were quenched with trifluoroacetic acid (TFA) to pH < 2, and centrifuged for 10 minutes at 16,000 x g to remove precipitated debris. Clarified peptide samples were de-salted on 50 ug Sep-Pak columns (Waters), and dried using vacuum centrifugation. A portion of these dried peptides were used for whole proteome analysis.

Phosphopeptides were enriched using iron(III) immobilized metal-ion affinity chromatography (IMAC) using a Kingfisher Flex (Thermo). 250 µg of peptides were used, alongside with 70 µL of 5% iron(III)-loaded IMAC beads (Cube Biotech). Peptide binding to beads was done for 30 minutes in 80% acetonitrile and 0.1% TFA. Beads were then washed with 3 x 80% acetonitrile and 0.1% TFA, eluted with 2.5% NH_4OH and 50% acetonitrile, immediately acidified with 70% acetonitrile and 10% formic acid. Eluates were then filtered with 2-layer StageTips (Rappsilber et al. 2003) to remove any residual beads, and dried using vacuum centrifugation.

3.5.3 Liquid chromatography-tandem mass spectrometry (LC-MS/MS) data acquisition. Whole proteome analysis was done using data-dependent acquisition (DDA) on a EASY-nLC II (Thermo Scientific) coupled to a QExactive mass spectrometer (Thermo Scientific). LC was performed with a 40 cm long, 100 µm inner diameter column packed in-house with Reprosil C18 3 µm beads (Dr. Maisch GmbH), with a column oven set to 50°C. Prior to LC-MS/MS analysis, peptide samples were dissolved in a solution with 4% formic acid and 3% acetonitrile. Samples were separated with a linear gradient of 9% to 32% acetonitrile in 0.15% formic acid over 66 minutes. MS acquisition was performed using data-dependent acquisition with a “Top-20” method and 40 s dynamic exclusion. Full-scan MS was acquired between 300-1500 m/z at 70,000 resolution, with a 3 x 10^6 automatic gain control (AGC) target and 100 ms maximum injection time. Precursor fragmentation was performed with a 2 m/z isolation window using

higher-energy collisional dissociation with a 26% normalized collision energy. MS/MS acquisition was performed at 17,500 resolution with a 50 ms maximum injection time. MS and MS/MS were acquired in the orbitrap and data was collected in centroid mode.

Global phosphoproteomics was performed using DDA on a nanoACQUITY (Waters) coupled to a Orbitrap Fusion mass spectrometer (Thermo). Column length and bead specifications were the same as for the whole proteome analysis. Prior to LC-MS/MS analysis, peptide samples were dissolved in a solution with 4% formic acid and 3% acetonitrile. Chromatographic separation was performed with a linear 5% - 23% acetonitrile in 0.15% formic acid over 90 minutes. Full-scan MS was acquired between 375-1575 m/z at 120,000 resolution, with a 7 x 10^5 AGC target and 50 ms maximum injection time. Precursors were selected with a 1.6 m/z isolation window, a 50 ms maximum injection time and a flexible AGC target to maximize parallelizable time. Precursors were fragmented using higher-energy collisional dissociation with a 29% normalized collision energy. MS/MS acquisition was performed at 15,000 resolution. The number of MS/MS was tuned to achieve a 3 s duty cycle. Fragmented precursors were dynamically excluded from subsequent selection for 30 s. MS and MS/MS were acquired in the orbitrap and data was collected in centroid mode.

Targeted phosphoproteomics was performed using parallel reaction monitoring (PRM) on a EASY-nLC II (Thermo Scientific) coupled to a QExactive mass spectrometer (Thermo Scientific). LC was performed with a 20 cm long, 100 µm inner diameter column packed in-house with Reprosil C18 1.9 µm beads (Dr. Maisch GmbH), with a column oven set to 50°C. Chromatographic separation was performed with a linear 6% - 25% acetonitrile in 0.15% formic acid over 41 minutes. Precursor fragmentation was performed using higher-energy collisional dissociation with a 27% normalized collision energy. Full-scan MS was acquired between 300-1500 m/z at 70,000 resolution, with a 3 x 10^6 AGC target and 240 ms maximum injection time.

20 targeted precursor fragmentations were performed per duty cycle. Isolation was performed with a 2 m/z isolation window, and MS/MS acquisition was performed at 17,500 resolution with a 50 ms maximum injection time and a 2 x 10^5 AGC target. All MS data was collected in centroid mode. For the initial "calibration assay," retention time prediction windows were +/- 4 minutes, and for the final "quantification assay," retention time prediction windows were +/- 1.5 minutes.

3.5.4 Mass spectrometry data processing. For DDA experiments, raw files were converted to mzXML format and searched using Comet (Eng et al. 2013) against the mouse SwissProt database including isoforms (downloaded May 10, 2015). Methionine oxidation and N-terminal protein acetylation were treated as variable modifications, and carbamidomethylation of cysteine residues was treated as a constant modification. In the case of phosphoproteome analysis, phosphorylated serine/threonine/tyrosine residues were also treated as a variable modifications. Trypsin digestion was defined with cut-sites at lysine/arginine except when followed by proline. Precursor mass tolerance was set to 50 ppm, and fragment mass tolerance was 0.02 Daltons. Search results were filtered using Percolator (Käll et al. 2007) to obtain a list of peptide-spectrum matches at a <1% false discovery rate. Phosphorylation site localization was performed using an in-house implementation of Ascore (Beausoleil et al. 2006) that admits any post-translational modification setting, where sites with an Ascore ≥ 13 ($p \leq 0.05$) were considered localized. Quantification was performed using ThunderQuant, an in-house developed software for peptide quantification that relies on MS1 peak area integration. Peptide quantifications were pooled into protein quantifications, where the mean peptide quantification for each protein was taken to represent the protein. Protein quantifications were normalized to the total signal from each run. Phosphorylated peptides were pooled into phosphorylation site quantifications using the mean quantification of peptides that represented each site.

For targeted PRM experiments, raw files were analyzed directly in Skyline (MacLean et al. 2010), where the data was manually analyzed using a custom transition list generated for small-molecule mode. Raw files were also searched using the same Comet/Percolator/ThunderQuant/Ascore pipeline that was used for the data-dependent acquisition data to identify peptides and phosphorylation site localizations from each PRM MS/MS spectrum. Manual annotation of PRM targets, informed by the search results, allowed for confident identification of peptides and assignment of their respective chromatographic peaks.

3.5.5 Data analysis and statistics. Nearly all data analysis was performed using custom R scripts. Batch effects due to sample preparation batches and chromatographic instability were removed using the removeBatchEffect() function from the R package “limma”. All subsequent data analysis was performed on the batch effect-corrected samples. For the time course analysis, statistical significance of phosphorylation sites or proteins that respond to insulin, Rictor-iKO, or an interaction between the two was determined by (ANOVA) corrected by the Benjamini-Hochberg method. To determine phosphorylation sites that significantly increase or decrease in response to insulin in control or Rictor-iKO cells specifically, we used and a cubic spline model fitting that has been described previously (Storey et al. 2005). Analysis of protein-normalized phosphorylation was conducted by normalizing phosphorylation site quantifications to their respective protein in each replicate, and calculating statistics based on these new quantitative values. Hierarchical clustering heatmaps of phosphorylation sites were performed, using the R package “gplots”, on any site that significantly responds to insulin, as defined by its cubic spline fit, in either the control or Rictor-iKO cells. To focus the clustering analysis on the insulin response, each condition was normalized to the minimum condition in each time course. Principal component analysis was performed on the 500 phosphorylation sites with the highest

coefficient of variation across all samples. Gene ontology enrichment analysis on proteomics data was performed using the 1D enrichment tool in Perseus (Cox & Mann 2012).

Chapter 4: Discussion and Future Directions

4.1 How does the mechanism of activation affect the function of RICTOR/mTORC2?

One of the reasons mTORC2 has been difficult to study is that there is no definitive mechanism for its activation. mTORC2 activation has been most well studied in the context of insulin/PI3K/AKT signaling axis, and several studies have established upstream regulatory roles for PI3K, AKT, and IKKα (P. Liu et al. 2015; Yang et al. 2015; Dan et al. 2016). Our study in Chapter 3 focuses on mTORC2 signaling in the context of the insulin pathway; however, we also observed many phosphorylation sites to be significantly affected by RICTOR loss independent of insulin, suggesting that insulin-independent signaling pathways are also dependent on *Rictor*. Indeed, mTORC2 has other known upstream regulators besides insulin. Notably, mTORC2 has been shown to act downstream of β-adrenergic (βA) stimulation and cAMP synthesis (Olsen et al. 2014; Albert et al. 2016).

βA-induced mTORC2 activity in particular is relevant to BAT, though the mechanism is controversial and likely context dependent. In one study, mTORC2 activation in response to βA stimulation was shown to be dependent on the PI3K-AKT signaling axis in mouse BAT and in cultured brown adipocytes (Albert et al. 2016). In another study in mouse brown adipocytes, βA/mTORC2 signaling was found to be independent of PI3K/AKT (Olsen et al. 2014). The reason for this discrepancy has not been elucidated, though one possible explanation is that each study used mice with different genetic backgrounds. Regardless of whether βA/mTORC2 signaling occurs through the PI3K/AKT axis, the difference between βA- and insulin-driven mTORC2 activity has not been investigated systematically. Exploring βA-induced activation of mTORC2 using phosphoproteomic and phenotypic studies may be necessary to fully elucidate the importance of mTORC2 in BAT.

Another experimental approach that could reveal more important roles of *Rictor*-iKO is a signaling dose response. As discussed above, mTORC2 acts in a positive feedback mechanism along with AKT (Yang et al. 2015), which likely amplifies the response to stimulation of the PI3K-AKT axis in the context of insulin signaling. However, signal amplification could also be dependent on the dosage of insulin; if the insulin dosage is above a certain threshold, the signal response could become saturated such that the effect of a positive feedback loop is diminished. According to Medscape, peak blood insulin levels peak after meals can reach a maximum of approximately 1.9 nM, which is is much lower than the concentration of insulin used in our study, and many others. Thus, an insulin dose response experiment that spans physiological insulin concentrations may reveal a greater difference in insulin sensitivity between control and *Rictor*-iKO cells, and give a higher-resolution view of AKT substrates that are particularly mTORC2-dependent.

4.2 How do differentially phosphorylated forms of AKT function?

The most well appreciated role for mTORC2 is regulating AGC kinases, including AKT, by hydrophobic motif phosphorylation. Despite this, the functional effect of hydrophobic motif phosphorylation is quite poorly understood. Early mutation studies on AKT demonstrated that both activation loop phosphorylation (T308 on AKT1) and hydrophobic motif phosphorylation are necessary for AKT activation in transfected HEK 293 cells as measured by an AKT activity assay using immunoprecipitated AKT and a peptide substrate (Alessi et al. 1996). However, despite a strong decrease in AKT hydrophobic motif phosphorylation, cells lacking RICTOR display relatively normal phosphorylation of AKT substrates. This raises the question of what the functional differences are between different phosphorylated states of AKT.

To unravel differences between AKT phosphorylation states, Najafov et al. found through mutagenesis experiments that hydrophobic motif phosphorylation likely facilitates an orthogonal mode of AKT activation loop phosphorylation by PDK1, via binding the PIF pocket region in PDK1(Najafov et al. 2012). More recently, AKT hydrophobic motif phosphorylation in adipocytes was found not to be required for insulin-dependent translocation of the glucose transporter GLUT4 to the plasma membrane, while it was required for insulin-dependent GLUT1 translocation (Beg et al. 2017). Our proteome and phosphoproteome analysis from Chapter 3 expands on this finding to explore global downstream changes that are dependent on the presence of the mTORC2-specific subunit *Rictor*. Indeed, our phosphoproteomics work identified annotated AKT substrates whose phosphorylation in response to insulin activation is dependent on *Rictor*. While our *Rictor*-iKO cells have far less hydrophobic motif phosphorylation on AKT, the experiment did not allow us to systematically investigate the effect of different phosphorylated forms of AKT. To do this, it should be fruitful to express the previously characterized phospho-inhibitory and phospho-mimetic AKT mutants, and study their effects on the proteome and phosphoproteome. Because of redundancy in AKT isoforms, one strategy for this would be to generate brown adipocyte cell lines with all three endogenous AKT isoforms knocked out, and to express a single AKT isoform (e.g. AKT1) possessing one of different combinations of phospho-inhibitory or -mimetic mutants. Another possibility could be to exploit amber codons to encode phospho-threonine and phospho-serine residues directly in AKT. A targeted analysis of known AKT substrate phosphorylation in response to insulin for these different mutants would be an invaluable resource and provide much-needed context to our understanding of mTORC2-dependent insulin signaling.

APPENDIX: SUPPLEMENTAL MATERIAL FOR CHAPTER 2

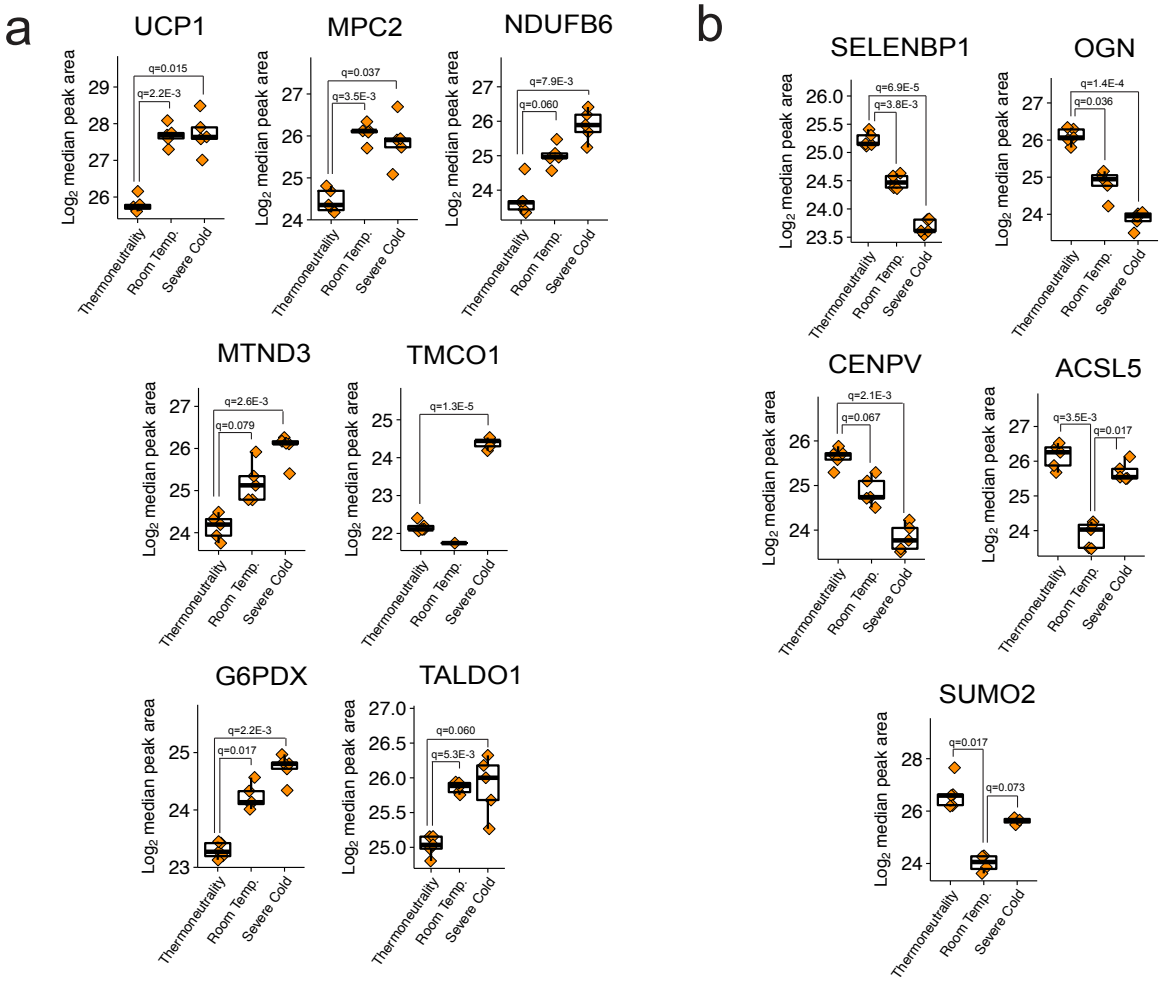

Figure S2.1: Proteome changes in room temperature versus thermoneutrality acclimation (related to Fig 2.1). (**A**) Plots of increasing proteins after mild and/or severe cold acclimation shown in the volcano plot. Data points represent measurements from individual animals. **(B)** Plots of decreasing proteins after mild and/or severe cold acclimation shown in the volcano plots in Figs 2.1d-e. Data points represent measurements from individual animals.

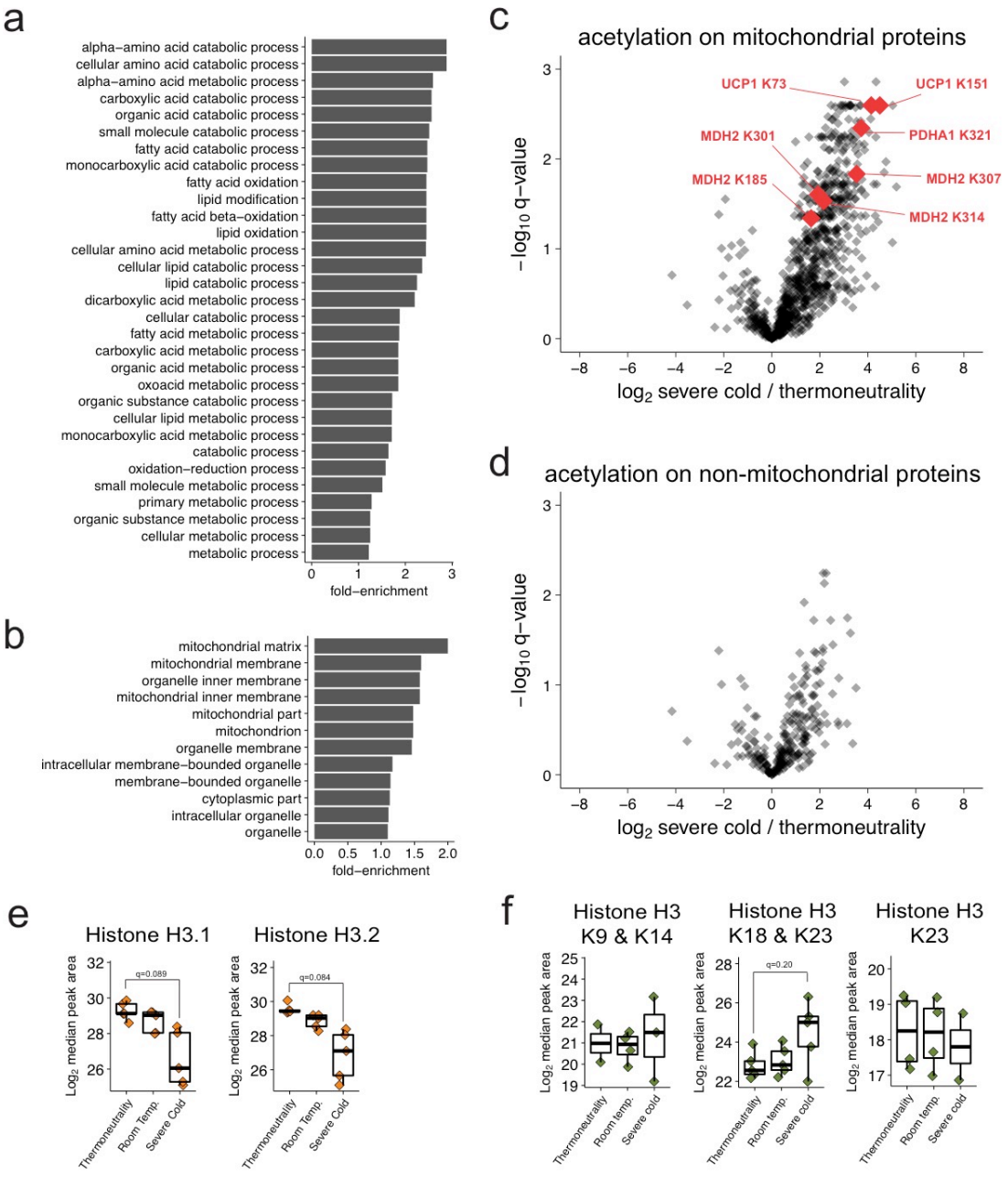

Figure S2.2: Acetylproteome changes in response to severe cold acclimation (related to Fig 2.4). **(A)** Complete list of enriched GO Process terms for the increasing acetylsites in severe cold vs. thermoneutrality (3-temp experiment). All enrichments are significant at 5% FDR. **(B)** Complete list of enriched GO Component terms for the increasing acetylsites in severe cold vs. thermoneutrality (3-temp experiment). All enrichments are significant at 5% FDR. **(C)** Volcano plot showing protein-normalized acetylation changes on mitochondrial proteins. Acetylsites that are plotted in Fig 3d-f are highlighted in red. **(D)** Volcano plot showing protein-normalized acetylation changes on non-mitochondrial proteins. **(E)** Quantification of histone H3.1 and H3.2 isoforms. Data points represent measurements from individual animals. **(F)** Quantification of acetylation on histone H3 tails, normalized to H3.1 protein levels. Data points represent measurements from individual animals.

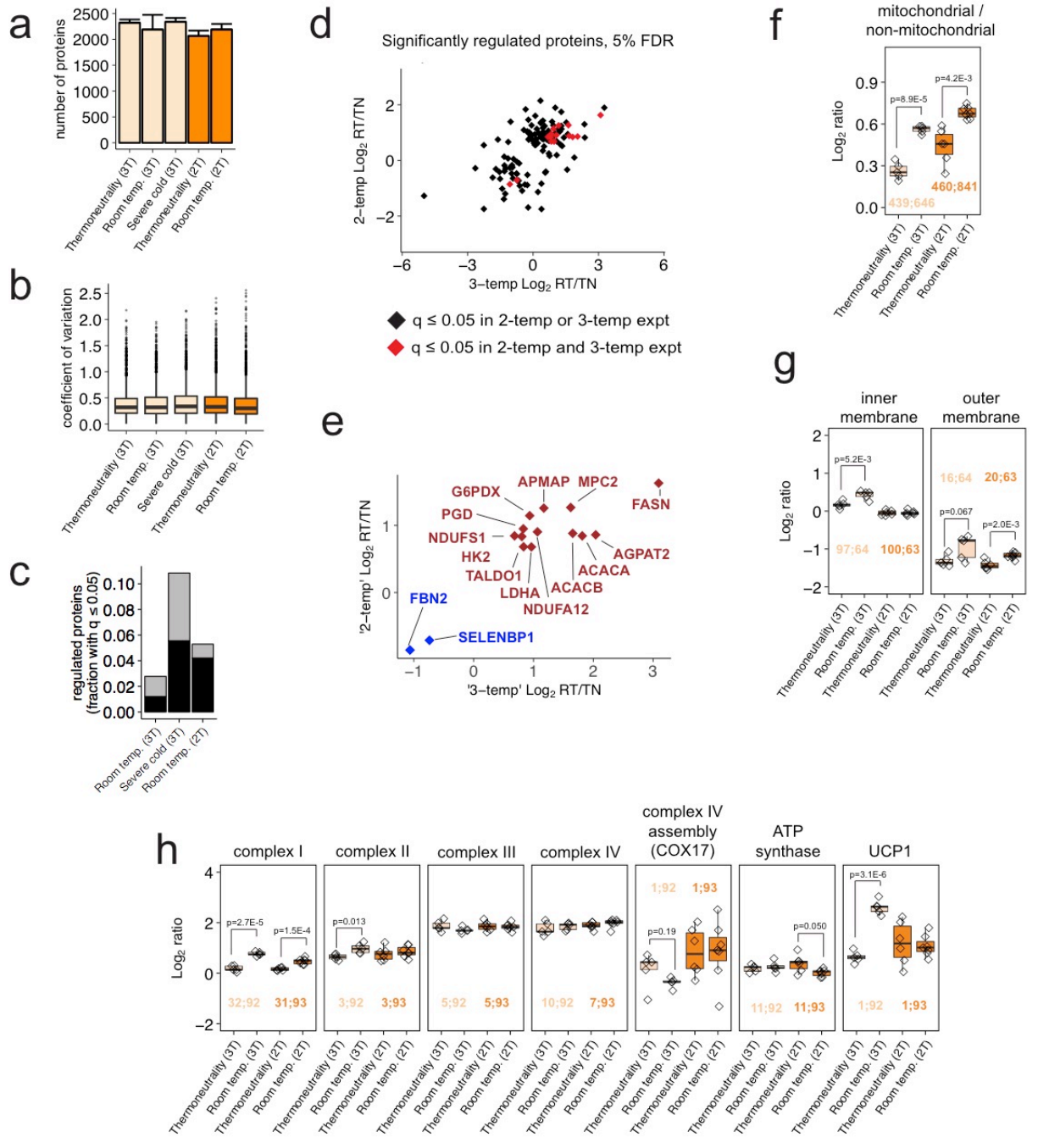

Figure S2.3: Additional two-temperature experiment validates proteomics findings. (A) Number of identified proteins in each biological condition, in both experiments. Lighter bars are from the three-temperature experiment, abbreviated "3T," and the darkers bars are from the two-temperature experiment, abbreviated "2T." Error bars represent standard deviation. **(B)** Distribution of the coefficients of variation in each biological condition, in both experiments. **(C)** The fraction of proteins with q ≤ 0.05, either increasing (black) or decreasing (grey), is plotted for the indicated experimental conditions and experiments, relative to the thermoneutrality control. **(D)** Scatter plot showing the Log_2 fold-changes between the severe cold and thermoneutrality in both the three-temperature experiment, and the two-

temperature experiment, in proteins that are significantly regulated in either of the two experiments. Points in red are significant in both experiments. **(E)** Data from panel D, except only showing those proteins that are significant in both experiments, along with their names. **(F)** For both the 3T and 2T experiments, in the room temperature and thermoneutrality conditions, plots showing changes to the Log_2 ratio of the median mitochondrial to the median non-mitochondrial protein. The number of proteins used to calculate medians for mitochondrial and non-mitochondrial fractions are indicated for each experiment before and after the semicolon, respectively. Data points represent ratios calculated from individual animals. **(G)** For both the 3T and 2T experiments, plot showing the Log_2 ratio of the median inner membrane or outer membrane protein to the median mitochondrial matrix protein. The number of inner/outer membrane proteins and the number of matrix proteins are indicated for each experiment before and after the semicolon, respectively. Data points represent ratios calculated from individual animals. **(H)** For both the 3T and 2T experiments, plot showing the Log_2 ratio of the median ETC complex protein to the median mitochondrial matrix protein. The number of ETC complex proteins and the number of matrix proteins are indicated for each experiment before and after the semicolon, respectively. Data points represent ratios calculated from individual animals.

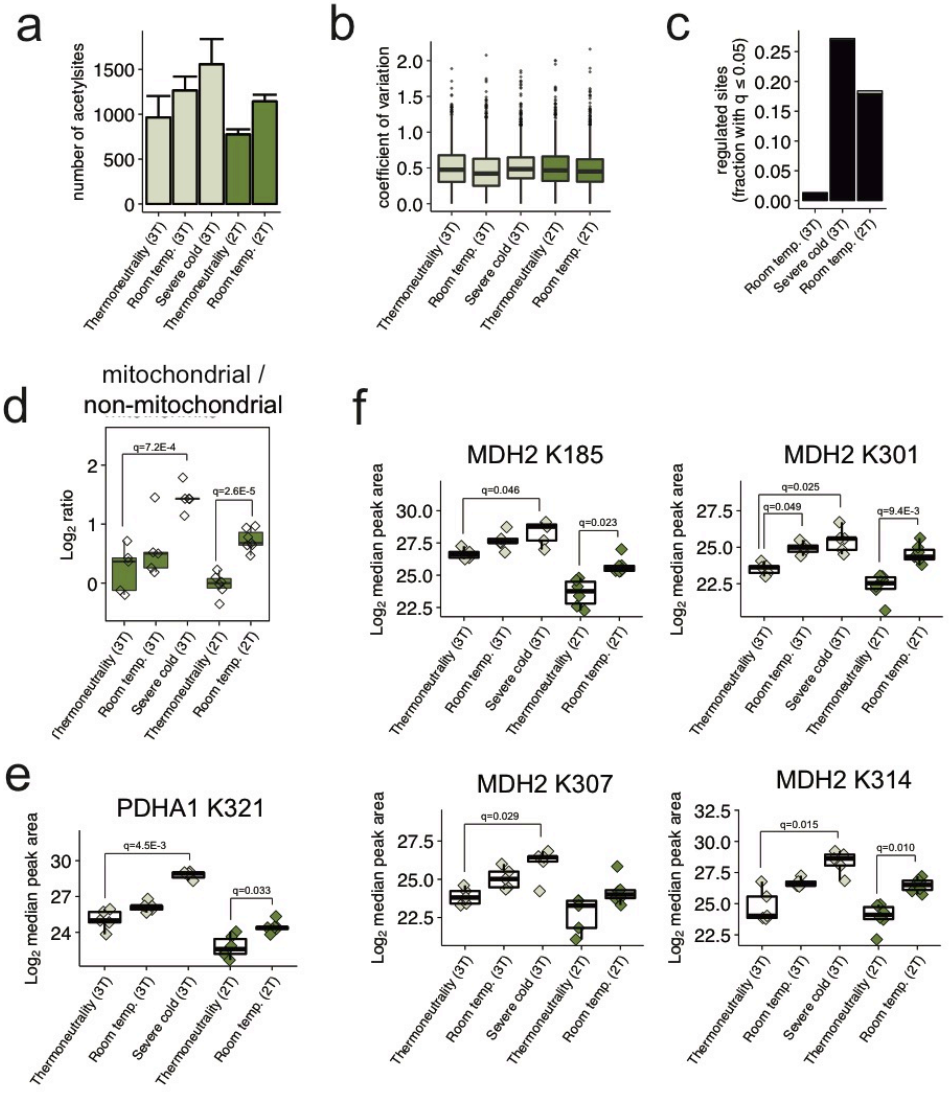

Figure S2.4: Protein acetylation changes after mild cold acclimation in two independent proteomics experiments. (A) Number of identified acetylsites in each biological condition, in both experiments. Lighter bars are from the three-temperature experiment, abbreviated “3T,” and the darkers bars are from the two-temperature experiment, abbreviated “2T.” Error bars represent standard deviation. **(B)** Distribution of the coefficients of variation in each biological condition, in both experiments. **(C)** The fraction of acetylsites with q ≤ 0.05, either increasing (black) or decreasing (grey), is plotted for the indicated experimental conditions and experiments, relative to the thermoneutrality control. **(D)** For both the 3T and 2T experiments, in the room temperature and thermoneutrality conditions, plots showing changes to the Log_2 ratio of the median mitochondrial to the median non-mitochondrial protein-normalized acetylsite. The number of acetylsites used to calculate medians for mitochondrial and non-mitochondrial fractions are indicated for each experiment before and after the semicolon, respectively. Data points represent ratios calculated from individual animals. **(E)** Quantification of PDHA1 K321 acetylation sites in both the 2T and 3T experiments. Data points represent measurements from individual animals. **(F)** Quantification of four MDH2 acetylation sites in both the 2T and 3T experiments. Data points represent measurements from individual animals.

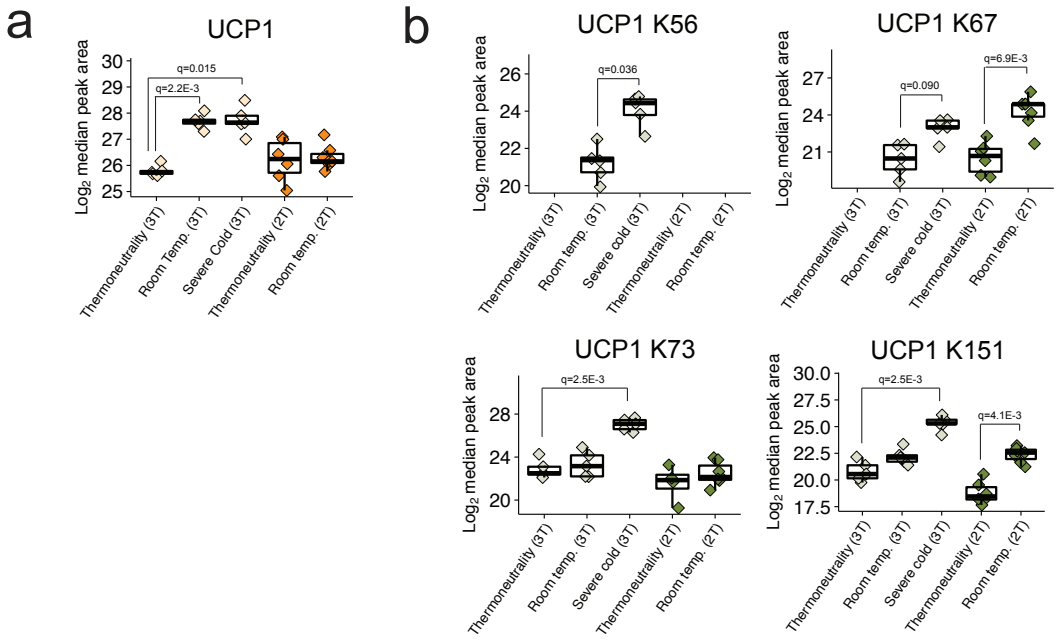

Figure S2.5: Regulation of UCP1 protein and acetylation levels during BAT thermogenesis. (A) Quantification of UCP1 protein levels in both the 2T and 3T experiments. Data points represent measurements from individual animals. **(B)** Quantification of UCP1 acetylation sites in both the 2T and 3T experiments. Data points represent measurements from individual animals.

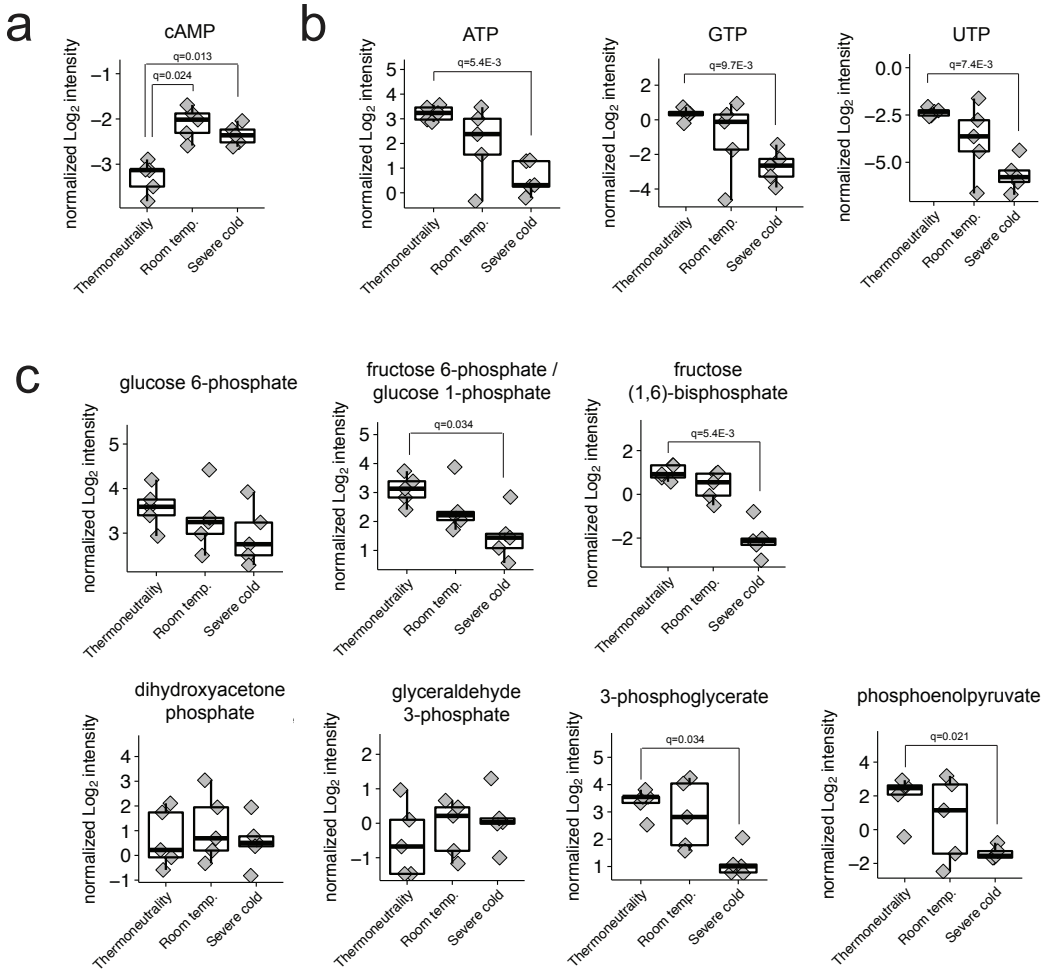

Figure S2.6: Additional polar metabolite measurements (related to Figure 2.5). (A) Abundance of cAMP after room temperature and severe cold acclimation. Data points represent measurements from individual animals. **(B)** Abundance of ATP, GTP, and UTP after room temperature and severe cold acclimation. Data points represent measurements from individual animals. **c**, Abundance of glycolysis intermediates after room temperature and severe cold acclimation. Data points represent measurements from individual animals.

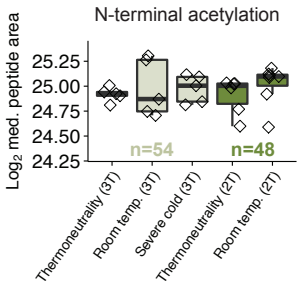

Figure S2.7: N-terminal acetylation does not change in BAT during cold acclimation. The median N-terminal acetylation peptide for each replicate is plotted above. The number of peptides seen in all replicates in each experiment is indicated. Data points represent median measurements from individual animals.

REFERENCES

Albert, V. et al., 2016. mTORC2 sustains thermogenesis via Akt-induced glucose uptake and glycolysis in brown adipose tissue. *EMBO molecular medicine*, 8(3), pp.232–246.

Alessi, D.R. et al., 1996. Mechanism of activation of protein kinase B by insulin and IGF-1. *The EMBO Journal*, 15(23), pp.6541–6551.

Bartelt, A. et al., 2011. Brown adipose tissue activity controls triglyceride clearance. *Nature Medicine*, 17(2), pp.200–205.

Bartelt, A. et al., 2018. Brown adipose tissue thermogenic adaptation requires Nrf1-mediated proteasomal activity. *Nature Medicine*, 24(3), pp.292–303.

Beausoleil, S.A. et al., 2006. A probability-based approach for high-throughput protein phosphorylation analysis and site localization. *Nature Biotechnology*, 24(10), pp.1285–1292.

Beg, M. et al., 2017. Distinct Akt phosphorylation states are required for insulin regulated Glut4 and Glut1-mediated glucose uptake. *eLife*, 6, p.729.

Berwick, D.C. et al., 2002. The identification of ATP-citrate lyase as a protein kinase B (Akt) substrate in primary adipocytes. *The Journal of biological chemistry*, 277(37), pp.33895–33900.

Betz, C. et al., 2013. Feature Article: mTOR complex 2-Akt signaling at mitochondria-associated endoplasmic reticulum membranes (MAM) regulates mitochondrial physiology. *Proceedings of the National Academy of Sciences of the United States of America*, 110(31), pp.12526–12534.

Boon, M.R. et al., 2014. Peripheral cannabinoid 1 receptor blockade activates brown adipose tissue and diminishes dyslipidemia and obesity. *FASEB journal : official publication of the Federation of American Societies for Experimental Biology*, 28(12), pp.5361–5375.

Cannon, B. & Nedergaard, J., 2011. Nonshivering thermogenesis and its adequate measurement in metabolic studies. *The Journal of experimental biology*, 214(Pt 2), pp.242–253.

Cereijo, R. et al., 2018. CXCL14, a Brown Adipokine that Mediates Brown-Fat-to-Macrophage Communication in Thermogenic Adaptation. *Cell Metabolism*.

Chaves, V.E. et al., 2012. Increased glyceride-glycerol synthesis in liver and brown adipose tissue of rat: in-vivo contribution of glycolysis and glyceroneogenesis. *Lipids*, 47(8), pp.773–780.

Chondronikola, M. et al., 2014. Brown Adipose Tissue Improves Whole-Body Glucose Homeostasis and Insulin Sensitivity in Humans. *Diabetes*, 63(12), pp.4089–4099.

Chouchani, E.T. et al., 2016. Mitochondrial ROS regulate thermogenic energy expenditure and

sulfenylation of UCP1. *Nature*, 532(7597), pp.112–116.

Chouchani, E.T., Kazak, L. & Spiegelman, B.M., 2017. Mitochondrial reactive oxygen species and adipose tissue thermogenesis: Bridging physiology and mechanisms. *The Journal of biological chemistry*, 292(41), pp.16810–16816.

Chow, J.D.Y. et al., 2014. Genetic inhibition of hepatic acetyl-CoA carboxylase activity increases liver fat and alters global protein acetylation. *Molecular Metabolism*, 3(4), pp.419–431.

Christoffolete, M.A. et al., 2004. Mice with Targeted Disruption of the Dio2 Gene Have Cold-Induced Overexpression of the Uncoupling Protein 1 Gene but Fail to Increase Brown Adipose Tissue Lipogenesis and Adaptive Thermogenesis. *Diabetes*, 53(3), pp.577–584.

Cox, J. & Mann, M., 2012. 1D and 2D annotation enrichment: a statistical method integrating quantitative proteomics with complementary high-throughput data. *BMC bioinformatics*, 13 Suppl 16(S16), p.S12.

Cypess, A.M. et al., 2009. Identification and Importance of Brown Adipose Tissue in Adult Humans. *New England Journal of Medicine*, 360(15), pp.1509–1517.

Dallner, O.S. et al., 2006. Beta3-adrenergic receptors stimulate glucose uptake in brown adipocytes by two mechanisms independently of glucose transporter 4 translocation. *Endocrinology*, 147(12), pp.5730–5739.

Dan, H.C., Antonia, R.J. & Baldwin, A.S., 2016. PI3K/Akt promotes feedforward mTORC2 activation through IKKα. *Oncotarget*, 7(16), pp.21064–21075.

Davies, M.N. et al., 2016. The Acetyl Group Buffering Action of Carnitine Acetyltransferase Offsets Macronutrient-Induced Lysine Acetylation of Mitochondrial Proteins. *Cell Reports*, 14(2), pp.243–254.

de Jesus, L.A. et al., 2001. The type 2 iodothyronine deiodinase is essential for adaptive thermogenesis in brown adipose tissue. *The Journal of Clinical Investigation*, 108(9), pp.1379–1385.

Ebner, M. et al., 2017. Localization of mTORC2 activity inside cells. *The Journal of Cell Biology*, 216(2), pp.343–353.

Ellis, J.M. et al., 2010. Adipose acyl-CoA synthetase-1 directs fatty acids toward beta-oxidation and is required for cold thermogenesis. *Cell Metabolism*, 12(1), pp.53–64.

Eng, J.K., Jahan, T.A. & Hoopmann, M.R., 2013. Comet: An open-source MS/MS sequence database search tool. *PROTEOMICS*, 13(1), pp.22–24.

Fan, J. et al., 2014. Tyr phosphorylation of PDP1 toggles recruitment between ACAT1 and SIRT3 to regulate the pyruvate dehydrogenase complex. *Molecular Cell*, 53(4), pp.534–548.

Fedorenko, A., Lishko, P.V. & Kirichok, Y., 2012. Mechanism of Fatty-Acid-Dependent UCP1 Uncoupling in Brown Fat Mitochondria. *Cell*, 151(2), pp.400–413.

Feldmann, H.M. et al., 2009. UCP1 ablation induces obesity and abolishes diet-induced thermogenesis in mice exempt from thermal stress by living at thermoneutrality. *Cell Metabolism*, 9(2), pp.203–209.

Fisher-Wellman, K.H. et al., 2019. Respiratory Phenomics across Multiple Models of Protein Hyperacylation in Cardiac Mitochondria Reveals a Marginal Impact on Bioenergetics. *Cell Reports*, 26(6), pp.1557–1572.e8.

Gao, D. et al., 2010. Rictor forms a complex with Cullin-1 to promote SGK1 ubiquitination and destruction. *Molecular Cell*, 39(5), pp.797–808.

Gingras, A.C. et al., 2001. Hierarchical phosphorylation of the translation inhibitor 4E-BP1. *Genes \& Development*, 15(21), pp.2852–2864.

Gnad, T. et al., 2014. Adenosine activates brown adipose tissue and recruits beige adipocytes via A2A receptors. *Nature*, 516(7531), pp.395–399.

Gordon, C.J., Becker, P. & Ali, J.S., 1998. Behavioral thermoregulatory responses of single- and group-housed mice. *Physiology & behavior*, 65(2), pp.255–262.

Grzelkowska-Kowalczyk, K. & Wieteska-Skrzeczyńska, W., 2009. Treatment with IFN-gamma prevents insulin-dependent PKB, p70S6k phosphorylation and protein synthesis in mouse C2C12 myogenic cells. *Cell biology international*, 34(1), pp.117–124.

Guerra, C. et al., 2001. Brown adipose tissue-specific insulin receptor knockout shows diabetic phenotype without insulin resistance. *The Journal of Clinical Investigation*, 108(8), pp.1205–1213.

Guertin, D.A. et al., 2006. Ablation in Mice of the mTORC Components raptor, rictor, or mLST8 Reveals that mTORC2 Is Required for Signaling to Akt-FOXO and PKCα, but Not S6K1. *Developmental Cell*, 11(6), pp.859–871.

Guilherme, A. et al., 2018. Neuronal modulation of brown adipose activity through perturbation of white adipocyte lipogenesis. *Molecular Metabolism*, 16, pp.116–125.

Hagan, G.N. et al., 2008. A Rictor-Myo1c complex participates in dynamic cortical actin events in 3T3-L1 adipocytes. *Molecular and Cellular Biology*, 28(13), pp.4215–4226.

HALL, L.M., METZENBERG, R.L. & COHEN, P.P., 1958. Isolation and characterization of a naturally occurring cofactor of carbamyl phosphate biosynthesis. *The Journal of biological chemistry*, 230(2), pp.1013–1021.

Hansen, B.K. et al., 2019. Analysis of human acetylation stoichiometry defines mechanistic constraints on protein regulation. *Nature Communications*, 10(1), p.1055.

Hebert, A.S. et al., 2013. Calorie Restriction and SIRT3 Trigger Global Reprogramming of the Mitochondrial Protein Acetylome. *Molecular Cell*, 49(1), pp.186–199.

Horton, J.D., Goldstein, J.L. & Brown, M.S., 2002. SREBPs: activators of the complete program of cholesterol and fatty acid synthesis in the liver. *The Journal of Clinical Investigation*,

109(9), pp.1125–1131.

Hui, S. et al., 2017. Glucose feeds the TCA cycle via circulating lactate. *Nature*, 551(7678), p.nature24057.

Humphrey, S.J. et al., 2013. Dynamic Adipocyte Phosphoproteome Reveals that Akt Directly Regulates mTORC2. *Cell Metabolism*, 17(6), pp.1009–1020.

Hung, C.-M. et al., 2014. Rictor/mTORC2 Loss in the Myf5 Lineage Reprograms Brown Fat Metabolism and Protects Mice against Obesity and Metabolic Disease. *Cell Reports*, 8(1), pp.256–271.

Ikeda, K. et al., 2017. UCP1-independent signaling involving SERCA2b-mediated calcium cycling regulates beige fat thermogenesis and systemic glucose homeostasis. *Nature Medicine*, 23(12), pp.1454–1465.

Irshad, Z. et al., 2017. Diacylglycerol acyltransferase 2 links glucose utilization to fatty acid oxidation in the brown adipocytes. *Journal of lipid research*, 58(1), pp.15–30.

Jeong, J.H., Chang, J.S. & Jo, Y.-H., 2018. Intracellular glycolysis in brown adipose tissue is essential for optogenetically induced nonshivering thermogenesis in mice. *Scientific Reports*, 8(1), p.6672.

Kazak, L. et al., 2015. A creatine-driven substrate cycle enhances energy expenditure and thermogenesis in beige fat. *Cell*, 163(3), pp.643–655.

Kazak, L. et al., 2017. Genetic Depletion of Adipocyte Creatine Metabolism Inhibits Diet-Induced Thermogenesis and Drives Obesity. *Cell Metabolism*, 26(4), p.693.

Käll, L. et al., 2007. Semi-supervised learning for peptide identification from shotgun proteomics datasets. *Nature Methods*, 4(11), pp.923–925.

Kissig, M. et al., 2017. PRDM16 represses the type I interferon response in adipocytes to promote mitochondrial and thermogenic programing. *The EMBO Journal*, 36(11), pp.1528–1542.

Kleinert, M. et al., 2016. mTORC2 and AMPK differentially regulate muscle triglyceride content via Perilipin 3. *Molecular Metabolism*, 5(8), pp.646–655.

Kumar, A. et al., 2010. Fat Cell–Specific Ablation of Rictor in Mice Impairs Insulin-Regulated Fat Cell and Whole-Body Glucose and Lipid Metabolism. *Diabetes*, 59(6), pp.1397–1406.

Kumar, A. et al., 2008. Muscle-specific deletion of rictor impairs insulin-stimulated glucose transport and enhances Basal glycogen synthase activity. *Molecular and Cellular Biology*, 28(1), pp.61–70.

Lamming, D.W. et al., 2014. Hepatic signaling by the mechanistic target of rapamycin complex 2 (mTORC2). *The FASEB Journal*, 28(1), pp.300–315.

Lawrence, R.T. et al., 2016. Plug-and-play analysis of the human phosphoproteome by targeted

high-resolution mass spectrometry. *Nature Methods*, 13(5), pp.431–434.

Lee, J., Ellis, J.M. & Wolfgang, M.J., 2015. Adipose fatty acid oxidation is required for thermogenesis and potentiates oxidative stress-induced inflammation. *Cell Reports*, 10(2), pp.266–279.

Lee, K.Y. et al., 2013. Lessons on conditional gene targeting in mouse adipose tissue. *Diabetes*, 62(3), pp.864–874.

Letts, J.A. & Sazanov, L.A., 2017. Clarifying the supercomplex: the higher-order organization of the mitochondrial electron transport chain. *Nature Structural \& Molecular Biology*, 24(10), pp.800–808.

Li, L. et al., 2015. p38 MAP kinase-dependent phosphorylation of the Gp78 E3 ubiquitin ligase controls ER-mitochondria association and mitochondria motility. T. D. Fox, ed. *Molecular biology of the cell*, 26(21), pp.3828–3840.

Li, Y. et al., 2013. Mass spectrometry-based detection of protein acetylation. *Methods in molecular biology (Clifton, N.J.)*, 1077(Chapter 6), pp.81–104.

Lindberg, O. et al., 1967. Studies of the mitochondrial energy-transfer system of brown adipose tissue. *The Journal of Cell Biology*, 34(1), pp.293–310.

Liu, P. et al., 2015. PtdIns(3,4,5)P3-Dependent Activation of the mTORC2 Kinase Complex. *Cancer discovery*, 5(11), pp.1194–1209.

Lopez-Fabuel, I. et al., 2016. Complex I assembly into supercomplexes determines differential mitochondrial ROS production in neurons and astrocytes. *Proceedings of the National Academy of Sciences of the United States of America*, 113(46), pp.13063–13068.

MacLean, B. et al., 2010. Skyline: an open source document editor for creating and analyzing targeted proteomics experiments. *Bioinformatics*, 26(7), pp.966–968.

Marcinkiewicz, A. et al., 2006. The phosphorylation of serine 492 of perilipin a directs lipid droplet fragmentation and dispersion. *The Journal of biological chemistry*, 281(17), pp.11901–11909.

Masui, K. et al., 2013. mTOR Complex 2 Controls Glycolytic Metabolism in Glioblastoma through FoxO Acetylation and Upregulation of c-Myc. *Cell Metabolism*, 18(5), pp.726–739.

McGillicuddy, F.C. et al., 2009. Interferon gamma attenuates insulin signaling, lipid storage, and differentiation in human adipocytes via activation of the JAK/STAT pathway. *The Journal of biological chemistry*, 284(46), pp.31936–31944.

Mills, E.L. et al., 2018. Accumulation of succinate controls activation of adipose tissue thermogenesis. *Nature*, 560(7716), pp.102–106.

Moisan, A. et al., 2015. White-to-brown metabolic conversion of human adipocytes by JAK inhibition. *Nature Cell Biology*, 17(1), pp.57–67.

Mottillo, E.P. et al., 2014. Coupling of lipolysis and de novo lipogenesis in brown, beige, and white adipose tissues during chronic β3-adrenergic receptor activation. *Journal of lipid research*, 55(11), pp.2276–2286.

Mukaida, S. et al., 2017. Adrenoceptors promote glucose uptake into adipocytes and muscle by an insulin-independent signaling pathway involving mechanistic target of rapamycin complex 2. *Pharmacological research*, 116, pp.87–92.

Najafov, A., Shpiro, N. & Alessi, D.R., 2012. Akt is efficiently activated by PIF-pocket- and PtdIns(3,4,5)P3-dependent mechanisms leading to resistance to PDK1 inhibitors. *The Biochemical journal*, 448(2), pp.285–295.

Narita, T., Weinert, B.T. & Choudhary, C., 2019. Functions and mechanisms of non-histone protein acetylation. *Nature Reviews Molecular Cell Biology*, 20(3), pp.156–174.

Oh, M.-H. et al., 2017. mTORC2 Signaling Selectively Regulates the Generation and Function of Tissue-Resident Peritoneal Macrophages. *Cell Reports*, 20(10), pp.2439–2454.

Olsen, J.M. et al., 2014. Glucose uptake in brown fat cells is dependent on mTOR complex 2-promoted GLUT1 translocation. *The Journal of Cell Biology*, 207(3), pp.365–374.

Ouellet, V. et al., 2011. Outdoor Temperature, Age, Sex, Body Mass Index, and Diabetic Status Determine the Prevalence, Mass, and Glucose-Uptake Activity of 18F-FDG-Detected BAT in Humans. *The Journal of Clinical Endocrinology \& Metabolism*, 96(1), pp.192–199.

Ozden, O. et al., 2014. SIRT3 deacetylates and increases pyruvate dehydrogenase activity in cancer cells. *Free radical biology & medicine*, 76, pp.163–172.

Pearson, D.J. & Tubbs, P.K., 1967. Carnitine and derivatives in rat tissues. *The Biochemical journal*, 105(3), pp.953–963.

Pilch, P.F. & Liu, L., 2011. Fat caves: caveolae, lipid trafficking and lipid metabolism in adipocytes. *Trends in endocrinology and metabolism: TEM*, 22(8), pp.318–324.

Potapova, I.A. et al., 2000. Phosphorylation of recombinant human ATP:citrate lyase by cAMP-dependent protein kinase abolishes homotropic allosteric regulation of the enzyme by citrate and increases the enzyme activity. Allosteric activation of ATP:citrate lyase by phosphorylated sugars. *Biochemistry*, 39(5), pp.1169–1179.

Rappsilber, J., Ishihama, Y. & Mann, M., 2003. Stop and Go Extraction Tips for Matrix-Assisted Laser Desorption/Ionization, Nanoelectrospray, and LC/MS Sample Pretreatment in Proteomics. *Analytical Chemistry*, 75(3), pp.663–670.

Ray, N.B. & Mathews, C.K., 1992. Nucleoside diphosphokinase: a functional link between intermediary metabolism and nucleic acid synthesis. *Current topics in cellular regulation*, 33, pp.343–357.

Risso, G. et al., 2015. Akt/PKB: one kinase, many modifications. *The Biochemical journal*, 468(2), pp.203–214.

Rothwell, N.J. & Stock, M.J., 1997. A role for brown adipose tissue in diet-induced thermogenesis. *Obesity research*, 5(6), pp.650–656.

Sanchez-Gurmaches, J. et al., 2018. Brown Fat AKT2 Is a Cold-Induced Kinase that Stimulates ChREBP-Mediated De Novo Lipogenesis to Optimize Fuel Storage and Thermogenesis. *Cell Metabolism*, 27(1), pp.195–209.e6.

Sanchez-Gurmaches, J., Hung, C.-M. & Guertin, D.A., 2016. Emerging Complexities in Adipocyte Origins and Identity. *Trends in cell biology*, 26(5), pp.313–326.

Sarbassov, D.D., 2005. Phosphorylation and Regulation of Akt/PKB by the Rictor-mTOR Complex. *Science*, 307(5712), pp.1098–1101.

Saxton, R.A. & Sabatini, D.M., 2017. mTOR Signaling in Growth, Metabolism, and Disease. *Cell*, 168(6), pp.960–976.

Schulz, T.J. et al., 2013. Brown-fat paucity due to impaired BMP signalling induces compensatory browning of white fat. *Nature*, 495(7441), pp.379–383.

Schwer, B. et al., 2009. Calorie restriction alters mitochondrial protein acetylation. *Aging Cell*, 8(5), pp.604–606.

Shahbazian, D. et al., 2006. The mTOR/PI3K and MAPK pathways converge on eIF4B to control its phosphorylation and activity. *The EMBO Journal*, 25(12), pp.2781–2791.

Shaw, A.E. et al., 2017. Fundamental properties of the mammalian innate immune system revealed by multispecies comparison of type I interferon responses. H. Malik, ed. *PLoS biology*, 15(12), p.e2004086.

Shimobayashi, M. et al., 2018. Insulin resistance causes inflammation in adipose tissue. *The Journal of Clinical Investigation*, 128(4), pp.1538–1550.

Stanford, K.I. et al., 2013. Brown adipose tissue regulates glucose homeostasis and insulin sensitivity. *The Journal of Clinical Investigation*, 123(1), pp.215–223.

Storey, J.D. et al., 2005. Significance analysis of time course microarray experiments. *Proceedings of the National Academy of Sciences of the United States of America*, 102(36), pp.12837–12842.

Strack, A.M., Bradbury, M.J. & Dallman, M.F., 1995. Corticosterone decreases nonshivering thermogenesis and increases lipid storage in brown adipose tissue. *The American journal of physiology*, 268(1 Pt 2), pp.R183–91.

Suzuki, M., Setsuie, R. & Wada, K., 2009. Ubiquitin carboxyl-terminal hydrolase l3 promotes insulin signaling and adipogenesis. *Endocrinology*, 150(12), pp.5230–5239.

Šestan, M. et al., 2018. Virus-Induced Interferon-γ Causes Insulin Resistance in Skeletal Muscle and Derails Glycemic Control in Obesity. *Immunity*, 49(1), pp.164–177.e6.

Townsend, K.L. & Tseng, Y.-H., 2014. Brown fat fuel utilization and thermogenesis. *Trends in*

Endocrinology \& Metabolism, 25(4), pp.168–177.

Townsend, M.K. et al., 2013. Reproducibility of metabolomic profiles among men and women in 2 large cohort studies. *Clinical chemistry*, 59(11), pp.1657–1667.

Vallerand, A.L., Pérusse, F. & Bukowiecki, L.J., 1987. Cold exposure potentiates the effect of insulin on in vivo glucose uptake. *The American journal of physiology*, 253(2 Pt 1), pp.E179–86.

van den Beukel, J.C. et al., 2014. Direct activating effects of adrenocorticotropic hormone (ACTH) on brown adipose tissue are attenuated by corticosterone. *FASEB journal : official publication of the Federation of American Societies for Experimental Biology*, 28(11), pp.4857–4867.

Villarroya, F. et al., 2018. Brown Adipokines. *Handbook of experimental pharmacology*, 102(Chapter 119), pp.3324–18.

Villarroya, F., Cereijo, R., et al., 2017. Brown adipose tissue as a secretory organ. *Nature reviews. Endocrinology*, 13(1), pp.26–35.

Villarroya, F., Gavaldà-Navarro, A., et al., 2017. The Lives and Times of Brown Adipokines. *Trends in endocrinology and metabolism: TEM*, 28(12), pp.855–867.

Wagner, G.R. & Payne, R.M., 2013. Widespread and enzyme-independent Nε-acetylation and Nε-succinylation of proteins in the chemical conditions of the mitochondrial matrix. *The Journal of biological chemistry*, 288(40), pp.29036–29045.

Wang, H. et al., 2018. Quantitative Proteomics Implicates Rictor/mTORC2 in Cell Adhesion. *Journal of Proteome Research*, 17(10), pp.3360–3369.

Winther, S. et al., 2018. Restricting glycolysis impairs brown adipocyte glucose and oxygen consumption. *American Journal of Physiology-Endocrinology and Metabolism*, 314(3), pp.E214–E223.

Wu, Q. et al., 2006. Fatty acid transport protein 1 is required for nonshivering thermogenesis in brown adipose tissue. *Diabetes*, 55(12), pp.3229–3237.

Yang, G. et al., 2015. A Positive Feedback Loop between Akt and mTORC2 via SIN1 Phosphorylation. *Cell Reports*, 12(6), pp.937–943.

Yu, X.X. et al., 2002. Cold elicits the simultaneous induction of fatty acid synthesis and beta-oxidation in murine brown adipose tissue: prediction from differential gene expression and confirmation in vivo. *FASEB journal : official publication of the Federation of American Societies for Experimental Biology*, 16(2), pp.155–168.

Yuan, M. et al., 2012. Identification of Akt-independent regulation of hepatic lipogenesis by mammalian target of rapamycin (mTOR) complex 2. *The Journal of biological chemistry*, 287(35), pp.29579–29588.

Zhang, Y. et al., 2014. Coordinated regulation of protein synthesis and degradation by

mTORC1. *Nature*, 513(7518), pp.440–443.

Zhao, S. et al., 2010. Regulation of cellular metabolism by protein lysine acetylation. *Science*, 327(5968), pp.1000–1004.

Zinzalla, V. et al., 2011. Activation of mTORC2 by Association with the Ribosome. *Cell*, 144(5), pp.757–768.